Title
Cellular Mechanotransduction via Microfabricated Post Arrays

Author
Higa, Adrienne

Publication Date
2012

Peer reviewed|Thesis/dissertation

Cellular Mechanotransduction via Microfabricated Post Arrays

By

Adrienne Therese Higa

A dissertation submitted in partial satisfaction of the

requirements for the degree of

Doctor of Philosophy

in

Engineering – Mechanical Engineering

in the

Graduate Division

of the

University of California, Berkeley

Committee in charge:

Professor Liwei Lin, Chair
Professor Song Li
Professor Dorian Liepmann

Spring 2012

Abstract

Cellular Mechanotransduction via Microfabricated Post Arrays

by

Adrienne Therese Higa

Doctor of Philosophy in Mechanical Engineering

University of California, Berkeley

Professor Liwei Lin, Chair

Substrate-based biophysical cues, which interact with cells through mechanotransductive pathways, influence many biological processes and cellular behaviors. By leveraging microfabrication techniques, this work aims to build biophysical stimuli into cellular substrates through discrete microtopographic features to study cellular responses. Here, uniform and gradient arrays of circular microposts have been geometrically tuned to change the apparent rigidity of a substrate and the placement of available cellular attachment sites. Three areas of cellular interaction with these micropost array substrates have been investigated: (*i*) single cell motility, (*ii*) maintenance and inhibition of collective cell behavior, and (*iii*) reprogramming and differentiation processes of induced pluripotent stem cells (iPSCs).

Single cell migration was induced through gradients in substrate stiffness and spacing of available attachment sites – phenomena known as durotaxis and herein referred to as spatiotaxis, respectively. Unidirectional micropost arrays gradients were designed with increasing stiffnesses at low and high gradient strengths of 0.5 nN/μm and 7.5 nN/μm, respectively. On these surfaces, bovine aortic endothelial cells (BAECs) were found to preferentially migrate toward the direction of increasing micropost stiffness. In 18-hour studies, with more than 12 single cells in each case, BAECs had average displacements of 26.5 ± 8.7 μm and 41.9 ± 14.7 μm for the low and high gradient strengths, respectively. Furthermore, BAECs were found to migrate in favor of the direction of decreasing interpost spacing over the direction of increasing stiffness in the prototype micropost arrays, demonstrating that spatial cues can dominate stiffness cues in the migratory response of cells.

The maintenance and inhibition of collective cell behavior was studied through changes in substrate stiffness and spacing via uniform and gradient micropost arrays with stiffnesses in the range

of 24-106 nN/μm. BAEC collectives directly cultured on these surfaces exhibited area contraction or expansion, which corresponded to maintenance and inhibition of group behavior on soft and stiff substrates, respectively. The micropost mechanical stiffness required for collective-to-single cell transitions was characterized as 30 ± 6 nN/μm. Effects of spacing on collective cell behavior were also explored, and results showed that BAEC collectives were unable to maintain group behavior with favorable stiffness cues, demonstrating again the significance of micropost spacing.

The effects of microtopography on the reprogramming and differentiation of iPSCs was investigated through uniform micropost arrays of varying radii and heights with mouse ear fibroblasts (mERFs) on micropost arrays with stiffnesses in the range of 24-2900 nN/μm. Preliminary results have shown that microtopography had influence over the formation of iPSC colonies and the number of colonies that exhibited beating. Specifically, beating colonies were observed as early as 10 days after the infection of mERFs on micropost surfaces, suggesting that microtopography might direct the differentiation of iPSCs. Characterizations of changes in mERF morphology, expression of nuclear structural proteins, and intracellular localization of proteins that regulate gene expression provide evidence for possible mechanisms responsible for the effects of microtopography on the reprogramming and differentiation processes of iPSCs.

Dedication

This body of work is dedicated to my parents, brother, sister, and grandparents – the loves of my life.

Acknowledgements

My graduate career at UC Berkeley has been, by far, the greatest force of my own efforts in molding me into the person I am today. It has been an incredible experience, both humbling and empowering, and I certainly could not have navigated my way through without the grace and support of so many people in my life. I have been extraordinarily fortunate in that the people who have helped me through this journey have chosen to share their lives with me, beyond the call of academic duty. For this, I am most grateful.

I would first like to thank my family, best friends, and boyfriend for their unwavering support of me, independent of my professional accomplishments. Knowing that the standards and expectations of society were not important measures of my self-worth gave me the strength and capacity to put my greatest efforts towards learning and growing in all aspects of my life. This enabled my graduate career to be much more than an academic pursuit, and planted me onto a path to become the person I have always wanted to become.

Without the guidance of my advisor, Professor Liwei Lin, I would not have had the opportunity to succeed and fail in a safe environment. Professor Lin let me be creative and excited about science, let me take responsibility for my failures, helped me appreciated my accomplishments, pushed me to look out for myself, and taught me the importance of being an independent and critical thinker. I do not think there are many professors out there who care as much as he does about his students, and I am very grateful that he has been present throughout my entire academic training.

I have had great mentors in addition to my advisor, who have been cheerleaders for both my research and personal development. Professor Song Li, my ‘co-advisor’, has been very patient and generous with his time, interest in my work, and knowledge throughout my Ph.D, and it has been a great pleasure to collaborate with his lab. Professors Dorian Liepmann, Al Pisano, Lydia Sohn, and Lisa Pruitt have always made time to provide me valuable research support and life advice during my career.

Numerous staff members and specialists throughout the UC Berkeley campus have personally been supportive of my research and growth. I would like to thank Helen Kim, Donna Craig, Julia Chu, Mary West, Terry Johnson, Xiao Fan Meng, Kim Chan, Quanming Shi, Sia Parsa, Kim Ly, John Huggins, Richard Lossing, Alain Kesseru, Shareena Samson, Pat Giddings, Yawo Akpawu, Mick Franssen, Gordon Long, Tom Clark, and Rene Viray.

My journey through graduate school would not have been so colorful, fulfilling, or productive without my friends and their laboratories on campus:

Within my own lab, I have been very fortunate to have worked so closely with amazing, brilliant people. Dr. Ryan Sochol, one of my oldest research partners and video co-producer, has been a tour du force. Knowing him has been life-changing, and I have learned many valuable lessons

through our numerous shared research and friendship experiences and endless vibrant discussions. Many of my lab contemporaries and alumni have been extraordinary, and I would like to thank Dr. Brian Sosnowchik, Heather Chiamori, Dr. Erika Parra, Armon Mahajerin, Kedar Shah, Alina Kozinda, Kosuke Iwai, Rich Winslow, Kevin Limkrailassiri, Dr. Yingqi Jiang, and Jiyoung Chang for their friendship over the years.

My collaborative efforts with the Bioengineering Department introduced me to some of the most exceptional researchers and kindest friends I have ever known. Dr. Maral Gharib, Dr. Randall Janairo, Annie Chou, Tim Downing, Elaine Su, An-Chi Tsou, Dr. Gary Lee, Sam Tia, Jeff Henry, Professor Aijun Wang, and Ashley Fritz, have helped to inspire an enduring dedication to the field, excitement for science, and commitment to having fun.

When I needed to step outside of my lab for research help and guidance, many friends in Mechanical Engineering, Electrical Engineering and Computer Science, and AS&T were glad to lend their time and intellect. I am particularly indebted to Professor Debbie Senesky, Matt Chan, Dr. Gabriele Vigevani, Sarah Wodin-Schwartz, Dr. Jim Cheng, Ting-Ta Yen, Yegan Erdem, Chris McCoy, Lindsay Miller, Sara Beani, Kim Lau, Peter Matheu, Dr. Donovan Lee, Dr. Li-Wen Hung, Dr. Reinaldo Vega, Zach Jacobson, Byron Ho, Erick Ulin-Avila, and Dr. Ze'ev Abrams.

Of course, life extends far beyond academia and my network of friends and colleagues, both on and off campus, has never failed me. I am eternally grateful to everyone of my past and present who has helped me discover and explore all of the wonderful things life has to offer.

Table of Contents

List of Figures

List of Acronyms

BAEC	Bovine Aortic Endothelial Cell
BSA	Bovine Serum Albumin
CCD	Charge-Coupled Device
cTnT	Cardiac Troponin T
DAPI	4’,6-Diamidino-2-Phenylindole
DI	Deionized
DMEM	Dulbecco’s Modified Eagle Medium
DNA	Deoxyribonucleic Acid
ECM	Extracellular Matrix
EBR	Edge Bead Removal
ESC	Embryonic Stem Cell
FAK	Focal Adhesion Kinase
FITC	Fluorescein Isothiocyanate
FBS	Fetal Bovine Serum
Gag	Group Antigens
hESC	Human Embryonic Stem Cell
HDAC4	Histone Deacetylase 4
HeBS	HEPES Buffered Saline Solution
HEK	Human Embryonic Kidney
HEPES	4-(2-Hydroxyethyl)-1-Piperazineethanesulfonic Acid
HMDS	Hexamethyldisilazane
IMDM	Isocov’s Modified Dulbecco’s Medium
iPSC	Induced Pluripotent Stem Cell
Klf4	Krueppel-Like Factor 4
LIF	Leukemia Inhibitory Factor
MEF	Mouse Embryonic Fibroblast
mERF	Mouse Ear Fibroblast
mESC	Mouse Embryonic Stem Cell
MHC	Myosin Heavy Chain
MSC	Mesenchymal Stem Cell
MOI	Multiplicity of Infection
NEAA	Non-essential Amino Acids
Oct-3/4	Octamer-Binding Transcription Factor 3/4
OSKM	Oct-3/4, Sox2, Klf4, and c-Myc

PBS	Phosphate Buffer Solution
PCR	Polymerase Chain Reaction
PDMS	Polydimethylsiloxane
P/S	Penicillin/Streptomycin
Rev	Regulator of Virion Expression
S.E.M.	Standard Error of the Mean
SEM	Scanning Electron Microscope
Sox2	Sex Determining Region Y-Box 2
STEMCCA	Stem Cell Cassette
SUN	Sad1p, UNC-84
TC	Tissue Culture
TRITC	Tetramethyl Rhodamine Iso-Thiocyanate
VSVG	Vesicular Stomatitis Virus Glycoprotein
μDG_H	Microtopographic Durotaxis Gradient, High Gradient Strength
μDG_L	Microtopographic Durotaxis Gradient, Low Gradient Strength
μDSG	Microtopographic Durotaxis *versus* Spatiotaxis Gradient
μSG	Microtopographic Spacing Gradient
μVH	Microtopographic Constant Micropost Radius, Variable Micropost Height Array
μVR	Microtopographic Constant Micropost Height, Variable Micropost Radius Array
μVR_2	Microtopographic Constant 2 μm Micropost Height, Variable Micropost Radius Array
μVR_7	Microtopographic Constant 7 μm Micropost Height, Variable Micropost Radius Array
%ECM	Percentage of Extracellular Matrix Coverage

Chapter 1: Introduction

1.1 Effects of Microenvironmental Stimuli on Cellular Behavior

The driving force behind investigating biology and biology-related fields is to address the unmet medical needs of society. Humans are highly complex organisms with many system unknowns and interactions, [1,2] making biological questions some of the most challenging research faced today. To simplify the analysis of human systems, they can be reduced to components such as organ systems, organs, tissues, and cells (**Figure 1.1)**. This enables researchers to focus on system-level problems through the investigation of subsystems with fewer unknowns. This methodology of studying subsystems of the human body has revealed that medical diseases and conditions, which present at the macroscale in the form of patient symptoms, are actually a result of changes at the cellular level. [3–5]

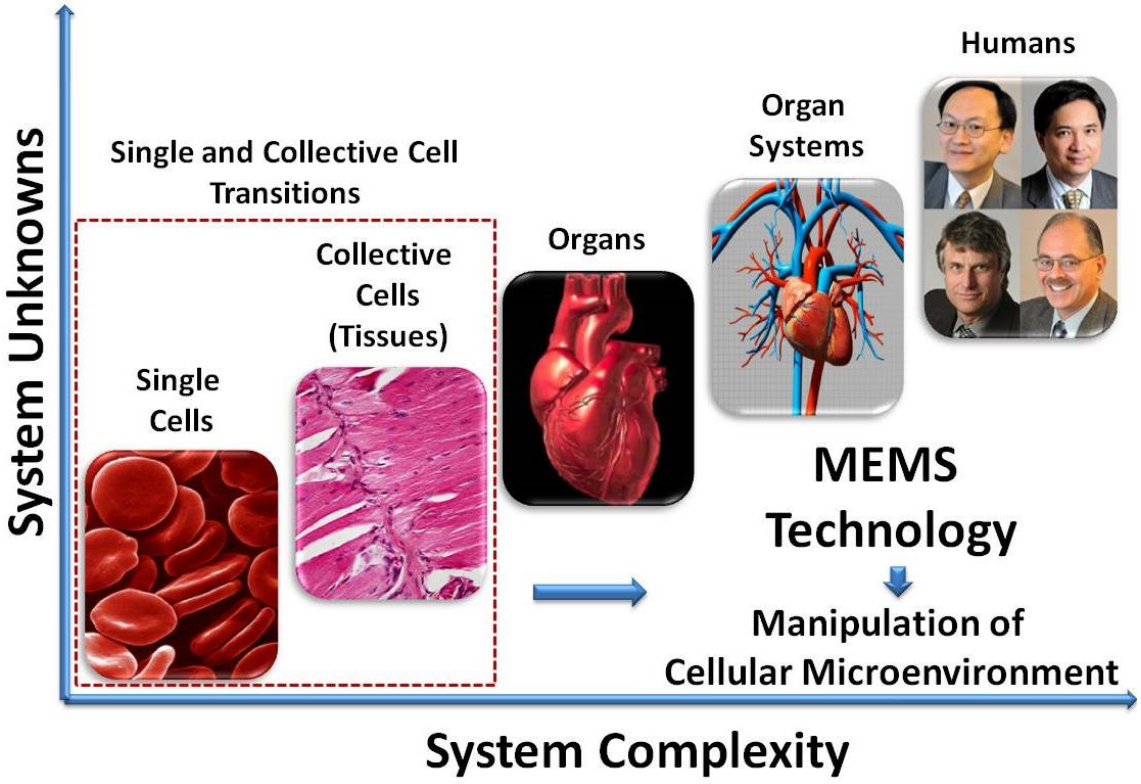

Figure 1.1. Subsystems of the human body.
Humans are highly complex organisms and must be broken down into subsystems to facilitate understanding. By reducing the subsystem complexity, the number of system unknowns is also reduced. For this reason, the field of biology has primarily focused on investigating single cell behavior. While single cells provide a strong foundation for biology, to advance to higher levels of complexity, group, or collective cell behavior and transitional behaviors, such as breakdown of collective cells and differentiation, must also be investigated as this area (*red box*) is critical to many growth and pathological biological phenomena. Both single and collective cells are highly influenced by their cellular microenvironments, making MEMS technology well suited for fabricating devices to study their behavior since many factors can be controlled precisely and repeatably at the microscale.

As shown in **Figure 1.1**, single cells are the simplest complete subsystem of the body and are the building blocks for all other human subsystems. As such, they have been the dominant focus of biology and have provided a robust foundation for the field. However, many growth and pathological conditions of the body are not confined to single cell behavior – they include group, or collective, cell behavior and transitions, such as breakdown of collective cells to single cells or differentiation, [6–8] shown in the red box of **Figure 1.1**. Therefore, investigation of what can affect any of these cell states is critical to understanding many biological phenomena.

Cues in the Cellular Microenvironment

Cellular behavior, at all levels of system organization, is highly regulated and influenced through stimuli, or cues, in the cellular microenvironment. [9] Understanding cellular responses to these cues, therefore, is crucial for practical applications in biology, including immune response, design of biomaterials, tissue engineering, and regenerative medicine, [10], [11] and makes microtechnologies well-suited for studying them (**Figure 1.1**). [12] These cues can be in many different forms, e.g. changes in soluble or immobilized chemicals, electric fields, temperature, and biophysical cues. Chemical cues, which are the most prevalent in the body, have been shown to influence many aspects of cellular behavior. These include spreading, [13] proliferation, [14], [15] motility, [16] differentiation, [17], [18] apoptosis, [19] and regulation at the tissue, organ, and organ system levels such as wound healing, increasing fluidic output of kidneys, and maintaining vascular tone. [1], [20], [21] Prior work has demonstrated cellular alignment and cytoskeleton reorganization to electrical fields, [22], [23] and effects of temperature on cellular growth. [24]

Considering that homeostasis of the body is strongly regulated by chemical cues, [1] these have been the dominant focus of research in the field of biology. However, to effectively reproduce the complexity of the *in vivo* chemical microenvironment is challenging. In addition to the numerous chemical cues that are present, [25] it is difficult to maintain such environments long-term as they require outside regulation or external power sources. [26–28] This can make their implementation in devices and in *in vivo* and *in vitro* application environments complicated and impractical. [29], [30]

Biophysical Cues and Mechanotransduction

While chemical cues remain the strongest regulators of cellular behavior, in the last 20 years, mechanical, or biophysical, cues have demonstrated increasing importance. Biophysical cues refer to the family of microenvironmental cues that can physically influence cellular behavior through mechanotransductive pathways. [31], [32] Many biological behaviors can be influenced by biophysical cues, such as motility, cell shape, growth, stem cell differentiation, and apoptosis, to name a few. [33–36] The direct physical changes that occur in cells through mechanotransduction can include reorganization of the cytoskeleton, modulation of attachment forces and protein dynamics, and activation/deactivation of enzymes. [37], [38] As shown in

Figure 1.2, biophysical cues can include shear forces from fluid flow in vessels, [33] tension and compression during movement, [39], [40] changes in substrate stiffness, [41] and spatial cues, such as extracellular matrix porosity. [42], [43]

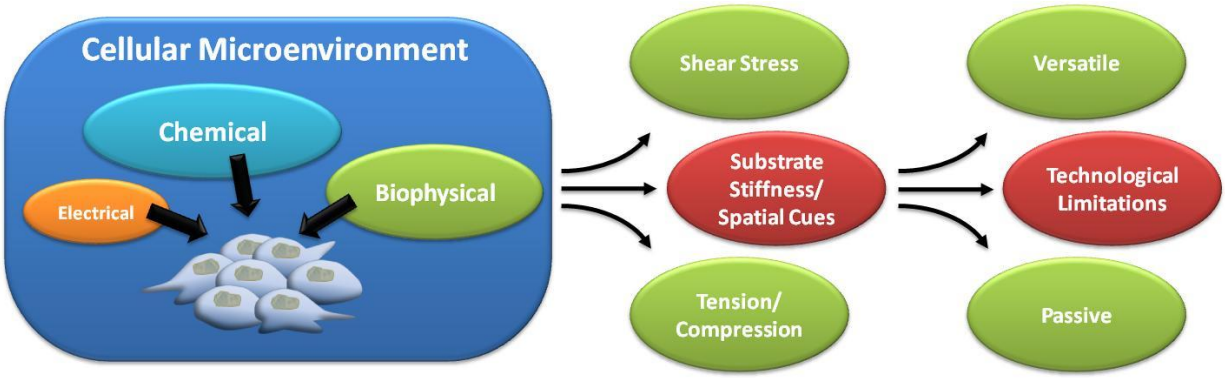

Figure 1.2. Biophysical cues in the cellular microenvironment.
Single and collective cell behaviors are highly regulated by stimuli, or cues, in their microenvironments, such as chemical, electrical, or mechanical cues. While chemicals are the primary modality by which the body maintains homeostasis, mechanical cues have recently demonstrated significant influence over cellular behavior. Mechanical cues, also known as biophysical cues, can be in the form of shear stress from fluid flow, tension or compression, substrate stiffness, and spatial cues. Passive biophysical cues, such as substrate stiffness and spatial cues, require no power or external regulation – this makes them ideal for implementation in devices.

These cues can be classified into two groups: *active* (green) and *passive* (red) (**Figure 1.2**). Active cues like shear stress and tension and compression are similar to chemical cues in that they require external regulation or power to maintain their efficacy. Conversely, substrate stiffness and spatial cues are *passive* stimuli as their properties are not transient. *Passive* biophysical cues are versatile stimuli capable of regulating many cellular functions. [36], [41], [44–46] While they are potentially simpler to reproduce *in vitro* than *active* cues, controlling them repeatably and accurately at the microscale has remained a challenge. [47–49]

1.2 Regulation of Cellular Behavior Through Microtopography

Considering that the cellular microenvironment is incredibly complex, technologies and methodologies that are capable of effectively producing isolated stimuli are necessary for studying and inducing desired cellular responses. Substrate-based methods have been demonstrated as powerful platforms for changing the biophysical stimuli in the cellular microenvironment. In addition to influencing processes such as, cell growth and proliferation, and development of cell-substrate junctions, [50–53] substrate stiffness has been shown to affect cellular migration, [54] collective cell behavior, [55] and stem cell lineage specification. [46], [56] Current methods of adjusting the biophysical properties of surfaces for cells utilize various types of polymers, such as hydrogels, polyacrylamide gels, and photopolymers, which rely on

polymer cross-linking density to modulate substrate stiffness. Although these methods are capable of generating continuous surfaces with uniform or gradients of substrate stiffness for cells, they suffer from many disadvantages. In addition to low repeatability, complicated fabrication processes, and poor user control over the placement and magnitude of substrate stiffness, [47], [49], [57], [58] surfaces produced via these methods are difficult to characterize and may have different chemical and porosity characteristics at their surfaces. [56]

Substrate-based methods of producing biophysical stimuli could provide systematic information and results by utilizing microfabrication techniques. Microfabrication processes are well-characterized, and can be used to control many factors at the microscale with high accuracy and repeatability. [56], [59–61] Spatial and geometric (stiffness) variations in microstructures, which can be simply fabricated, have the potential of systematically studying cellular behaviors affected by passive, substrate-based biophysical cues. Microtopography has been used to influence many aspects of cellular behavior, including alignment and growth, [62], [63] cellular migration, [64–66] traction forces, [67], [68] restriction of cell movement, [69] and differentiation of stem cells. [56], [70]

Microtopographic substrates have demonstrated their capabilities of regulating cellular behavior, but have not been designed to preclude effects of gradients or changes in immobilized chemicals and topographical surface areas (availability of attachment points). [67], [71] Micropost arrays, due to their unique ability to discretized the apparent stiffness and spacing of attachment points of a surface, offer a robust technique to study these effects independently. Recently, researchers have used uniform micropost arrays as force sensors to determine traction forces of cells (**Figure 1.3**). Each micropost can be modeled as a cantilever using Euler Bernoulli and Timoshenko shear beam theory [72] to derive a bending stiffness at the top of the microposts that is a function of its material properties and geometry (radius, r, and height, H). [61], [67], [73] In **Figure 1.3**-*left*, the material properties of the micropost, κ, E, and G, are the Timoshenko shear coefficient, the elastic modulus, and the shear modulus, respectively. When cells are seeded onto these surfaces, they form cell-substrate junctions and deform the micropost through their stochastic contractions, illustrated by the bovine aortic endothelial cell (BAEC) on the micropost array in **Figure 1.3**-*right*. The deformation of the top surfaces, δ, due to traction forces exerted by cells, F, can be visually measured and compared to the location of the bases of the microposts. This deformation can then be used in the derived bending stiffness equation to calculate corresponding traction forces, as shown in **Figure 1.3**-*left*.

As the bending stiffness of the microposts can be controlled by their radii and height, micropost arrays that change the apparent uniform and gradient stiffness of a substrate can be designed by simply modulating their geometry. This enables an engineering technique of controlling the apparent stiffness of a substrate in a precise and repeatable fashion. Furthermore, since the interpost spacing can be adjust independently of the micropost stiffnesses, effects of spacing on cellular behavior can be explored as well.

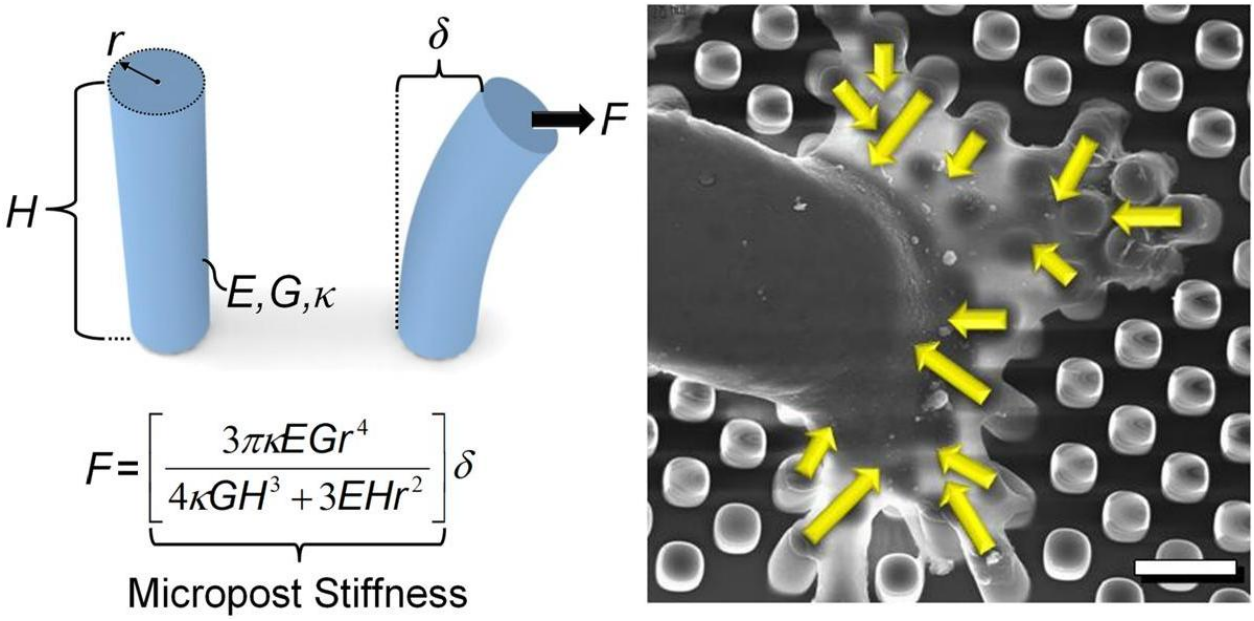

Figure 1.3. Micropost array theory.
(*Left*) Historically, micropost arrays have been used to detect cellular traction forces. Microposts can be modeled as cantilevers using Euler Bernoulli and Timoshenko shear beam theory to derive a bending stiffness at the top surface that is a function of its material and geometric properties. The material properties, κ, E, and G, are the Timoshenko shear coefficient, elastic modulus, and shear modulus, respectively. The geometric properties, r and H, are the micropost radius and height. When cells are placed on micropost arrays, they form cell-substrate attachments and can deform the microposts during movement. By measuring the displacement of the top surfaces of microposts relative to their bases, corresponding cellular traction force values can be calculated. (*Right*) A bovine aortic endothelial cell (BAEC) attached to a micropost array substrate. The deformation at the top surface of the micropost caused by cellular contractions can be visually measured and used to calculate traction forces through the bending stiffness equation. For this cell, forces range from 11-26 nN. Bar = 10 μm

1.3 Cellular Mechanotransduction by Microfabricated Post Arrays

In this body of work, new devices and methods for regulating biophysical properties of the cellular microenvironment through microtopography are described. Specifically, devices created from arrays of circular microposts were used to modulate: (*i*) the apparent stiffness of a substrate, and (*ii*) the distance between available cellular attachment sites. This was achieved by changing the geometry of microposts through the adjustment of radii or heights and the interpost spacing in an array, respectively. Given that the physical properties of micropost arrays are geometrically defined, these were simply and repeatably fabricated through standard one mask soft-lithography microfabrication processes.

Three areas of cellular behavior were explored using these micropost arrays to modulate the biophysical properties of the cellular microenvironment: (*i*) single cell motility, (*ii*)

maintenance or inhibition of collective cell behavior, and (*iii*) possible effects on the reprogramming and differentiation of induced pluripotent stem cells (iPSCs). These are illustrated and detailed in **Figure 1.4**.

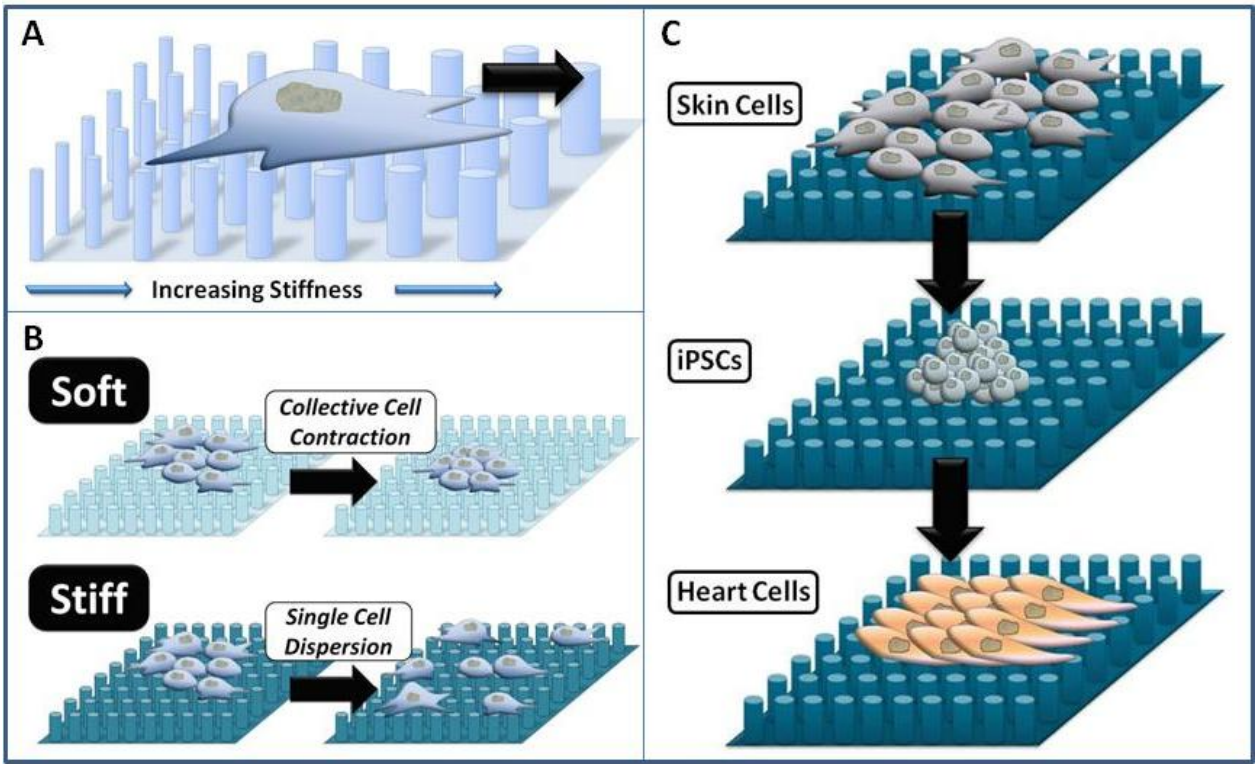

Figure 1.4. Micropost arrays for mechanically inducing cellular behavior.
(*A*) Micropost array gradients for inducing unidirectional single cell migration. Microscale gradients in stiffness and spacing between attachment points were achieved by increasing the radii and interpost spacing of the microposts over the length of the array. These substrates were used to observe cellular durotaxis and spatiotaxis. (*B*) Uniform and gradient micropost arrays of variable radii and heights for investigating collective cell behavior in response to changes in apparent substrate stiffness and microtopographic spacing. Collectives of cells were directly cultured on variable geometry micropost surfaces using a thin-film stenciling technique akin to metal lift-off. (C) Uniform micropost arrays of variable radius and height for influencing the reprogramming of mouse ear fibroblasts (mERFs) into induced pluripotent stem cells (iPSCs) and possibly their differentiation. Using varying initial seeding densities and lentiviral infection levels, mERFs were seeded and incubated on surfaces of different microtopography. Cellular reprogramming and differentiation behavior was observed over time.

For single cell motility studies, the effects of microscale gradients (**Figure 1.4.A**), on single BAECs was quantified by tracking their migration over 18-hour time-lapse experiments. The microscale gradients were created by varying the radii and interpost spacing of microposts along the length of arrays. Both unidirectional migration based on stiffness, or durotaxis, [54] and on spacing between attachment points, a phenomenon herein referred to as spatiotaxis, were observed. This is the first time either phenomenon has been induced using microtopography.

Collective cell behavior, which is the true working mechanism behind many biological phenomena, has largely been unexplored, particularly in the realm of biophysical cues. [74] Here, cell collectives were directly formed on uniform and gradient micropost arrays using a thin-film stenciling method (**Figure 1.4.B**) similar to metal lift-off techniques of microfabrication. The maintenance or inhibition of BAEC collective behavior was quantified by measuring their expanded or contracted area over the course of 16-hour experiments. Thresholds of apparent substrate stiffness where collective cell behavior could no longer be maintained were characterized for multiple micropost geometries. This marks the first demonstration of using microtopographic features to biophysically regulate the maintenance or inhibition of collective cell behavior.

Finally, the reprogramming and differentiation of iPSCs has largely been investigated in the context of chemical microenvironmental cues. There are currently no studies in the literature that demonstrate biophysical influence over these processes. Mouse ear fibroblasts (mERFs) were reprogrammed and differentiated on surfaces of varying microtopography, and effects of initial cell seeding densities and lentiviral infection levels were also investigated (**Figure 1.4.C**). Preliminary results demonstrate possible influence of microtopography on colony formation and iPSC differentiation for the first time.

1.4 Dissertation Outline

In **Chapter 2**, the design and fabrication of micropost arrays is investigated as a means of influencing unidirectional migration of single cells. Micropost arrays are utilized as a method of controlling the biophysical cues within the cellular microenvironment through microscale stiffness and spacing gradients, to induce durotaxis and spatiotaxis, respectively. In addition to prior research efforts for regulating cellular motility through mechanotaxis, the section will include how micropost arrays have been implemented and developed within this research area. Two micropost array gradients will be presented: (*i*) microtopographic durotaxis gradients (*μDGs*) and (*ii*) microtopographic durotaxis *versus* spatiotaxis gradients (*μDSGs*). The microfabrication of the micropost arrays, cell culturing techniques, and methods for collecting and quantifying cellular behavior will be described. Experimental cell migration results will be covered and discussed.

In **Chapter 3**, the implementation of micropost array technology for the mechanical regulation of group, or collective, cell behavior is presented. In this work, both uniform and gradient micropost arrays are investigated for maintaining or inhibiting collective cell behavior. An overview of prior work in regulating collective cell behavior through chemical and biophysical cues will be included. Two sets of uniform micropost arrays for modulating the apparent substrate stiffness will be explored: (*i*) microtopographic constant micropost height, variable micropost radius arrays (*μVRs*), and (*ii*) microtopographic constant micropost radius,

variable height arrays (*μVHs*). Additionally, microtopographic spacing gradients (*μSGs*) will be used to study possible effects of micropost spacing on collective cell behavior. The methodology for culturing collectives of cells through thin-film stencils will be described, as well as microfabrication of the micropost arrays, data acquisition and processing, and cell analysis techniques. The experimental results will be reviewed and discussed.

In **Chapter 4**, the micropost array substrates will be extended for studying possible effects of microtopography on the reprogramming and differentiation of induced pluripotent stem cells (iPSCs). Prior work in controlling the reprogramming and differentiation processes of iPSCs will be covered, with an emphasis on chemical methods as no previous research has demonstrated influence of biophysical cues on iPSCs. As preliminary work in this field, this section will focus on summarizing the results of experiments investigating effects of initial cell seeding densities, lentivirus infection levels, and surface microtopography on the reprogramming and differentiation processes. The design and microfabrication of the micropost arrays, cell culturing methods, and cell analysis techniques will be detailed. Preliminary experimental results will be summarized and discussed.

This dissertation will be concluded in **Chapter 5**. This section will review the major findings for all applications of the uniform and gradient micropost array substrates. The implications of these results and future directions will be explored.

Chapter 2: Micropost Array Gradients for Single Cell Migration

2.1 Introduction

This chapter focuses on utilizing micropost array gradients as a means to study single cell behavior in response to specific, passive biophysical information. The changes in apparent substrate stiffness and variable spacing of available attachment sites are intended to passively guide unidirectional migration of single cells.

Microenvironmental Cues and Single Cell Migration

Microenvironmental cues, specifically chemical, [16], [26], [28], [29], [75] electrical, [76–78] thermal, [79] and biophysical, [48], [54], [80], [81] have been shown to influence migration of single cells. These cues affect various stages of cellular migration, which is a combination of stochastic protrusive activity, attachment to substrates through dominant protrusions, and detachment and contraction of the trailing edge.[28], [82] For investigation and artificially controlling cellular migration, these different microenvironmental stimuli offer many modalities to device designers. [83] However, as previously discussed, passive biophysical cues offer many advantages over other microenvironmental stimuli – they do not require external regulation or power to maintain their efficacy.

Cell motility in response to biophysical cues is known as the phenomenon of mechanotaxis. [84] Mechanotaxis can be induced through shear and tensile stress, [85–87] as well as gradients in substrate stiffness. [41], [48] Substrate stiffness, which is a passive biophysical cue, has been demonstrated as a versatile regulator of single cell behavior and cellular migration based on gradients of substrate stiffness is the phenomenon known as durotaxis. [38], [41] Researchers have demonstrated and investigated this phenomenon by creating substrates with stiffness gradients through the manipulation of photopolymerized hydrogels. [47], [49], [57], [88], [89] Substrates that have few distinct substrate stiffnesses have been fabricated, but are limited due to their small range of stiffnesses, as well as the fact that the critical dimensions of the stiffness steps are far greater than that of cells. [88], [89] Cells, therefore, have difficulty in sensing stiffness changes in their microenvironments. Using complex microfluidic systems and diffusion-based methods, substrates with many distinct substrate stiffnesses have been achieved. These systems are difficult to fabricate, have low repeatability, and have poor user control over the placement and magnitude of stiffnesses. [47–49], [57]

Microtopography and Single Cell Migration

Microtopographic techniques have demonstrated influence over cellular motility. Prior work has utilized microridges and microposts for studies on bidirectional single cell migration. On microridges, cells could migrate freely along the length of the microgrooves (**Figure 2.1-**

left). [66] This behavior has been replicated using elliptical micropost arrays, where cells preferentially migrated along the direction of the major axis of the microposts (**Figure 2.1**-*right*). [59], [90] The elliptical nature of the microposts yield different bending stiffnesses parallel (stiffer) and perpendicular (softer) to the major axis, and cells likely migrated along the major axis direction due to a preference for stiffer surfaces. While illustrative of the potential for inducing directional migration, microtopographic methods have not been capable of unidirectional migration without the aid of immobilized chemical gradients or increased topographical surface area (availability of attachment sites). [67], [71]

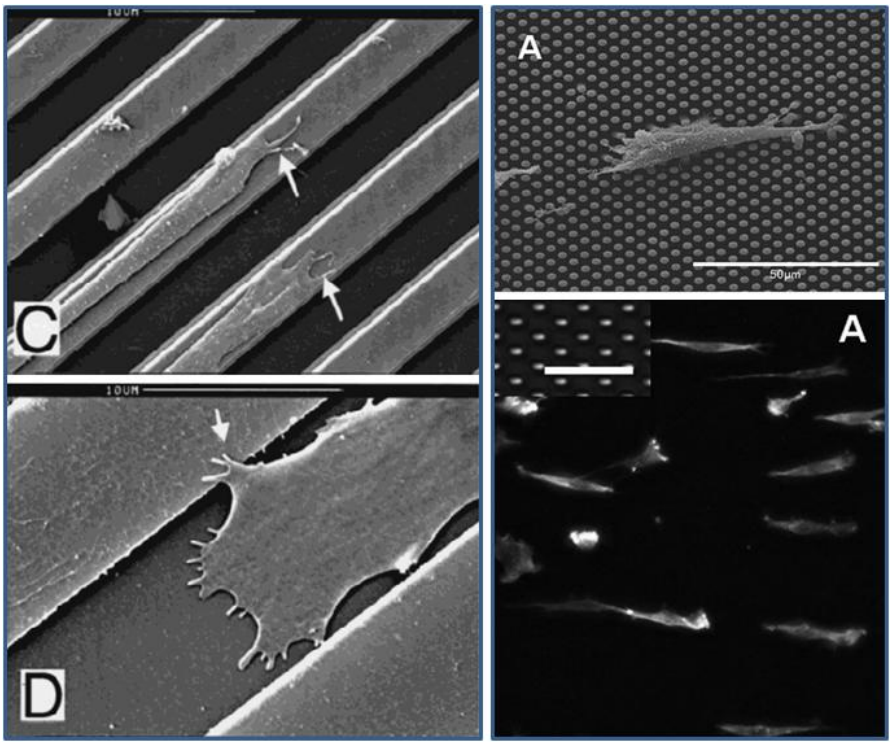

Figure 2.1. Bidirectional guidance of cellular migration via microtopography.
Microtopography, such as microgrooves (*left*) [66] and elliptical micropost (*right*) [90], has been used to influence cellular migration. Cells moved bidirectionally along the length of the microgrooves and parallel to the direction of the major axes of the elliptical microposts.

2.2 Design of Micropost Array Gradients in Stiffness and Spacing

As discretized surfaces, micropost arrays have the ability to modulate the apparent stiffness of a substrate, as well as the distance between possible attachment sites for cellular motility studies. These biophysical cues can influence two aspects necessary for cellular migration: cell-substrate attachments and lamellipodia. This section describes the fabrication of microscale gradients in stiffness and spacing based on the geometric regulation of micropost arrays. Through gradients in stiffness and spacing, the micropost arrays are described as a methodology for inducing unidirectional migration of single cells due to the migration phenomena of durotaxis and spatiotaxis, respectively. Two types of circular micropost arrays

were designed: microtopographic durotaxis gradients (*μDGs*) and microtopgraphical durotaxis *verses* spatiotaxis gradients (*μDSGs*).

2.2.1 Microtopographic Durotaxis Gradients (*μDGs)*

As a technique to create microscale stiffness gradients, the *μDGs* were designed by changing the geometry of the microposts unidirectionally along a single axis of an array. Although the micropost stiffness can be modulated by either the height or the radius, the height was kept at a constant 7 μm while the radius was adjusted to enable a simpler, one-mask soft lithography fabrication process. **Figure 2.2** illustrates the concept of the *μDGs*. The interpost spacing between microposts of different radii was maintained at a constant 2 μm.

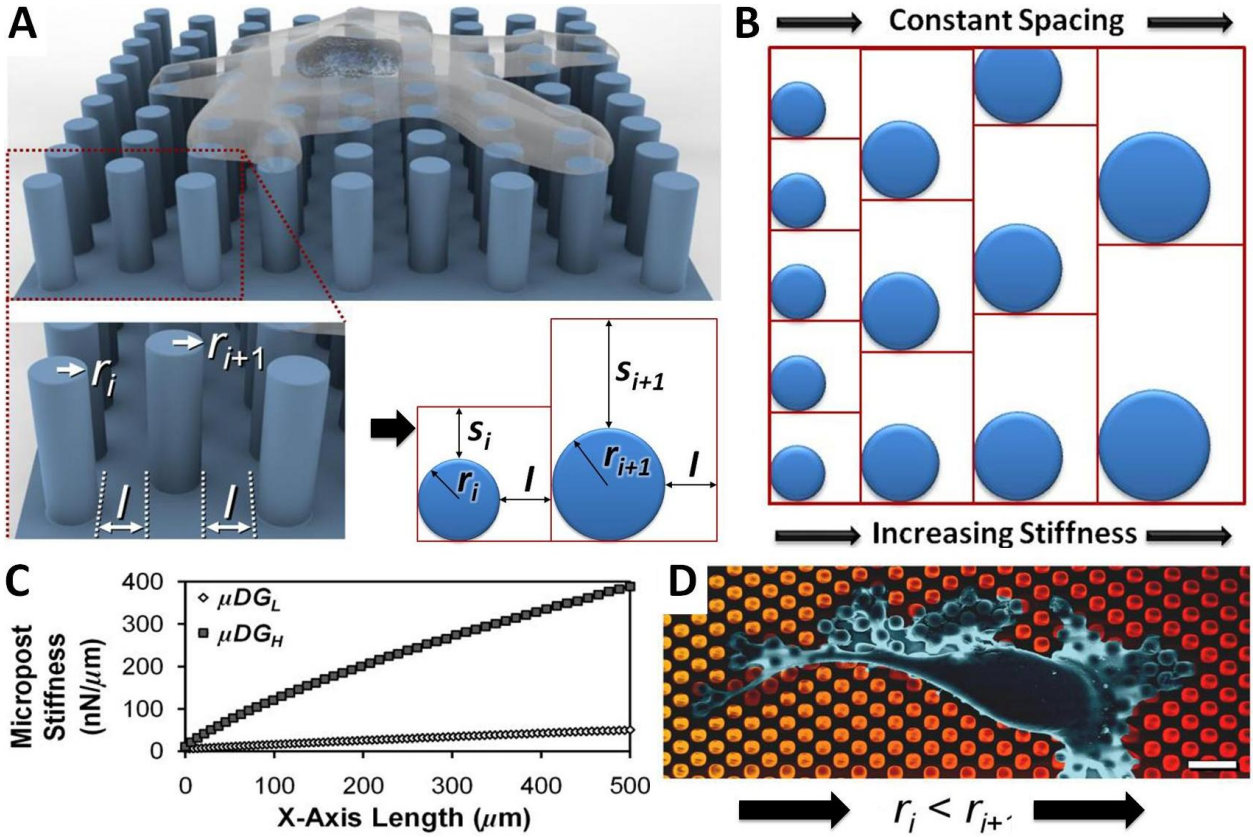

Figure 2.2. Concept schematic for the microtopographic durotaxis gradient (*μDG*).

(*A*) For the *μDGs*, the radii, *r*, of the microposts increase unidirectionally over the length of the array, while the interpost spacing along the axis of increasing stiffness, *I*, remains at a constant 2 μm. The bottom right figure shows the spacing schemes governed by **Equation 2.1**. This equation dictates that the ratio of micropost topographic surface area to a corresponding unit cell must remain constant for microposts of different radii. Given that the interpost spacing is fixed, the interpost spacing in the direction perpendicular to the direction of increasing stiffness, *s*, must increase to compensate. (*B*) Schematic top view of the *μDG*, with increasing micropost radii (stiffness) and constant interpost spacing. (*C*) Ranges of theoretical stiffness for the μDG_L and μDG_H over the length of the array. (*D*) A false colored SEM micrograph of a BAEC on a *μDG* illustrates a changing geometry with changing column color. Bar = 10 μm

Two gradient strengths in the range of physiologically relevant stiffnesses [67], a low strength gradient (μDG_L) and a high strength gradient (μDG_H), were created to investigate the possible effects. The μDG_L had an increase in post-to-post stiffness of 0.5 nN/μm with a stiffness range of 5 to 50 nN/μm for radii between 1 to 2 μm. The μDG_H had an increase in post-to-post stiffness of 7.5 nN/μm, which is 15 times greater than the μDG_L. The μDG_H had a stiffness range of 5 to 390 nN/μm for radii in the range of 1 to 3 μm. Since the microposts had aspect ratios of less than 1:10 (width to length), the equation used to describe the micropost bending stiffness was derived using Euler Bernoulli and Timoshenko shear beam theory. To accommodate the stiffness limits and increments, the micropost array gradients had overall areas approximately 500 x 500 μm^2, and consisted of thousands of features. The microposts were designed to be much smaller than the size of cells, such that cells would be able to interact with a range of microposts to experience different stiffnesses. To increase attachment to the surfaces of the microposts, the *μDGs* were coated with extracellular matrix attachment proteins (ECM).

Non-uniformities in both the topographical surface area for substrate-immobilized chemicals should be eliminated or minimized in the micropost gradient arrays to avoid possible chemical cues influencing cellular migration. To preclude possible effects of these non-uniformities, microposts were designed such that the ratio (*%ECM*) of the micropost topographical surface area to the area of their corresponding unit cell remained constant for different micropost stiffnesses. As illustrated in **Figure 2.2.A**, to account for the constant 2 μm interpost spacing, the interpost spacing perpendicular to the axis of increasing stiffness was proportionally increased for increasing micropost radii. Spacing schemes were governed by:

$$\%ECM = \frac{\pi r^2}{(2r+s)(2r+l)} = \text{Constant} \qquad \textbf{Equation 2.1}$$

where r is the micropost radius, s is the interpost spacing perpendicular to the axis of increasing stiffness, and I is the interpost spacing parallel to the axis of increasing stiffness. A top view schematic of the *μDGs* can be found in **Figure 2.2.B**, illustrating constant interpost spacing and increasing micropost radii (stiffness) in the rightward direction. **Figure 2.2.C** shows the ranges of theoretical stiffnesses for the μDG_L and μDG_H over the length of the arrays. Specifically, for all *μDGs*, the *%ECM* was held constant at 0.2 to minimize differences between the low and high gradient strengths. In **Figure 2.2.D**, a false colored SEM micrograph of a BAEC on a *μDG* illustrates changes in the geometry of the microposts, and therefore stiffness, with changing column color.

2.2.2 Microtopographic Durotaxis *versus* Spatiotaxis Gradients (*μDSGs*)

Since substrate stiffness and the spacing between attachments points can possibly affect different steps of cellular migration, micropost arrays with gradients in substrate stiffness and in interpost spacing should be designed and studied. **Figure 2.3.A** illustrates a specific design where both the radii and interpost spacing of the microposts are increased unidirectionally along

an axis. The ranges for interpost spacing and micropost stiffness and spacing scheme can be found in **Figure 2.3.B**.

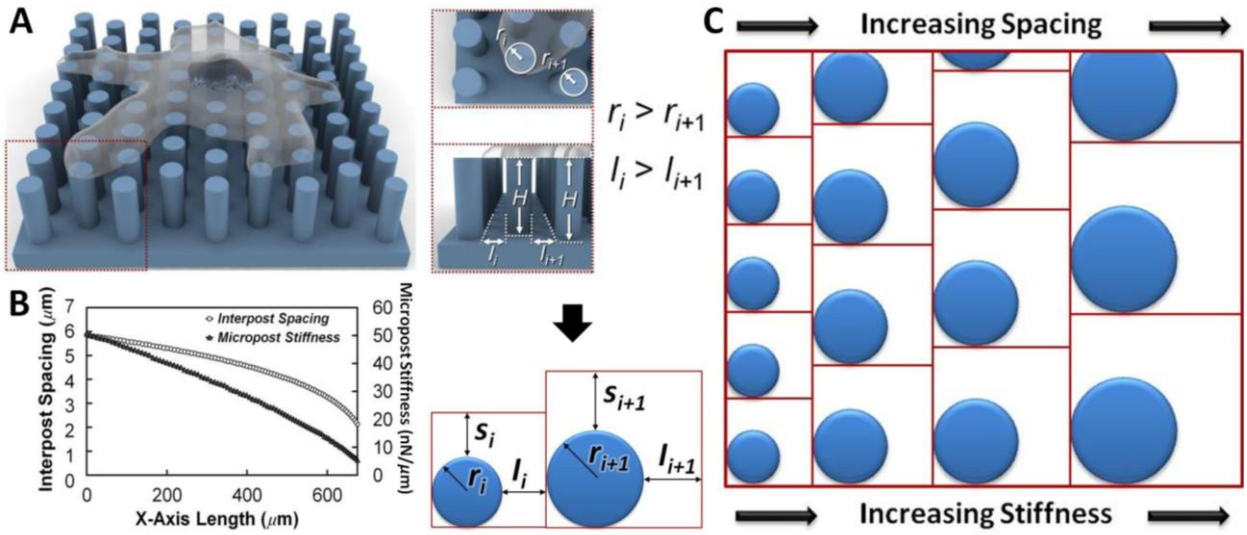

Figure 2.3. Concept schematic for the microtopographic durotaxis *versus* spatiotaxis gradient (*μDSG*)

(*A*) For the *μDSG*, the radii, *r*, and interpost spacing along the axis of increasing stiffness, *I*, of the microposts increased unidirectionally in parallel. (*B*) Ranges of micropost stiffness and interpost spacing for the *μDSG* over the course of the array. The right figure illustrates the spacing schemes for increasing radii dictated by **Equation 2.1**. To maintain continuity with the *μDGs*, the *%ECM* was held at 0.2. However, since *I* was not constrained, the interpost spacing was increased uniformly in the directions parallel (*I*) and perpendicular (*s*) to the axis of increasing stiffness with increasing radius, making *I* equal to *s*. (*C*) Schematic of the top view of the *μDSG* with increasing micropost radii (stiffnesses) and increasing interpost spacing.

Similar to the *μDGs*, the heights of all the microposts were kept at a constant 7 μm. Using a *%ECM* value of 0.2, the interpost spacing values corresponding to increasing radii were calculated using **Equation 2.1**. For these microposts and their corresponding unit cells, the spacing parallel and perpendicular to the gradient were increased uniformly with increasing radius, therefore making *s* equal to *I*. This resulted in micropost gradients with radii and interpost spacing increasing in the same direction along an axis. The range of interpost spacing was between 2 to 6 μm, with an average increment of 40 nm. For comparison purposes, the micropost radii used were identical to the μDG_L, in the range of 1 to 2 μm. A top view schematic of the *μDSGs* can be found in **Figure 2.3.C**, where interpost spacing and micropost stiffness increase simultaneously.

2.3 Materials and Methods

2.3.1 Microfabrication and Preparation

Micropost array gradient substrates were fabricated using a one mask soft-lithography process. Feature heights of 7 μm were targeted for all single cell migration studies.

Spin-coating Wafers

To create the micropost array substrates, silicon n-type test wafers (4") were cleaned in piranha for 10 minutes, rinsed in DI water, and spun dry (*msink8*). To enhance adhesion of photoresist to the silicon wafers, the clean wafers were treated with HMDS in *primeoven*. Following HMDS treatment, the wafers are spin-coated with Megaposit SPR-220 i-line positive photoresist (*Rohm and Haas Company, PA, USA*) using the following custom program (*coater program 7*) on *svgcoat2*:

Event	***Oper***	***Arm***	***Time***	***Speed***	***Accel***
1	SPIN	0	10.0	0.00	20
2	DSP3	8	--	0.00	20
3	SPIN	0	3.0	0.30	50
4	SPIN	0	3.0	0.50	50
5	SPIN	0	3.0	1.00	50
6	SPIN	0	3.0	3.00	50
7	SPIN	0	30.0	***X***	50
8	END	--	--	--	--

where *X* is the desired RPM based on the calibration curve in **Figure 2.4**.

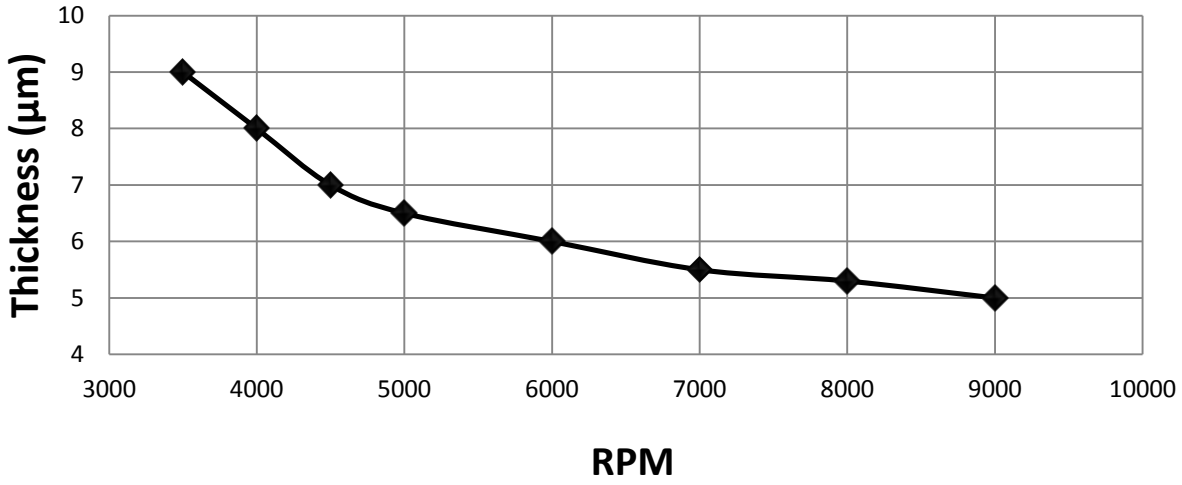

Figure 2.4. SPR-220 spin-coating calibration curve.
The manufacturer's specifications were not accurate for spin-coating SPR-220 on svgcoat2. These values are to be used during *Event 7* of the aforementioned custom program.

After coating, the wafers were run through EBR on *svgcoat2* to remove edge resist. Failure to do this resulted in poor transferring and alignment problems with *gcaws2* due to edge roughness and adhesion from residual SPR-220. To soft bake, the wafers were held at 115°C for 5 minutes on a hot plate and thicknesses are confirmed with *asiq* or *nanospec*. As RPMs of 8000-9000 are reached, the coating can become very uneven, with in-wafer variation in thicknesses as high as 0.5 μm. Before exposure, the coated wafers sat at room temperature for 30-60 minutes to allow the photoresist to stabilize. Failure to do this led to cracking during the subsequent processing steps.

Exposure, Development, and PDMS Micromolding

To pattern the photoresist, the coated wafers were exposed using chrome masks (*Fineline Imaging, CO, USA*) on *gcaws2* (projection lithography, 10:1 reduction) with the EXPO EXPO program:

- Program Row (R) allows up to a 7 x 7 matrix with seven exposure times (columns) and seven offsets (rows). For rectangular devices approximately 1 cm^2 in area, 7 x 7 are the maximum number of devices that can fit onto a 4" wafer. The actual yield is 45 devices, as the corners of the array do not fit completely onto the wafer surface. Offsets are integral to yield straight side walls, since the micropost heights can exceed the theoretical depth of focus of 5.56 μm. Offset values between -3 and -12 (-4 is roughly equivalent to 1 μm) can yield straight side walls for SPR-220 thicknesses of 5-7 μm.
- Program Exposure (E) allows a user definable matrix (up to 7 x 7) with incremented exposure times at a specified offset. Exposure times of 0.5-0.56 seconds can fully expose SPR-220 thicknesses of 5-7 μm.

For post-exposure bake, the wafers were held at 115°C for 6.5 minutes on a hot plate and cooled to room temperature completely for a minimum of 5 minutes. If the wafers were not fully cooled, the photoresist could crack or delaminate during the development process. Developers, such as LDD-26W or MF-26A (*Shipley Europe Ltd, UK*), can be used for SPR-220 development. SPR-220 forms large particulates during development that can prevent mass transfer of the developer to the exposed photoresist. To fully and cleanly develop the exposed patterns, the wafers should periodically be agitated during the 13-15 minutes development period. Following development, the wafers were rinsed thoroughly with DI water and dried with compressed N_2. Failure to clean these surfaces can result in stronger adhesion between Sylgard 184 polydimethylsiloxane (PDMS) (*Dow Corning Corporation, MI, USA*) and the SPR-220 micromolds. The wafers were hard baked at 80°C for 20 minutes and then treated with HMDS in *primeoven*. This second HMDS treatment was initially intended to form a release layer on the photoresist. While the releasing properties of HMDS were not necessarily ideal, the heating and dehydration steps during HMDS deposition significantly reduced any photoresist delamination during the demolding process of PDMS substrates. After cooling the wafers to room temperature, the wafers were silanized with Trichloro(1H,1H,2H,2H-perfluorooctyl) silane (*Sigma-Aldrich, MO, USA*). About 100 μl was used per wafer, and the silane was allowed to evaporate overnight in a fume hood to form a release layer.

Once the wafers were silanized, PDMS, mixed at a 10:1 w/w ratio, was poured onto the wafers. For the 5" square Greiner petri dishes, 30 g of PDMS will create devices ~3-4 mm in thickness. The wafers were then cured at room temperature under vacuum on a level surface for a minimum of 2 days before demolding.

Micropost array preparation

After curing, the PDMS substrates were demolded by cutting the PDMS with scalpels, and were cleaned of any residual photoresist by sonicating in 100% ethanol for 10 minutes. The substrates were then rinsed with DI water twice, and dried thoroughly using an aspirator. To render the substrates hydrophilic, they were O_2 plasma-treated for 2-3 minutes. It is particularly important to remove all water and/or ethanol, as they can attenuate the O_2 plasma treatment.

Microcontact-printing

Microcontact-printing stamps were made by incubating cleaned flat pieces of PDMS with a fibronectin solution (*Invitrogen, NY, USA*), diluted to a concentration of 50 μg/ml in DI water, for one hour. About 250 μl of solution was used for each stamp, yielding a final protein density of approximately 12.5 $\mu g/cm^2$. Before use, the stamps were rinsed twice in sterile DI water and dried using an aspirator to rid the surfaces of any particulates. Following the O_2 plasma-treatment (*RTE73 AMNS-500-E, Plasma Therm, FL, USA*) of the micropost array substrates, the dried stamps were placed in contact with the substrates for a minimum of 20 minutes. After stamp removal, the micropost array substrates were washed for one minute intervals in 70%

ethanol and twice in sterile DI water. To prevent attachment of the cells to the microposts in places other than the top surfaces, the micropost array substrates were incubated in a 0.2% Pluronic® F-127 (*Sigma-Aldrich, Corp., MO, USA*) solution for 30 minutes. The substrates were then washed for one minute and stored in sterile PBS in an incubator prior to use. The entire fabrication process for the micropost array substrates is shown in **Figure 2.5**.

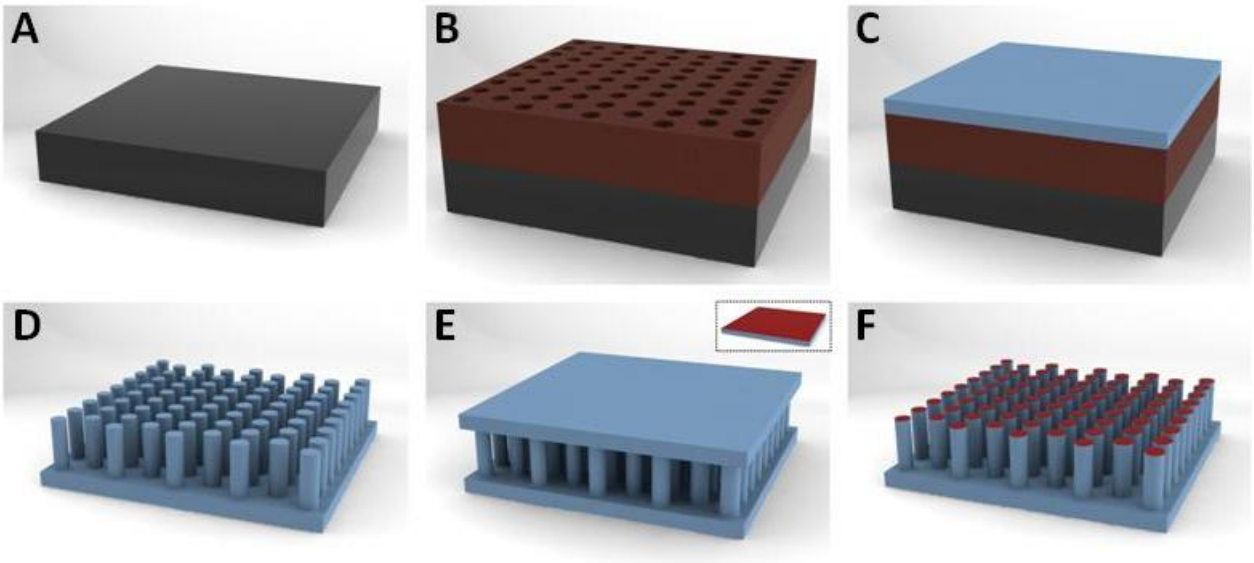

Figure 2.5. Fabrication process flow for the micropost array substrates.
(*A*) Silicon wafers were cleaned and (*B*) spin-coated with SPR-220 to a thickness of 7 μm. The SPR-220 was processed, exposed, and developed before silanization. (*C*) PDMS, mixed at 1:10 w/w ratio, was poured onto the wafers and allowed to cure under vacuum, to prevent bubbles, at room temperature for a minimum of two days. (*D*) The micropost array substrates were demolded, sonicated in ethanol, and O_2 plasma-treated before (*E*) microcontact-printing the top surfaces with fibronectin. (*F*) The substrates were sterilized and treated with a surfactant before using them for cellular studies.

2.3.2 Cell Preparation for Single Cell Migration Studies

Bovine aortic endothelial cells (BAECs) were used for all single cell experiments in this chapter. All BAEC cell lines were sourced from lines isolated in a tissue culture laboratory. BAECs were maintained in Dulbecco's Modified Eagle Medium (DMEM) supplemented with 10% fetal bovine serum (FBS), and 1% penicillin/streptomycin (P/S) (all *Gibco, Invitrogen, NY, USA*). Cells used in all experiments were within passages 5-15. Using standard cell culturing and sterile techniques, plated BAECs in 10 cm TC dishes were washed with 6 ml of PBS and trypsinized using 2 ml of 1x Trypsin (*Gibco, Invitrogen, NY, USA*) for 5 minutes. After neutralizing the Trypsin with 6 ml of DMEM, the cells were manually pipetted to minimize clusters of cells, and subsequently spun down in a centrifuge at 1000 RPM for 4 minutes. The media was aspirated and replaced before dilution. For single cell studies, the cells were

resuspended and diluted to a target concentration of 180 cells/μl. Approximately 30-40 μl of cells were placed onto the surfaces, or about 5400-7200 cells/cm^2.

2.3.3 Methods for Observing and Analyzing Single Cell Migration

Time-lapse Microscopy

Before seeding, the micropost array substrates were secured and placed in custom fixtures for viewing on inverted microscopes (**Figure 2.6**).

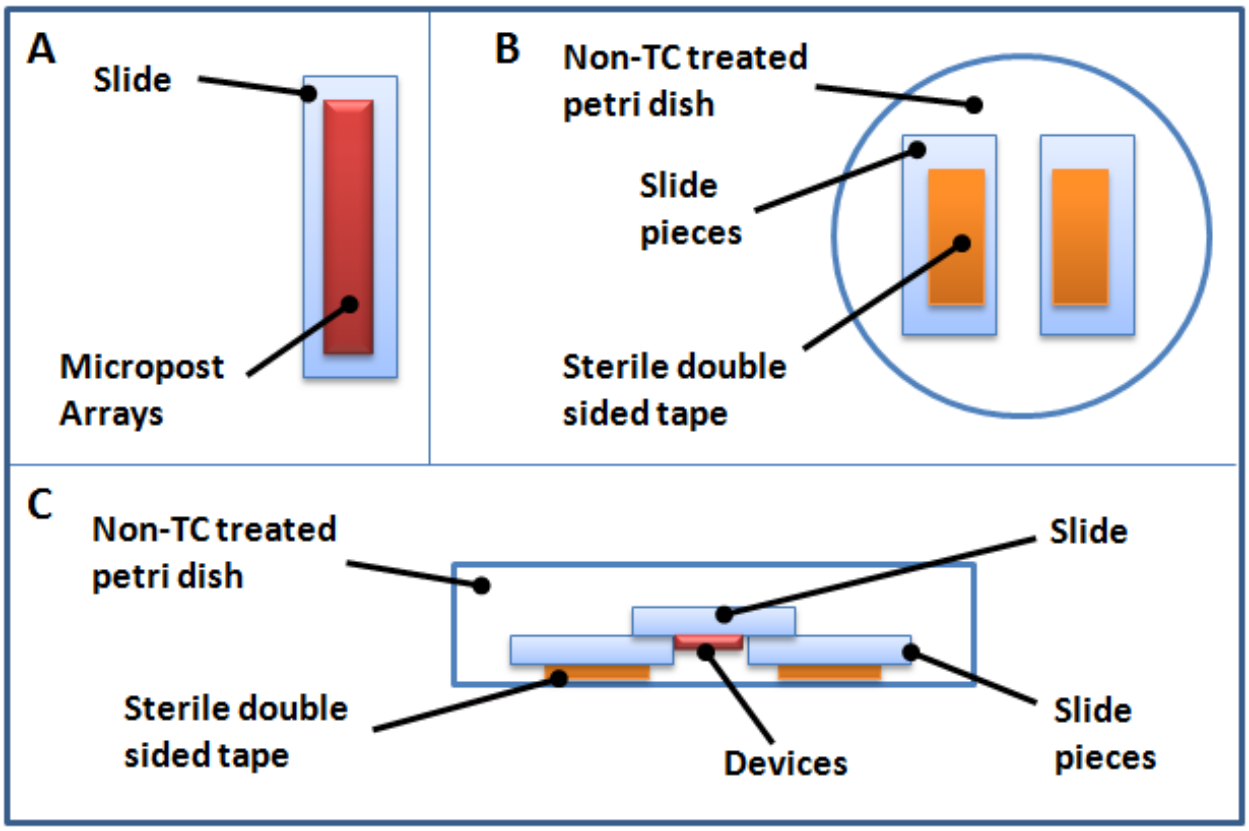

Figure 2.6. Custom fixtures for inverted microscopy.
(*A*) Micropost array substrates were dried and fixed onto sterilized microscope slides. (*B*) To prevent the surfaces from contacting the base of the petri dishes, halved pieces of microscope slides were fixed a device-width apart using sterilized double-sided tape and served as spacers. (*C*) Prior to viewing, the devices were placed face-down between the fixed microscope slide halves.

After preparation, the micropost array substrates were dried and positioned face-up onto autoclaved or ethanol/UV sterilized microscope slides for handling purposes (**Figure 2.6.A**). In a non-tissue culture (TC) treated petri dish (diameter = 10 cm), two halved sterilized microscope slides were fixed in parallel and spaced a substrate-width apart with sterilized double-sided Scotch tape (**Figure 2.6.B**). Non-TC dishes were selected to prevent cells from growing on the

bottom of the dish, which could affect imaging quality. The Scotch tape was sterilized by submerging pieces in 70% ethanol for 15 minutes, washing twice in DI water, and air drying under UV light. This petri dish assembly served as a custom fixture for imaging.

After the cells were seeded and incubated on the substrates for one hour, all DMEM was displaced by CO_2 independent media supplemented with 10% FBS and 1% P/S (*Gibco, Invitrogen, NY, USA*). To observe cellular behavior, the substrates on glass slides were placed into the custom fixture described previously. Prior to placement, the fixed halved glass slides in the petri dish were submerged in CO_2 independent media. The substrates were then slowly placed face-down between the parallel halved glass slides to prevent the trapping of air bubbles between the substrates and the dish bottom. This configuration enabled the substrates to be imaged directly through the media and the dish bottom, while fixing them in place to prevent movement during time-lapse imaging (**Figure 2.6.C**). These substrates were viewed (*Eclipse TE300 inverted microscope, Nikon*) using time-lapse phase contrast microscopy with images taken every 10 minutes for 18-hour periods and analyzed using Simple PCI software (*Compix, Inc.*). Due to the nature of time-lapse microscopy and the biological demands of living cells, the cells required an incubator-like environment during experiments. To address this need, a custom machined chamber was designed and built out of Plexiglass (*Tap Plastics, CA, USA*) to enclose the Nikon microscope. This created a semi-sterile environment for the cells and allowed for temperature (heater set to 38°C) and humidity control of experiments (**Figure 2.7**). Humidity was controlled by placing 700ml of DI water in an open Griffin beaker in the chamber.

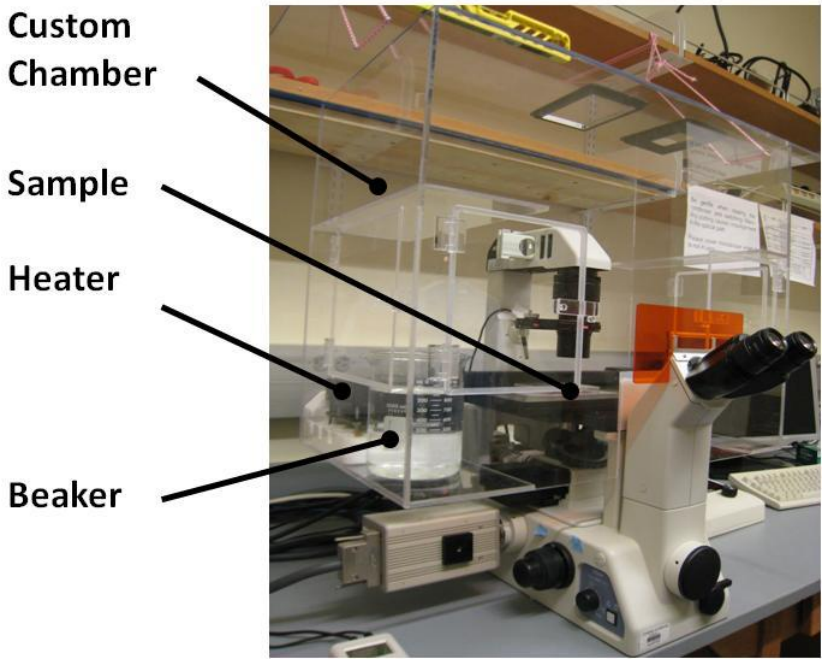

Figure 2.7. Customized chamber for time-lapse microscopy.
A Plexiglas chamber was custom machined for the Eclipse TE300 inverted microscope to create a semi-sterile environment with temperature and humidity control for maintaining cell viability during time-lapse experiments.

Data Acquisition and Analysis

Single cell migration data was collected by analyzing video images through a custom program developed in ImageJ (*National Institutes of Health (NIH), USA*). Considering that factors such as cell-cell interactions and collapsed microposts can possibly affect cell behavior, data was collected for single cells that had no contact with other cells, the edges of the arrays, and remained on pristine parts of the patterns during the entire experiment. Displacement and velocity data was collected by tracking the approximate area centroids of the cells over time. This data is presented as means and standard error of the mean (s.e.m.), which were directly calculated from the data. The s.e.m. is calculated by dividing the standard deviations by the square root of the sample size, n. The p values for samples of data were also calculated as a means to demonstrate statistical significance between two samples if the difference was less than 0.05. These were calculated using unpaired Student's t tests. By dividing the differences between two samples' means with the corresponding standard error of the difference of the two means, t values were calculated. The two-tailed p values were then calculated using these t values and numbers of degrees of freedom equivalent to $n - 2$.

2.4 Results and Discussion

2.4.1 Device Microfabrication

The design of the micropost array gradients was an iterative process. Major considerations included the minimum resolvable micropost dimensions (radii of 1 μm) and largest tolerable spacing (10 μm) that would still prevent cells from falling in between the microposts. Additionally, the greatest failure mode of the micropost array gradients was the irreversible collapse of microposts onto one another, or stiction (**Figure 2.8**), caused by multiple crossings of the liquid-vapor barrier during preparation. Stiction rendered the micropost arrays unusable by compromising the original stiffness and spacing cues of the substrates. Several methods were attempted to minimize stiction in the system, including reducing exposure times and various coatings or surface roughening. The results of these methods can be found in **Figure 2.9**. Although reducing exposure times can lower the aspect ratio of the microposts and change the angle of the micropost sidewalls, underexposure of the microposts yielded features with top surfaces that were textured instead of flat (**Figure 2.9.A-C**). Lowering the surface energy is a common method of reducing stiction at the microscale. To lower the surface energy of the microposts, their surfaces were roughened by O_2 plasma and coated with fluorinated polymers in *ptherm*. However, these methods were not successful in eliminating stiction (**Figure 2.9.D-E**) and redesigning the spacing in the micropost patterns was required to prevent microposts from collapsing onto one another. Experimental results show that for microposts with radii of less than 1.5 μm, the ratio of the micropost topographical area to the corresponding unit cell should not

exceed 0.2. Hexagonal spacing and ratios closer to 0.1 were able to eliminate stiction in the micropost arrays entirely.

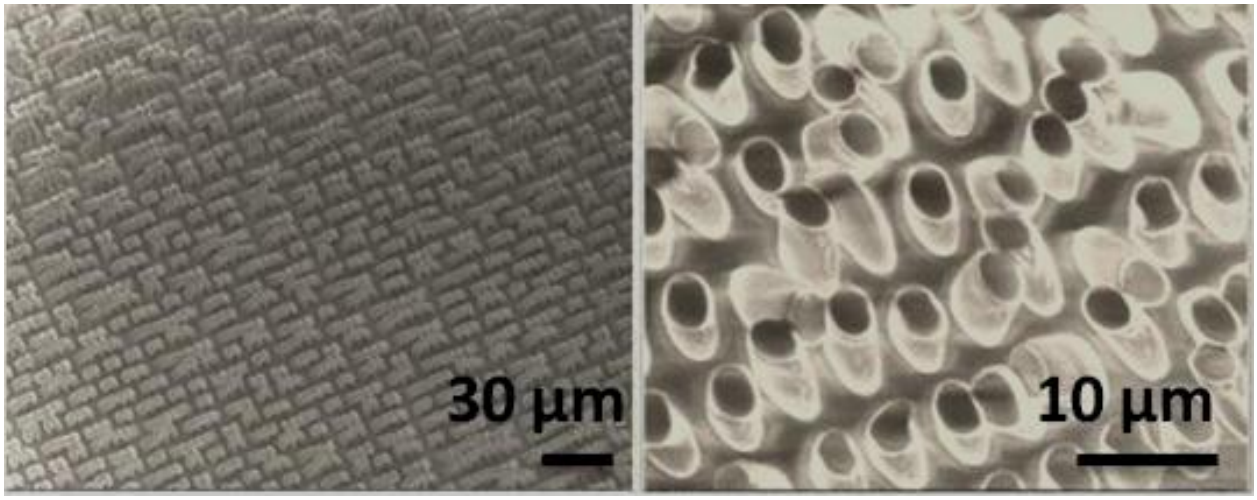

Figure 2.8. Micropost array stiction.
During cleaning, microcontact-printing, and liquid sterilization, the micropost arrays break the liquid-vapor barrier multiple times. This causes the microposts (height = 7 μm) to exhibited significant stiction during drying. (*Left*) At a magnification of 729X, clusters of the collapsed microposts can be seen, some with as many as 12 microposts. (*Right*) At higher magnification (4.24kX), micropost exhibit significant deformation to make contact with other microposts.

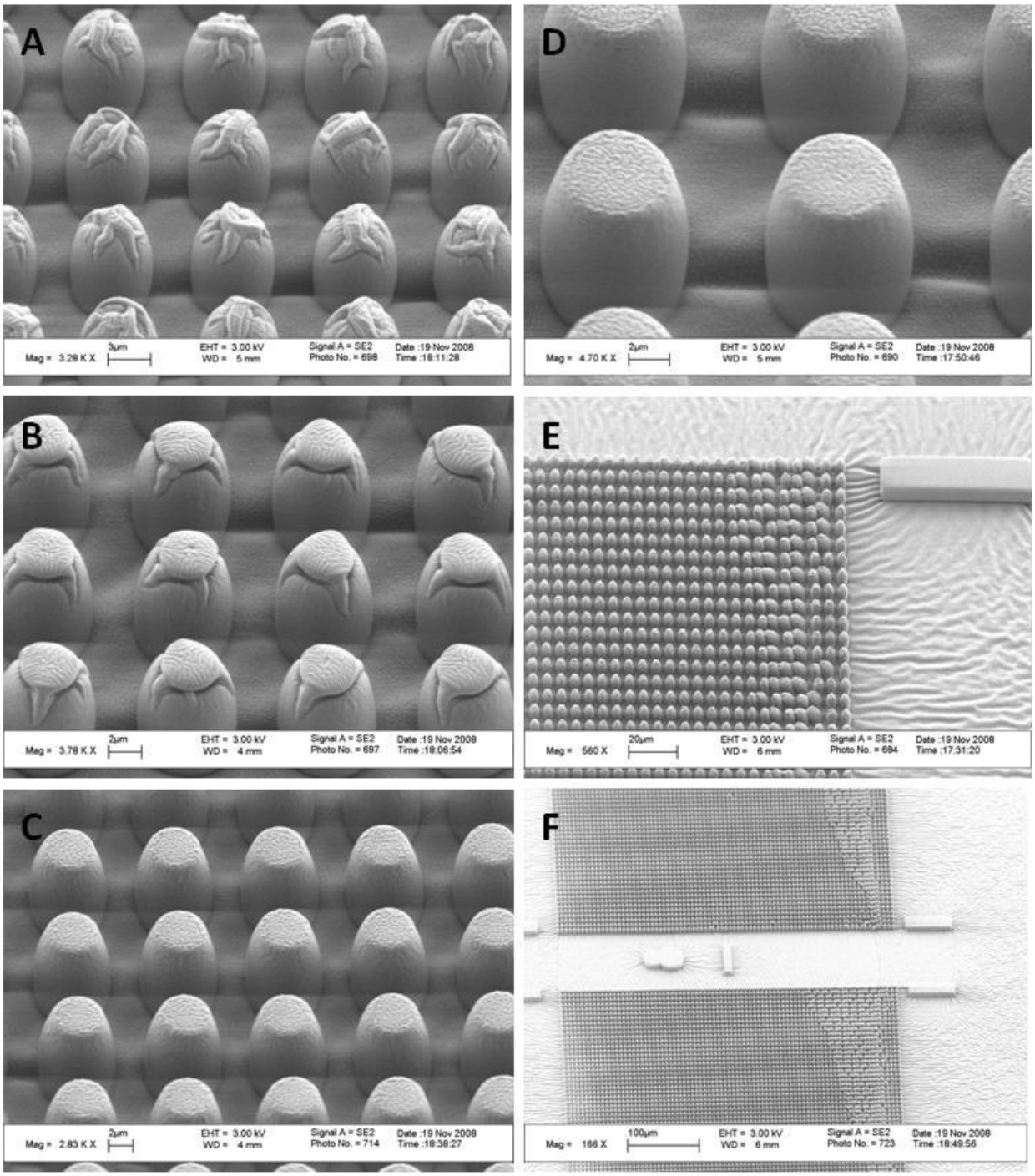

Figure 2.9. Methods for reducing micropost stiction.
Two methods were tested for reducing micropost stiction: (*A*-*C*) vary exposure times, and (*A*-*F*) O_2 plasma etching combined with deposition of a fluorinated polymer (*ptherm*). (*A*-*C*) While increasing exposure time (0.35–0.50 seconds) produces cleaner and taller features, the microposts become more susceptible to stiction due to the increasing aspect ratio. Surface roughening and coating with a fluorinated polymers are common methods of decreasing surface energy, and can been seen in (*D*). However, by examining the arrays with decreasing magnification (*E* to *F*), varying exposure and lowering surface energy did not eliminate stiction entirely.

2.4.2 Single Cell Migration Results: *μDGs*

Experimental results for the *μDGs* indicated that both substrates can preferentially induce BAEC migration in the direction of increasing micropost stiffness (**Figure 2.10, Figure 2.11**). [91]

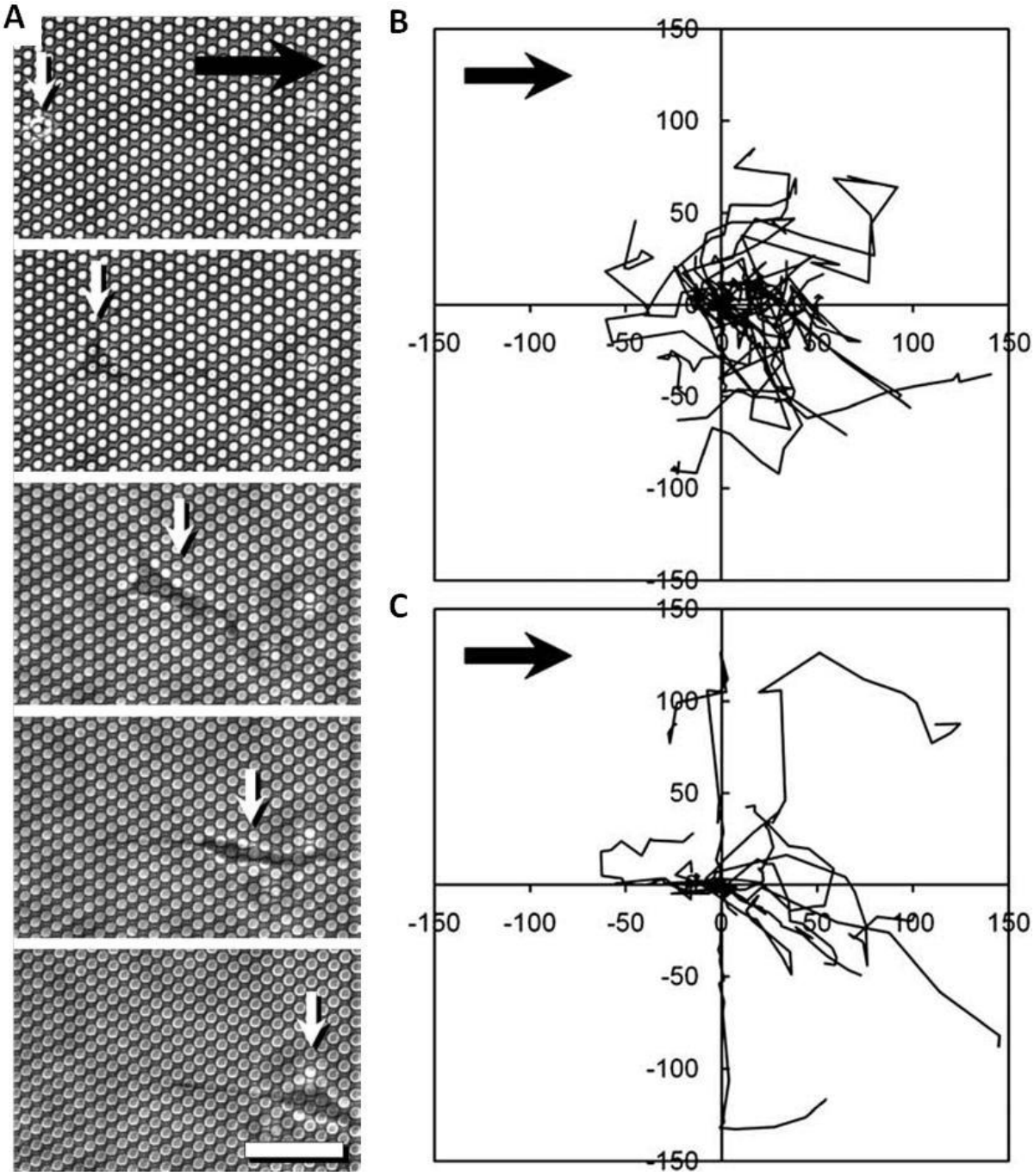

Figure 2.10. BAEC migration on *μDGs*.
(*A*) Time-lapse images of a BAEC migrating on a μDG_L over an 18-hour period where the cell body is located by the white arrows. All black arrows denote the direction of increasing micropost stiffness. Bar

= 50 μm. Normalized 2-D migration paths are shown for (*B*) 23 cells on a μDG_L and (*C*) 13 cells on a μDG_H, illustrating a bias towards the direction of increasing stiffness. Axes are in units of microns.

To quantify migratory behavior, the displacement of BAECs was tracked on both substrates for 18-hour periods. Time-lapse images of this migration can be found in **Figure 2.10.A**, where movement is shown every 4.5 hours. These images show cell migration in the direction of increasing micropost stiffness (rightward direction). On the μDG_L substrates, the average displacement of 23 BAECs along the axis (x-direction) of changing micropost stiffness was found to be 26.5 ± 8.7 μm, where positive and negative displacement values correspond to the directions of increasing and decreasing micropost stiffness, respectively. The maximum positive displacement for these cells was 141 μm, and the maximum negative displacement was 45 μm. After 18 hours, 16 out of the 23 BAECs, or 70%, had a net displacement in the direction of increasing micropost stiffness. The 2-D migration paths for these BAECs can be found in **Figure 2.10.B**. These paths, which are normalized to the original starting positions of the cells, illustrate the bias of movement in the positive x-direction, and also show significant displacement lateral (y-direction) to the axis of increasing micropost stiffness. The quantification of these displacements can be found in **Figure 2.11.A**. The average x- and y-displacements refer to the average displacements of cells relative to their starting positions, where positive x-displacement is in the direction of increasing stiffness. The average net displacement is the summation of all movement in the x- and y-directions over time.

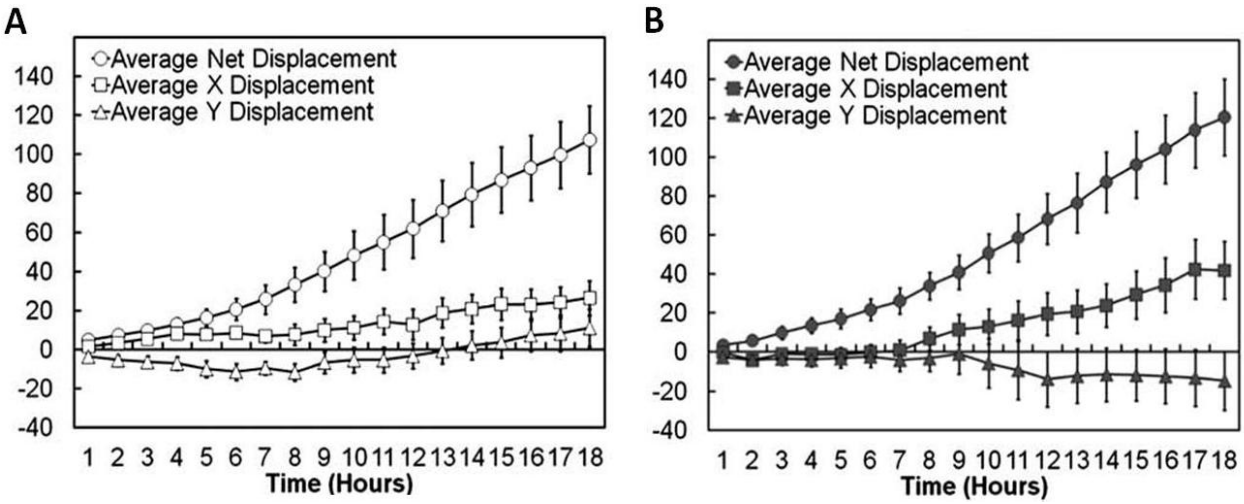

Figure 2.11. Experimental displacement data for *μDGs*.
Average cell displacements for (*A*) μDG_L and (*B*) μDG_H over 18-hour periods. X- and y-displacement refer to the axes parallel and perpendicular to the durotaxis gradients, respectively. Positive x-displacement values indicate movement in the direction of increasing stiffness, and negative displacement values are in the direction of decreasing stiffness. The average net displacement refers to the summation of the all movement in the x- and y-directions integrated over time. Results suggest that higher gradient strengths enhance the magnitude of displacements in the direction of increasing stiffness. Both graphs indicate that there is significant movement in the y-directions. Y-axis values are in units of microns. Error bars = s.e.m.

On the μDG_H substrates, the magnitude of positive cellular displacements and the percentage of cells moving in the direction of increasing stiffness were increased. This enhancement of the durotactic response with increased gradient strength is consistent with previous work. [48], [54], [89] The average displacement in the direction of increasing stiffness of 13 BAECs on the μDG_H was found to be 41.9 ± 14.7 μm, with a maximum positive displacement of 145 μm, and maximum negative displacement of 24 μm. This negative displacement has also been reduced relative to the μDG_L. At the end of the 18-hour studies, 10 out of the 13 cells, or 77%, had a net displacement in the direction of increasing stiffness. The 2-D migration paths of these cells over 18-hour periods can be found in **Figure 2.10.C**, and were quantified similarly to the μDG_L in **Figure 2.11.B**. For both *μDGs*, there exists a bias of displacement in the positive x-direction, with a stronger bias on the higher gradient strength. Similar trends do not appear to be present in the y-direction, having smaller average displacements relative to the positive x-direction. There is, however, a slight favoring of the negative y-direction for cells migrating on the μDG_H, which is possibly due to the random walk behavior of cells.

In addition to displacement, cellular migration velocity was also affected by the *μDGs*, as summarized in **Figure 2.12**. During the 18-hour periods, cells moved faster on the μDG_L (white) than the μDG_H (gray), with average speeds of 7.5 ± 0.5 μm/hr and 7.0 ± 0.7 μm/hr in the positive x-direction, respectively. While there was slight difference in magnitude, this was not statistically significant ($p = 0.61$). In the negative x-direction, BAECs on the μDG_L traveled at a reduced speed of 6.6 ± 0.5 μm/hr, which was not statistically different ($p = 0.24$) from their speed in the positive x-direction. On the μDG_H, the BAEC migration speed in the negative x-direction also decreased, with a magnitude of 4.8 ± 0.6 μm/hr. This change in migration speed was statistically different from the movement in the positive x-direction on the μDG_H, as well as in the negative x-direction on the μDG_L, with $p < 0.05$ in both cases. Thus, BAECs migrating on the μDG_H moved at speeds 46% faster in the direction of increasing stiffness versus the direction opposite to that.

Aspects of cellular migration, displacement and velocity, on the *μDGs* were enhanced by increasing the strength of the stiffness gradients. In comparison to the μDG_L, BAECs migrating on the μDG_H displaced farther, on average and maximally, in the direction of increasing micropost stiffness. BAECs also traveled shorter distances in the direction of decreasing stiffness. A larger percentage of migrating cells responded desirably to the *μDGs* higher gradient strength, displacing in the direction of increasing stiffness. Additionally, while the cell migration speeds on both substrates in the direction of increasing micropost stiffness were comparable, BAECs on the μDG_H moved at statistically slower speeds in the opposite direction. BAECs on the μDG_L, in contrast, did not move statistically slower.

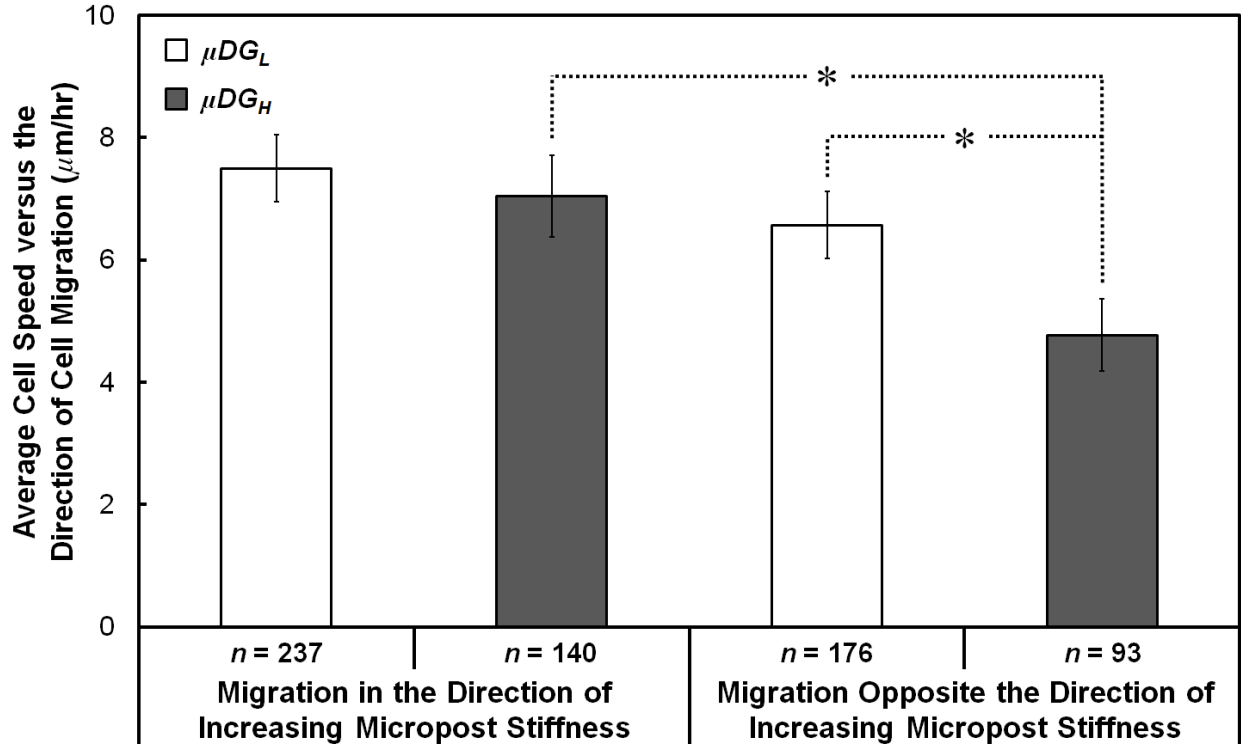

Figure 2.12. Experimental velocity data for *μDGs*.
The velocity of BAEC migration was calculated for all cells used to determine displacement data on the μDG_H and μDG_L. Velocity of each cell was calculated over 1-hour intervals (n = number of time steps) during the 18-hour experiments. In the direction of increasing micropost stiffness, BAECs migrated at comparable speeds on the μDG_L (white) and the μDG_H (gray). Although migration speeds on μDG_L were slightly slower in the direction of decreasing stiffness, this was not statistically significant. In contrast, the migration speed in the direction of decreasing stiffness on the μDG_H was found to be statistically different from movement in the opposite direction, as well as from the movement in the direction decreasing stiffness on the μDG_L. * denotes statistical significance with $p < 0.05$. Error bars = s.e.m.

While the *μDGs* were designed to a constant "effective" topographic surface area for regimes of different stiffnesses and yielded durotactic results consistent with previous research, factors such as changes in micropost-specific topographical surface area could have affected the migration results. At this time, effects of increasing the unique micropost topographical surface area are unknown and might affect cellular migration by varying the amount of continuous area available for cell-substrate attachments. This speaks to questions regarding how the density, size, and numbers (per micropost) of focal adhesion could influence the migration process

2.4.3 Single Cell Migration Results: *μDSGs*

Experimental results demonstrated that variable spatial cues can affect migratory behaviors of BAECs. [92] In direct comparison with the micropost stiffness regimes of the μDG_L, BAECs migrating on the *μDSGs* indicated that increasing interpost spacing can negate the cellular response to durotactic migratory cues. A comparison of the displacement data

demonstrates this to be a statistically significant difference, with a $p < 0.05$. Migration of BAECs on the *μDSGs*, displayed through time-lapse images taken every 3-4 hours over an 18-hour period, can be found in **Figure 2.13.A**. These images show a unidirectional migration in the direction of decreasing interpost spacing (rightward direction), which runs opposite the direction of increasing micropost stiffnesses (leftward direction). The 2-D normalized migratory paths for these cells can be found in **Figure 2.13.B**, which are further quantified as absolute movement in the directions of decreasing interpost spacing (positive x-direction) and perpendicular to the gradient (y-direction) in **Figure 2.13.C**. In **Figure 2.14**, average directional displacements are quantified, where positive x-direction refers to movement in the direction of decreasing interpost spacing (decreasing micropost stiffness), and negative values are in the direction of increasing interpost spacing (increasing micropost stiffness). The average displacement of 38 BAECs in the positive x-direction was 9.6 ± 7.3 μm, with a maximum positive displacement of 149 μm and a maximum negative displacement of 115 μm (**Figure 2.14.A**). While displacement along the x-axis shows bias as expected, movement in the y-direction appears to oscillate near zero, with average absolute displacement of 4.2 ± 11.5 μm. Of the 38 BAECs tracked on the *μDSGs*, 23, or 61%, displaced in the direction of decreasing interpost spacing.

Additionally, interpost spacing affected the speed of migration on these surfaces. During 18-hour studies, the average BAEC migration speed was 5.42 ± 0.36 μm/hr in the direction of decreasing interpost spacing, and 4.67 ± 0.31 μm/hr in the opposite direction. Although there is a slight difference in the two directions, this was not found to be statistically significant ($p = 0.12$).

While the exact mechanisms of cellular migration are not well understood, explanations for this behavior can possibly be attributed to the different stages of cell motility. Protrusive activity of cells is a stochastic process, and the formation of a dominant lamellipodia that determines the directionality of migration relies on cells being able to reach a subsequent attachment point and form cell-substrate junctions. Although the durotactic cues increase on the μDG_L over the course of the array, the interpost spacing also increases in parallel on the *μDSGs*, which places stiffer microposts increasingly farther and farther away. This increased interpost spacing likely lowers the probability of cells being able to reach them during the stochastic protrusive activity, precluding them from physically reaching these attachment points. Large spacing, therefore, limits what durotactic information cells can receive from their microenvironments, leading to a dominance of spatial cues over stiffness cues in these micropost array gradients. This increasing spacing likely contributes to the lower average migration speeds of the cells in comparison to the *μDGs*. The *μDSGs* also have the same micropost-specific topographical surface area issues that the *μDGs* have. The gradient in micropost-specific topographical surface area could potentially result in localized chemical gradients, since the surfaces are microcontact-printed with fibronectin. These chemotactic cues could theoretically work in concert with the durotactic cues, suggesting that spatial cues are an even stronger regulator of cellular migration.

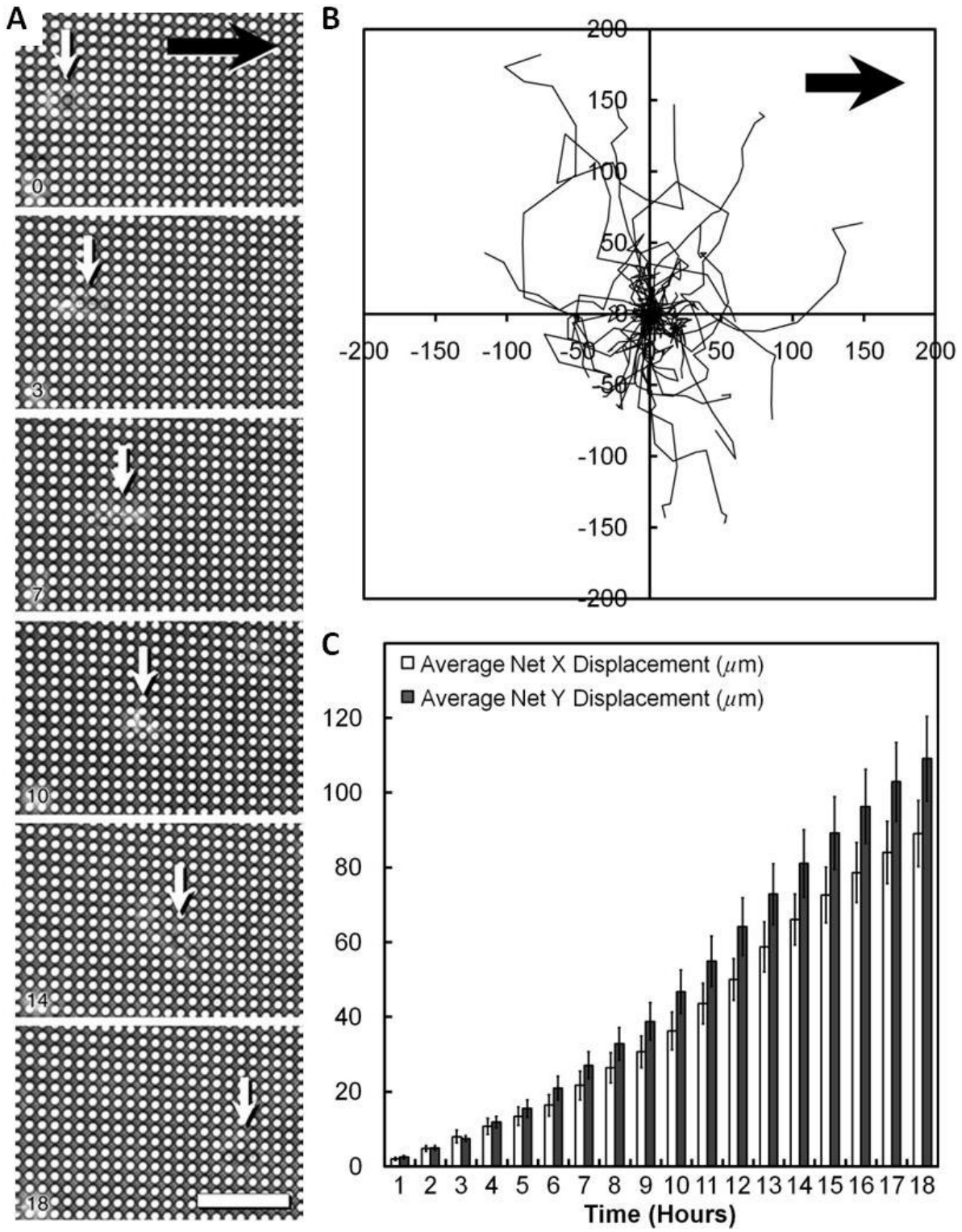

Figure 2.13. BAEC migration on *μDSGs*.
(*A*) Time-lapse images of a BAEC migrating on a *μDSG* over an 18-hour period where the cell body is located by the white arrows. All black arrows denote the direction of decreasing interpost spacing (decreasing micropost stiffness). Numbers indicate time stamps in hours. Bar = 50 μm. (*B*) Normalized 2-D migration paths are shown for 38 BAECs. Axes are in units of microns. (*C*) Average absolute displacement of cells in the x- and y-directions during 18-hour studies. Error bars = s.e.m.

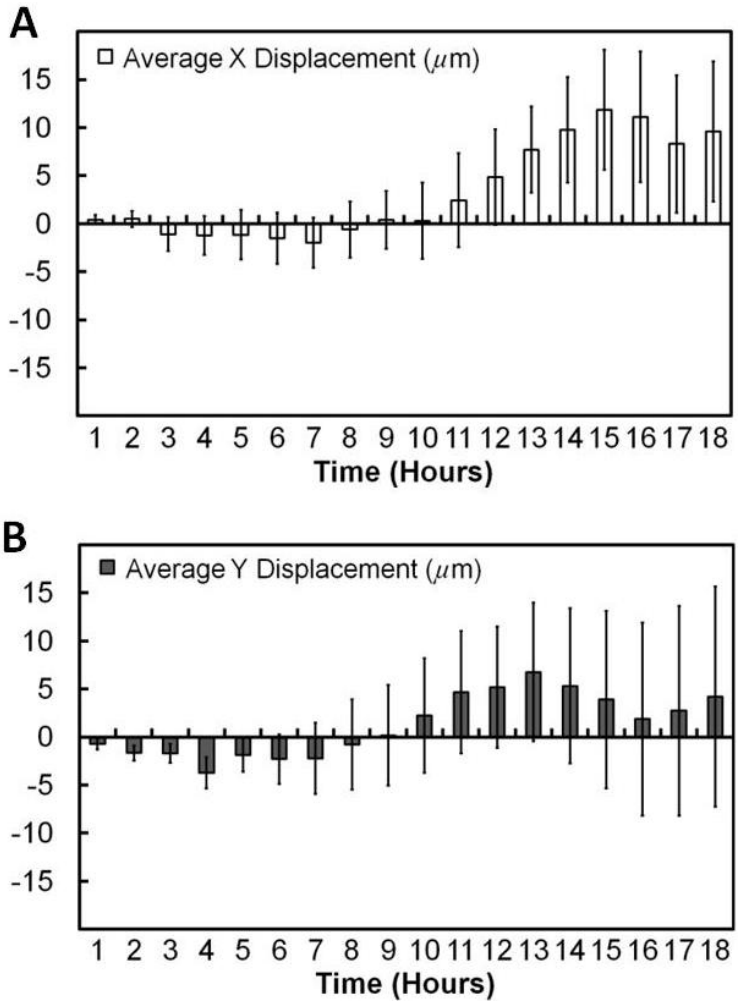

Figure 2.14. Experimental displacement data for *μDSGs*.
Average displacement of 38 BAECs over 18-hour periods on the *μDSGs* (*A*) parallel (x-direction) and (*B*) perpendicular (y-direction) along the axis of varying interpost spacing and micropost stiffness. Positive and negative values of displacement in the x-direction indicate movement in the direction of decreasing and increasing interpost spacing, respectively. From (*A*), there is a bias of movement in the direction of decreasing interpost spacing – opposite of the results for the *μDGs*. As there are no unidirectional stiffness changes perpendicular to the x-direction, (*B*) shows unbiased migratory behavior in the y-direction. Error bars = s.e.m.

Chapter 3: Micropost Arrays for Regulation of Collective Cell Behavior

3.1 Introduction

This chapter describes using uniform and gradient micropost arrays in interpost spacing to modulate the biophysical microenvironment for collective cells, as well as a test methodology for direct culture of cell collectives onto these surfaces. Micropost arrays of varying radii and heights are employed to mechanically study collective cell behavior.

Collective Cells versus Single Cells

While single cell behavior provides an important foundation for predicting effects of biophysical cues, few cells in the body operate individually. Instead, group, or collective, cell behavior is the true environment behind many biological processes, such as immune response, tissue formation, and organ regeneration. [93–95] Transitional behavior from collective-to-single cell states, and vice versa, also characterizes many growth and pathological biological phenomena, including wound repair and cancer metastases. [8], [96] However, since collective cell studies are significantly more complex than single cell studies, the field of collective cell biology remains relatively unexplored. [97]

In comparison to single cell behavior, collective cell behavior involves higher communication complexity as cells must work in concert with one another. Like single cells, collective cells respond to chemical regulation and can form cell-substrate junctions to mechanically transduce information from their environments. However, when cells are in a collective state, they initiate other communication methods to enable them to work synergistically. This "quorum" behavior materializes through new physical and chemical connections. Physically, collective cells can form cell-cell connections, such as anchoring (adherens, desmosomes), occluding (tight), and communicating (gap) junctions (**Figure 3.1**), which allow direct communication of small molecules or electrical signals through cytoplasmic connections with neighboring cells. [1], [2], [98] These junctions also enable tissue-level functionalities, which can include creating physical barriers between the interior and exterior of vessels, [98] exertion of greater traction forces, [82], [99–101] and collective cell migration. [95], [102] New paths of chemical signaling also occur, known as paracrine or juxacrine signaling, through the secretion and diffusion of factors from one cell to another. This type of collective cell chemical signaling is used *in vivo* to regulate group behaviors such as maintenance of vascular tone, angiogenesis, and proliferation. [21], [98], [103], [104]

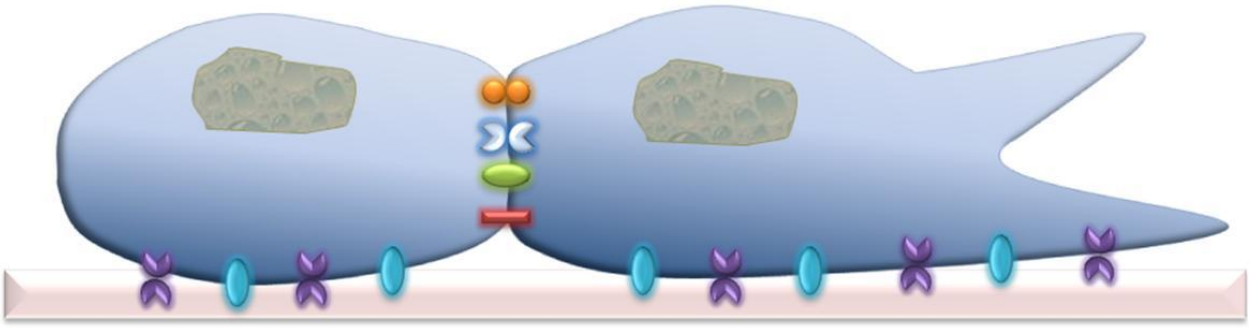

Junction Type	Cell-Substrate	Cell-Cell
Anchoring	Focal Adhesions Hemidesmosomes	Adherens Desmosomes
Occluding		Tight
Communicating		Gap

Figure 3.1. Cell-substrate and cell-cell junctions of collective cells.
Collective cells can form physical junctions with their surroundings, like single cells, as well as with one another. Cell-substrate junctions, such as focal adhesions and hemidesmosomes, are primarily for anchoring and for obtaining mechanotransductive information for the cellular microenvironment. Cells are also physically able to localize with one another through adherens junctions and desmosomes, and are capable of forming gap junctions that enable direct cytoplasmic connections for communicating with electrical impulses or small molecules. Occluding junctions, such as tight junctions, enable collective cells to have tissue functionalities, such as being able to create barriers between the external surfaces of intestinal tracts and their lumen.

Microenvironmental Cues and Collective Cell Behavior

While prior research on collective cells has primarily focused on their biology and the internal mechanisms that are involved in maintaining their collective states, [74], [105] microenvironmental cues have been shown to influence their behavior. Collective cell migration [95], [106–109] and patterning of groups of cells can be induced using soluble or substrate-immobilized chemical cues. [100] Active and passive biophysical cues can possibly affect group behavior as well. When exposed to shear stress from fluid flow, monolayers of cells can exhibit morphological changes and collective migration. [110] Scratch wound assays, where parts of cell monolayers are removed to create openings in the layer, have been utilized to induce collective cell migration as part of the wound healing response. [111], [112] Researches have employed polyacrylamide gels to change the stiffness of a substrate. Over the course of a few hours, loosely clustered groups of cells either exhibited dispersion into single cells or formed tissue-like constructs on stiff and soft gels, respectively (**Figure 3.2.A-B**). This phenomenon was also described for tissue explants, where migration of cells from the tissue was found to be limited by

softer substrates, even after three days of culture. On stiff surfaces, cell migrated away from the tissue explants, marking the breakdown of tissue behavior. (**Figure 3.2.C-D**). [55]

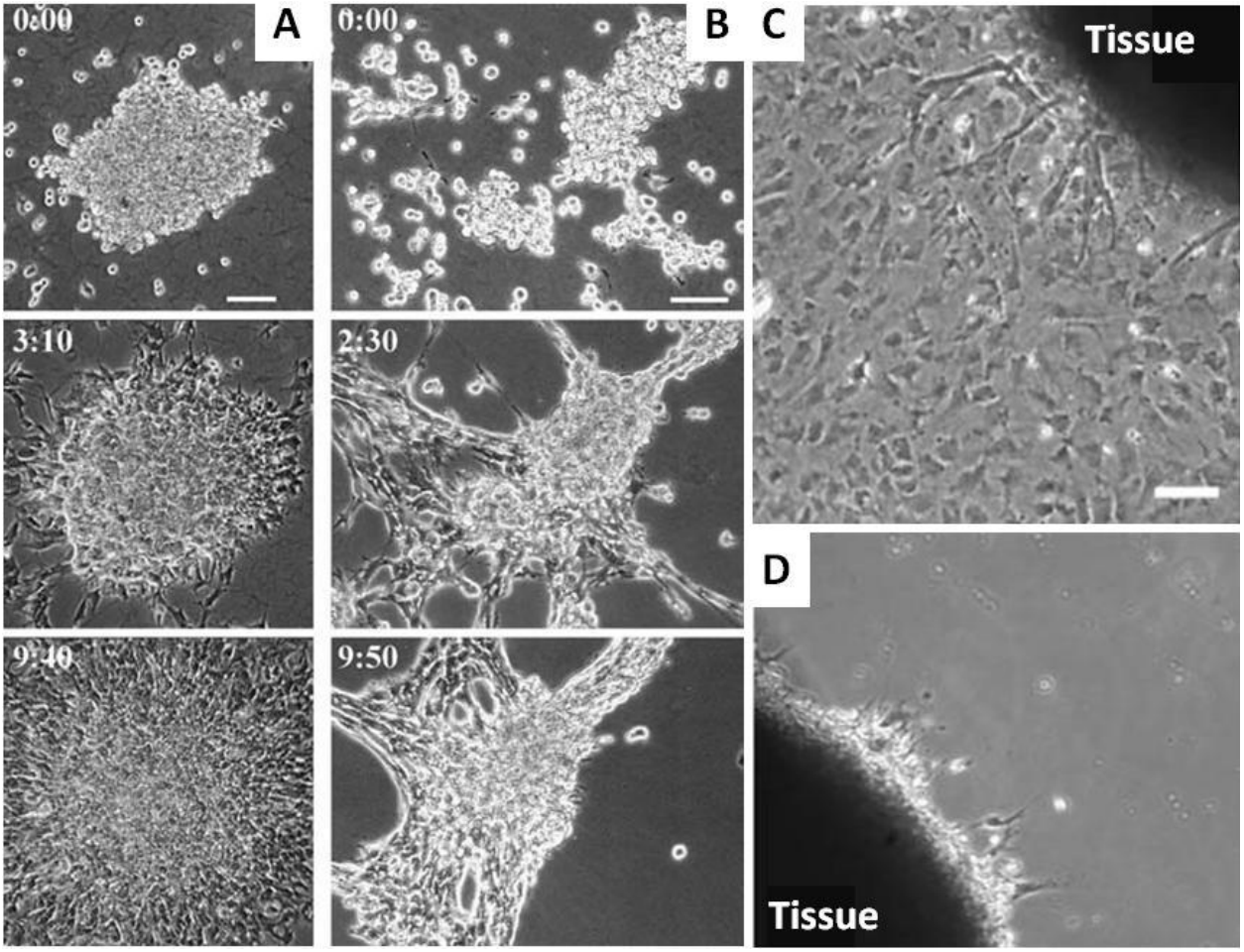

Figure 3.2. Maintenance and inhibition of tissue behavior on polyacrylamide gels.
Researchers placed loosely clustered groups of fibroblasts onto (*A*) stiff (7.69 ± 2.85 kPa) and (*B*) soft polyacrylamide gel surfaces (2.68 ± 0.99 kPa). Cells on the stiff surfaces migrated away from the clusters as single cells. In contrast, on the soft surfaces, cells formed tissue-like constructs. Time stamps are in hh:mm. This was also shown for tissue explants placed on (*C*) stiff and (*D*) soft surfaces. After 3 days in culture, single cells migrated away from the tissue explants on the stiff surfaces, but barely on the soft surfaces. Bars = 100 μm [113]

As collective cell behavior relies on the existence of cell-cell junctions, these results suggest that the biophysical force balance that hypothetically exists between cell-cell and cell-substrate junctions can be manipulated through substrate stiffness, as shown in **Figure 3.3**. [107], [114], [115] Substrate stiffness, which can influence cell-substrate junctions, [116] might play an integral role in inducing or controlling biological phenomenon that rely on collective behavior and collective-to-single cell transitions by causing these junctions to be stronger or weaker than the adhesion forces of cell-cell junctions. For example, if cell-cell junctions are much stronger than cell adhesion forces to a soft substrate, then collective cell behavior might be maintained.

Conversely, if the cell-cell junctions are much weaker than cell-substrate junctions on a stiff substrate, single cell behavior may be favored. As the micropost array substrates mentioned previously in **Chapter 2** were able to influence single cell behavior, they can be utilized to study collective and transitional cell behavior.

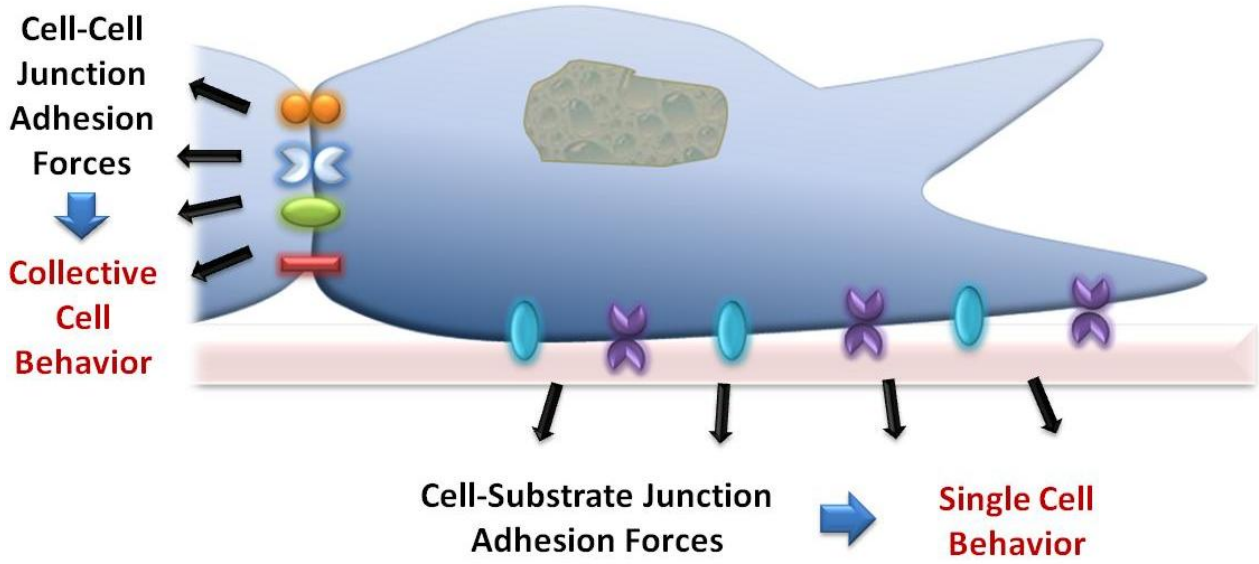

Figure 3.3. Biophysical force balance between cell-cell and cell-substrate junctions.
A biophysical force balance between the adhesion forces of cell-cell junctions and cell-substrate junctions may play a significant role in maintaining single and collective cell states. It is hypothesized that tissue behavior is preserved when cell-cell junctions dominate the physical interactions cells have with their environment. Conversely, if cells are able to form more favorable junctions with their substrate, collective cells may break apart and result in single cell behavior.

Microtopographic substrate-based biophysical stimuli, which are well-controlled and simply fabricated, have been used to study specific aspects of collective cell behavior, including traction forces, directed migration, and alignment. For gels with semi-aligned collagen fibers, cells within a collective have shown various levels of polarization. [117] Using microtopographic surfaces, researches have shown that the collective cell leading edge may extend along microridges, [64] and exert larger traction forces than single cells. [100], [101], [118] Additionally, cell collectives were able to be confined by patterns of holes in their substrates. [69] While these findings suggest microtopographic surfaces can be used to mechanically influence collective cell behavior, they have not been utilized to investigate effects of substrate stiffness on collective cell behavior or collective-to-single cell transitions.

By utilizing uniform and gradient micropost arrays to change the apparent stiffness of the cellular substrate, the effectiveness of using microtopography to study stiffness-related collective behavior and collective-to-single cell transitions will be explored. Similar to the aforementioned maintenance and inhibition of collective cell behavior on polyacrylamide gels, it would be expected that cells will break away from a collective and observe single cell migration on stiff

micropost (short or large radii) arrays, and maintain their collective behavior on soft (tall or small radii) micropost arrays. A schematic of this project concept can be found in **Figure 3.4**.

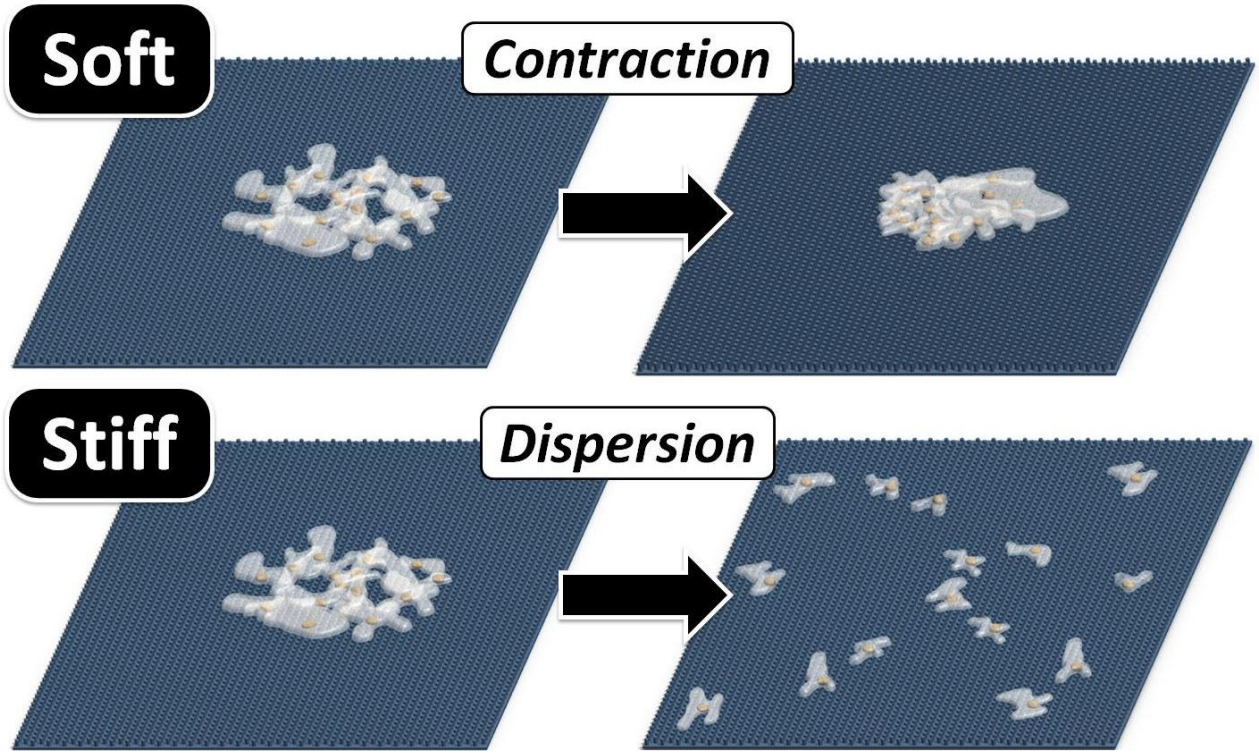

Figure 3.4. Project concept: collective cell behavior.
Previously, substrate stiffness has been shown to maintain collective behavior or induce transitions to single cell behavior. As micropost arrays are capable of regulating the apparent stiffness of a substrate at the microscale and have demonstrated influence over single cell behavior, these microtopographic surfaces are potentially capable of either maintaining or inhibiting collective cell behavior as well. On soft micropost (tall or small radii) arrays, cell collectives are expected to maintain their group behavior by allowing cell-cell junctions to dominate. Alternatively, on the hard micropost (short or large radii) arrays, cell collectives are predicted to breakdown and disperse into single cells, favoring stronger cell-substrate adhesion forces.

3.2 Design of Micropost Arrays and Thin-film Stencils

To explore the potential of using micropost arrays for controlling collective cell behavior, and possibly for observing transitions between collective and single cell states, uniform micropost arrays were designed in addition to gradient arrays.

3.2.1 Uniform Micropost Arrays: *μVRs* and *μVHs*

Two groups of uniform circular micropost arrays were designed: (*i*) microtopographic constant micropost height, variable micropost radius array (*μVR*), and (*ii*) microtopographic

constant micropost radius, variable height array (*μVH*). The *μVR* and *μVH* (**Figure 3.5**) were designed to create surfaces of uniform apparent stiffness through various micropost geometries. To maintain consistency with the micropost array gradients used for the single cell studies, the same ratio of micropost top surface area to corresponding unit cell was used – *%ECM* of 0.2. For all uniform arrays, the interpost spacing was uniform in both the x- and y-directions to eliminate any gradients and the microposts were arrayed using hexagonal spacing. For the *μVR*, microposts had a constant height of 7 μm, and were arrayed uniformly with radii ranging from 1.5-2.25 μm with theoretical stiffnesses of 23.6-106.4 nN/μm (**Figure 3.5.A**). In this way, arrays with different apparent stiffnesses could be fabricated on the same device and tested in parallel with identical environmental conditions. In contrast, the *μVHs* were developed to maintain constant micropost-specific topographical surface area and interpost spacing while changing the apparent substrate stiffness through different micropost heights. For these arrays, the microposts had a constant radius of 1.5 μm and heights varying from 5-6 μm with theoretical stiffnesses of 59.1-36.1 nN/μm (**Figure 3.5.B**). These micropost arrays could be compared directly to the *μVR* with 1.5 μm radii. Due to their variable height, these arrays could not be fabricated on the same device. Arrays ranged in area from 500 x 500 μm^2 to 2500 x 2000 μm^2.

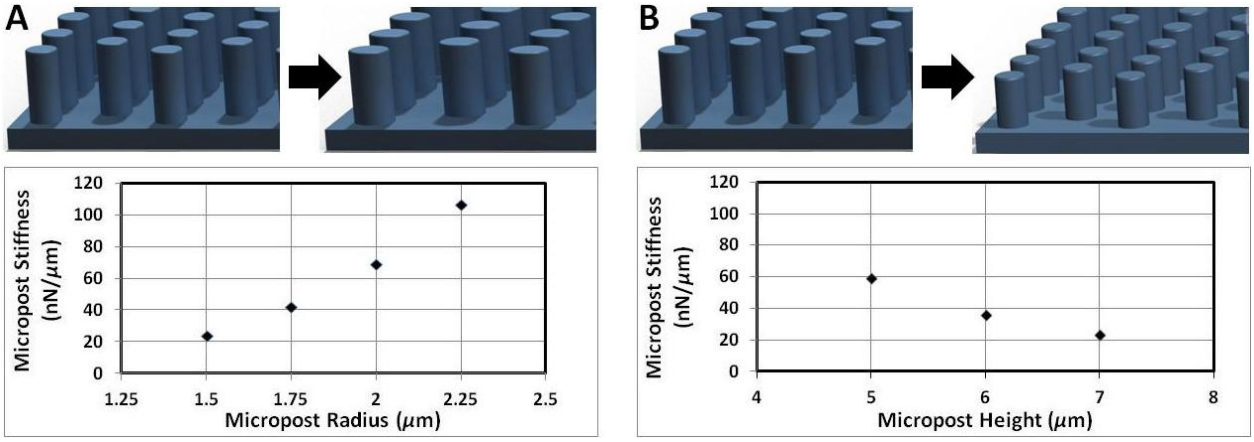

Figure 3.5. Concept schematic for the *μVRs* and *μVHs*.
(*A*) For the *μVRs*, the height of the microposts for all arrays was maintained at 7 μm, while the radius was varied between 1.5-2.25 μm. This enabled uniform arrays of different apparent stiffnesses to be tested in parallel on the same device. Theoretical micropost stiffnesses were calculated for these radii in the graph. (*B*) In contrast, the *μVHs* had a constant radius of 1.5 μm for all arrays and variable height ranging from 5-6 μm. These can be directly compared to the *μVR* with radii of 1.5 μm. These arrays enabled the micropost-specific top surface area to be consistent between arrays; however, because they had variable heights, these arrays could not be fabricated on the same device for parallel testing. The graph below includes their theoretical micropost stiffnesses with the *μVR* with radii of 1.5 μm as a reference. From the micropost stiffness graphs, some of the *μVRs* show comparable stiffnesses to the *μVHs*.

3.2.2 Microtopographic Spacing Gradients (*μSGs)*

The single cell migration studies indicated that spatial cues can affect aspects of cellular migratory behavior. To determine if spacing might have an effect on collective cell behavior,

microtopographic spacing gradients, or *μSGs*, were designed (**Figure 3.6**). The *μSGs* consisted of microposts of uniform geometry with interpost spacing that decreased over the length of the array. The microposts had constant heights and radii of 7 μm and 1.5 μm, respectively. The interpost spacing decreased from approximately 3.9-3 μm (**Figure 3.6.B**), or an average of 10 nm post-to-post. This entire interpost spacing range is 2-3 times greater than the interpost spacing for any of the uniform 1.5 μm radii micropost arrays used for the collective cell experiments. Similar to the gradients used for the single cell studies, the interpost spacing was governed by **Equation 2.1**, with a *%ECM* equal to 0.15. As the interpost spacing decreases over the length of the array, the interpost spacing perpendicular to the gradient axis was increased to maintain the ratio. A schematic of the top view of the *μSG* can be found in **Figure 3.6.C**. The approximate area of these arrays was 550 x 550 μm^2.

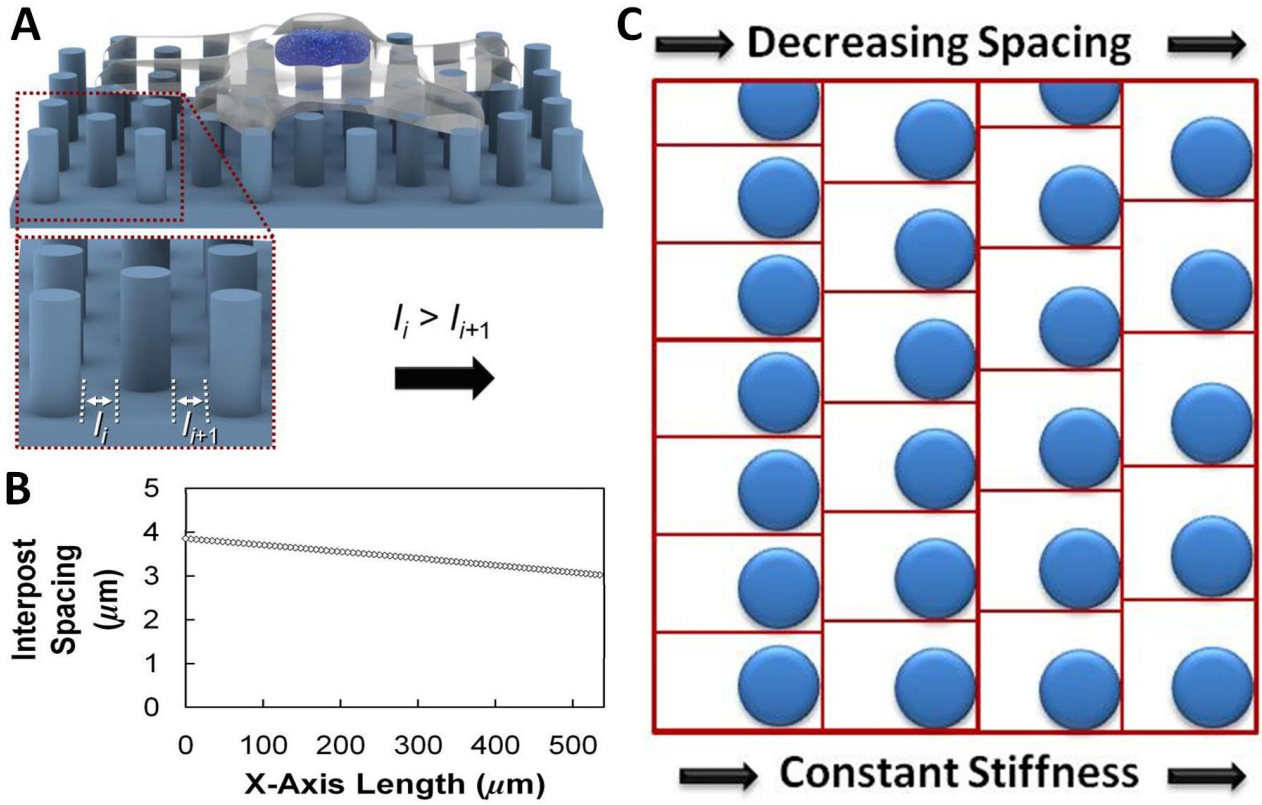

Figure 3.6. Concept schematic for the microtopographic spacing gradient (*μSG*).
To determine if spacing could affect these studies, (*A*) *μSG* with uniform microposts (7 μm tall, 1.5 μm radii) and increasing spacing were designed. The range of interpost spacing (*B*) used in these gradient surfaces was greater than the interpost spacing for any of the *μVRs*. To eliminate effects of increasing topographical surface area, the ratio of the micropost surface area to corresponding unit cells was decreased to 0.15 from 0.2 used for all other micropost arrays. As the interpost spacing increased, the spacing perpendicular to the gradient was decreased. (*C*) A schematic of the top view of the *μSG*, with decreasing interpost spacing and constant micropost stiffness.

3.2.3 Collective Cell Stenciling

From the single cell migration experiments, it became clear that creating uniform groups, or collectives, of cells was very difficult and could not be localized onto the micropost array surfaces in a repeatable fashion. To address this limitation, a method of stenciling cells onto the micropost arrays was developed (**Figure 3.7**). Thin-film stencils, which have historically been utilized for creating openings in cell monolayers for wound healing assays [111], were used to pattern cells on the micropost array surfaces in a manner similar to the metal lift-off processes of microfabrication. The thin-film stencils were designed with 100 μm deep circular or elliptical thru-holes ranging from 50-400 μm in diameter or major axis length. By placing these stencils in close contact with the micropost array surfaces, only select areas of the micropost arrays would be accessible to the seeded cells. The cells could then form collectives within the thru-holes and be released by removing the thin-film stencils.

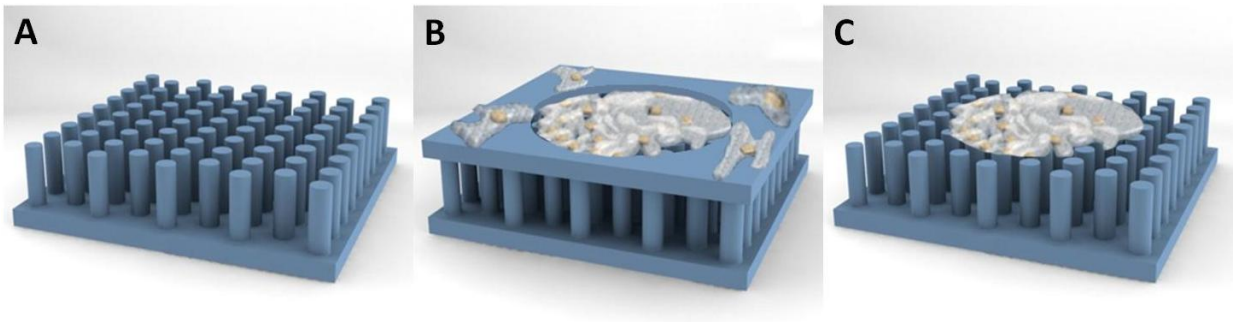

Figure 3.7. Thin-film stencil methodology.
In order to directly localize and grow cell collectives on the micropost array surfaces (*A*), thin-film stencils with circular or elliptical thru-holes ranging from 50-400 μm in diameter or major axis length, were utilized. The thru-holes were 100 μm deep. These stencils were placed in contact (*B*) with the micropost surfaces, allowing only specific areas to be accessible by cells. (*C*) After incubation for a few days, the stencils were removed to release cell collectives.

3.3 Materials and Methods

3.3.1 Micropost Arrays and Thin-film Stencils: Microfabrication and Preparation

Micropost Arrays Substrate Fabrication and Preparation

The uniform and gradient micropost array substrates were fabricated and prepared using the same techniques used for the micropost array gradients and single cell studies. Features of heights ranging from 5-7 μm were targeted for these devices.

Thin-film Stencil Fabrication

Thin-film stencils were fabricated using a one-mask soft lithography process.

Micromold Fabrication

To create micromolds for the stencils, clean silicon wafers were spin-coated (*CEE 100X, Brewer Science, MO, USA*) with SU-8 2050 (*MicroChem Corp., MA, USA*). To yield 100 μm tall features, SU-8 was spun on at 500 RPM for 10 seconds and 1800 RPM for 30 seconds. The wafers were then soft baked on hot plates at 65°C for 5 minutes, followed by 95°C for 20 minutes before exposing in contact mode for 60 seconds (*Hybraline Series 400 Aligner, OAI, CA, USA*). Following exposure, the wafers were post exposure baked on hot plates at 65°C for 5 minutes and 95°C for 10 minutes. The wafers were then submerged in SU-8 developer (*MicroChem Corp., MA, USA*) for 15-30 minutes until fully developed, and subsequently washed with isopropyl alcohol. After the wafers were dried with compressed N_2, they were silanized using the same process for the micropost array substrate micromolds.

PDMS Stencil Micromolding

PDMS thin-film stencils were fabricated by micromolding PDMS mixed at a 10:1 w/w ratio. PDMS was mixed and degassed for 30 minutes, placed in a syringe, and dropped sparingly onto the SU-8 micromolds. Using compressed air, the PDMS (approximately 2 g) was distributed evenly to coat the micromolds. Spin coating was not employed in this step due to poor (streaky and bubbly) distribution of the PDMS. The PDMS was then compressed into the molds using a weight separated by plastic transparencies to prevent adhesion of the PDMS to the weight. This methodology minimized the amount of PDMS coating the top surfaces of the features, thereby generating thru-holes in the thin-films. To cure the PDMS, the compressed stencils were heated on hot plates for 12 hours at 40°C.

Thin-film Stencil Preparation

Prior to use, the thin-film stencils were inspected for thru-holes. If the micromolds were not overly silanized, the PDMS coating the top surfaces of the features would stick to the developed SU-8, separating it from the thin-films, and resulting in clean openings. However, if the PDMS coating the top surfaces was too thick or the micromolds were nonstick from excessive silanizing, lightly running the blunt side of a scalpel over the SU-8 features and using Scotch tape could remove any excess PDMS occluding the holes. After demolding, the thin-film stencils were sonicated in 100% ethanol for 10 minutes, and subsequently sterilized and washed for one minute intervals in 70% ethanol, twice in sterile DI water, and twice in sterile PBS. Considering the stencils are highly hydrophobic, it is best to prepare these and submerge them in PBS for at least one day to render them more hydrophilic before use to minimize the trapping of air bubbles in the thru-holes during experiments.

Prior to seeding, the micropost array substrates and thin-film stencils were dried and placed in contact with one another. Failure to dry all surfaces of the substrates and the stencils completely would cause poor contact between the two, and result in lift-off of the stencils and leakage of cells onto all parts of the substrates.

3.3.2 Cell Preparation for Collective Cell Migration Studies

BAECs were used for all collective cell experiments. An mCherry-Actin transfected BAEC line was also used for these experiments, and was prepared and seeded using the same protocols.

All BAEC lines used for collective cell experiments were prepared in a manner similar to that of the single cell experiments. However, the cells were trypsinized for a shorter amount of time, about 3 minutes, to maintain some clustering of the cells. Additionally, the cells were seeded at a density of approximately 3-4 times confluency (156000-208000 cells/cm^2) to ensure that some cells would fall into the thru-holes of the stencils. Due to the hydrophobicity of the thin-film stencils, bubbles were often trapped at the holes, precluding cells from reaching the micropost array substrates. To remedy this, pipetting near the holes gently displaced the bubbles with cell suspension. The cells were allowed to attach to the micropost substrates for three hours before the excess cells were washed away, and the cells were left to incubate in the stencils for 3 days before experiments. This ensured that the cell collectives were able to create cell-cell junctions before being released and observed. To release the cell collectives, the thin-film stencils were carefully removed while submerged in media with sterile tweezers. All DMEM was replaced with supplemented CO_2 independent media following stencil removal for microscope observation.

3.3.3 Methods for Observing Collective Cell Migration

Time-lapse Microscopy

Collective cell migration was observed using either time-lapse phase contrast (same setup as that used for single cell studies) or bright field microscopy with images taken every 20 minutes for 16-hour periods. Bright field time-lapse images were taken using custom programs on the ImageXpress® Micro System (*Molecular Devices, LLC, CA, USA*) with a Photometrics $CoolSNAP_{HQ}$ digital charge-coupled device (CCD) camera and MetaXpress 3.1.0.89 software. The ImageXpress® Micro System also has a temperature controlled chamber to maintain the cells at 37°C. In all experiments, collective cell migration was observed through the PDMS substrates and therefore did not require custom glass slide fixtures.

Antibody Staining

All cells were stained using standard protocols in a non-sterile environment with non-sterile reagents. Briefly, after aspirating all media, all samples were rinsed in PBS twice (one

minute/wash) and fixed using 4% paraformaldahyde for 15 minutes. After rinsing in PBS twice, samples were submerged in 0.1% Triton-X for 6-10 minutes, depending on the targeted proteins. Surface proteins, such as VE-cadherin, would require a 6 minute Triton-X treatment, while 10 minutes was required for internal cellular proteins. The samples were again rinsed twice in PBS (one minute/wash) and blocked with 1% bovine serum albumin (BSA) for 30 minutes. Using a 1:200 dilution in 1% BSA, the primary antibodies were placed onto the cells (100 μl/cm^2), covered with parafilm squares, and incubated at 4°C for 12 hours. Parafilm squares were used to ensure that the suspension of antibodies covered all parts of the samples through capillary action. The squares should be cut slightly smaller than the actual samples and should only be removed after the entire sample is submerged. The parafilm squares will be automatically released to prevent damage to the sample surfaces. Between the primary and secondary antibodies, there were three 15 minute washes, 2x PBS-Triton-X and 1x PBS. For the secondary antibodies, the antibodies were diluted to a 1:500 ratio in PBS and pipetted onto the cells (100 μl/cm^2), covered with parafilm squares, and incubated at room temperature for one hour. The same three 15 minute washes were repeated and the samples were incubated with a 1:1000 dilution of DAPI for 10 minutes. The samples were washed twice in PBS for 10 minutes, moved to glass slides, and mounted with fluoromount. To keep the samples from drying out, coverslips were place on top of the substrates and fixed in place with nail polish.

Data Acquisition and Analysis

Collective cell behavior data was collected from time-lapse images and analyzed using ImageJ software. To quantify cellular behavior, the expansion or contraction of the cell collectives was tracked over time by calculating their areas with respect to time. Considering that the collectives varied in initial size and shape, the expanded or contracted areas were normalized to their corresponding initial areas to compensate for these discrepancies. All data is presented as means and s.e.m. These were calculated directly from the data and processed using the same statistical methods as used for the single cell studies.

All stained samples were imaged using the ImageXpress® Micro System (epi-fluorescence), the Swept Field Confocal Microscope with Prairie View Imaging software (*Prairie Technologies, Inc., WI, USA*), or LSM 700 Flexible Confocal Microscope with Zen 2009 software (*Carl Zeiss Microscopy, LLC, NY, USA*). All image post-processing was done using ImageJ software.

3.4 Results and Discussion

3.4.1 Device Fabrication

Using design rules and fabrication methods from the micropost array gradients used for the single cell experiments, the *μVRs* and *μSGs* yielded well-formed microposts (**Figure 3.8.A**). However, for the *μVHs*, fabrication was attempted with both OiR 897-10i (*Fujifilm, RI, USA*) and SPR-220. SPR-220 is difficult to spin-coat at heights lower than 5 μm due to its high viscosity. Therefore, shorter microposts were attempted with OiR 897-10i by spin-coating multiple layers of photoresist using the standard programs on *svgcoat2*. Unfortunately, OiR 897-10i did not expose well on *gcaws2*, and could not yield viable micropost arrays at heights greater than 2 μm. Results in **Figure 3.8.B** illustrate deformed microposts with noncircular cross-sections.

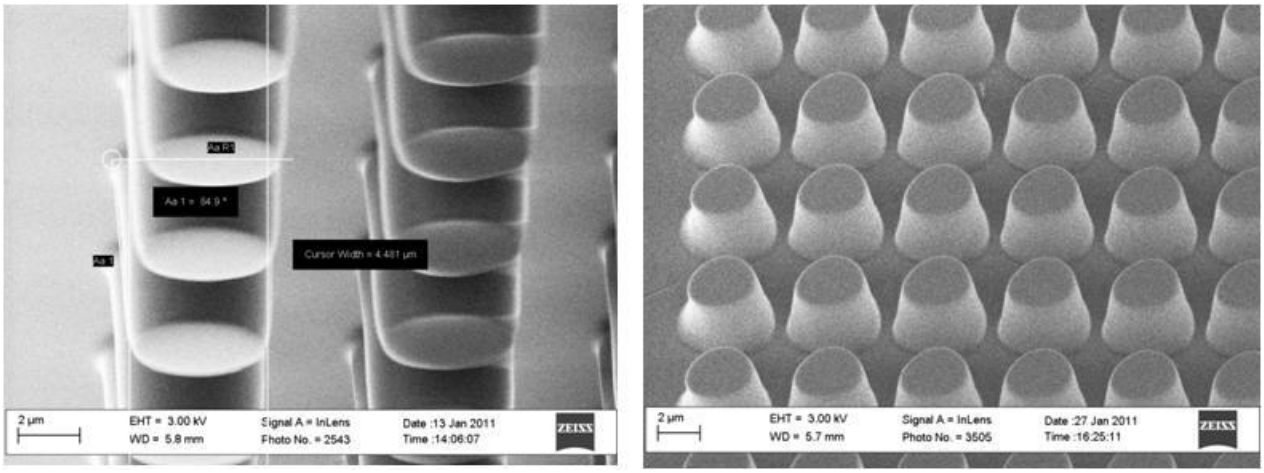

Figure 3.8. Comparison of micropost profiles.
Microposts were fabricated using two photoresists, SPR-220 (*left*) and OiR 897-10i (*right*). In both cases, target feature heights were 5 μm. Using custom programs for SPR-220, micropost arrays with relatively straight side walls were achievable. However, using multiple standardized coating steps on *svgcoat2* to created resist thicknesses of 5 μm, features patterned using *gcaws2* were warped and unable to maintain the desired height after processing. SPR-220 was, therefore, used to create micropost arrays with heights equal to or greater than 5 μm.

Prior to using soft lithography, laser ablation was considered for thin-film stencils fabrication. PDMS was spin-coated onto photoresist-coated silicon wafers at thicknesses ranging from 25-60 μm, and subsequently cured and ablated using lasers in a materials processing laboratory and a femto-second laser. Photoresist was used as a release layer for the PDMS. Results from the laser system in the materials processing laboratory can be found in **Figure 3.9**-*left*. While arrays of appropriately-sized thru-holes could be quickly produced in the PDMS thin-films, significant thermal crazing and warping were found upon closer examination (**Figure 3.9**-*right*). Interactions with the underlying photoresist also occurred and stained the thin-films. To

address these issues, a femto-second laser was tested to determine if the thermal damage could be minimized. The holes produced were cleaner and had less thermal damage; however, the spot size of the lasers was much smaller than 15 μm in radius and would not be viable for collective cell seeding considering that BAECs can easily spread to that size.

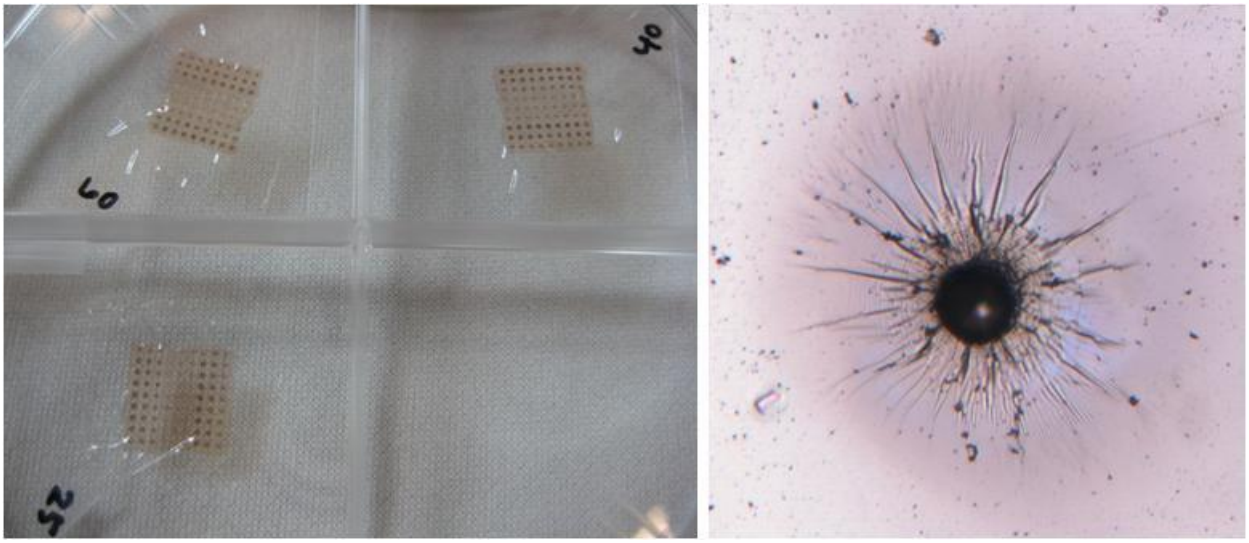

Figure 3.9. Thin-film stencil laser ablation results.
PDMS was spin-coated onto photoresist-coated wafers. (*Left*) PDMS was spun at thicknesses of 25-60 μm and ablated using the laser cutters in a materials processing laboratory. Arrays, 1 x 1 cm^2, of thru-holes were rapidly produced. However, extensive thermal damage was caused by the laser ablation (*right*), resulting in warping of the thin-film and crazing around the thru-holes which could result in leakage of cells. The hole diameter is approximately 180 μm.

Due to the fabrication issues associated with laser ablation, soft lithography was employed to create the thin-film stencils used in all collective cell experiments. The thin-film stencils were patterned with both circular and elliptical thru-holes. The fabrication results can be found in **Figure 3.10**. Stencils with diameters and major axes in the range of 50-400 μm have been designed and fabricated, all of which could produce features with clean side walls as shown in the SEM micrographs. However, the probability of yielding continuous and dense cell collectives was affected by fabrication issues and geometry. Features with diameters smaller than 75 μm rarely produced thru-holes, and the scalpel method of opening the holes marginally increased viability without damage to the features. Additionally, thru-holes that were less than 100 μm in diameter were very difficult to seed – even when seeding at high density, BAECs had difficulty being seeded collectively in these holes.

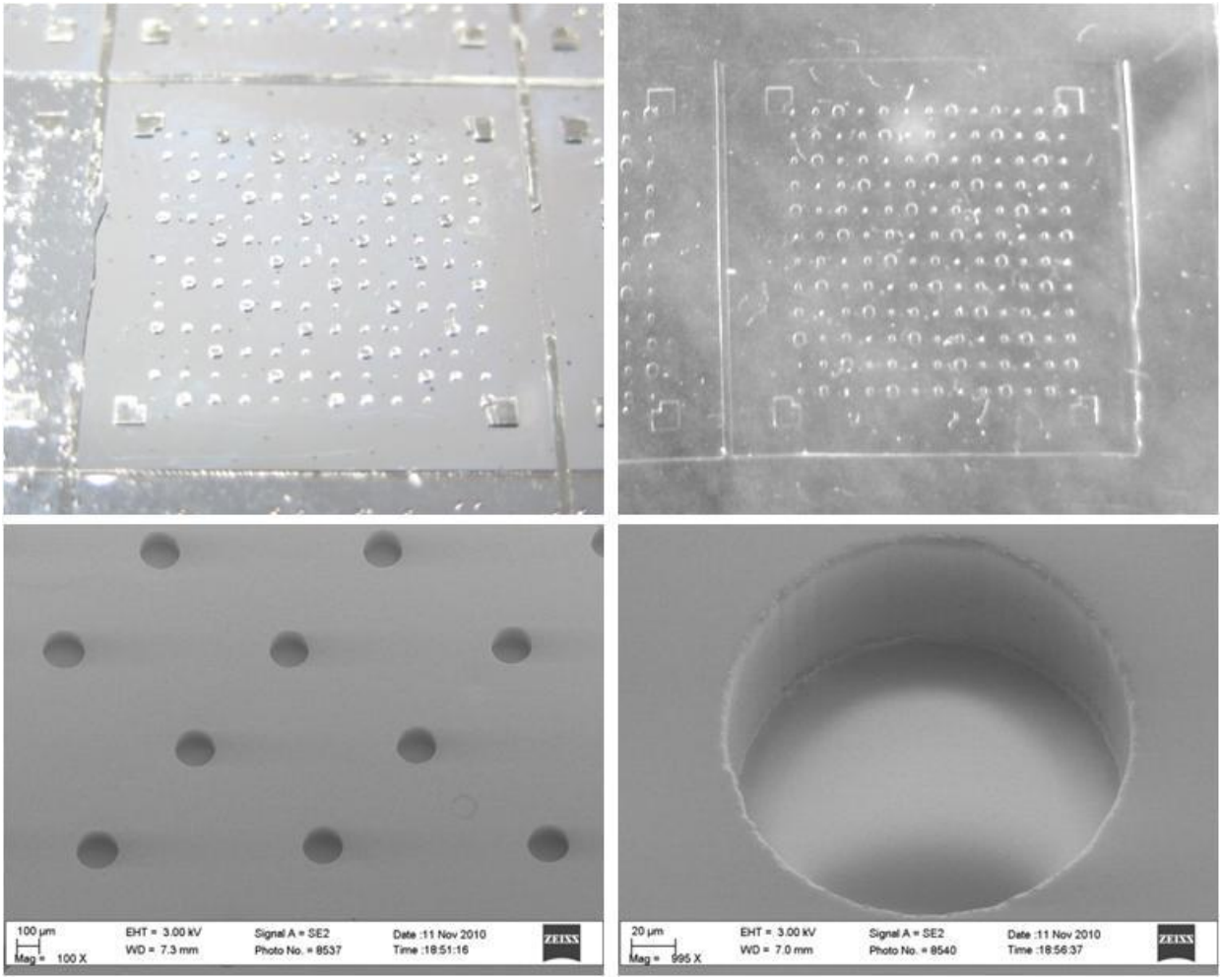

Figure 3.10. Thin-film stencil fabrication results.
The thin-film stencils were fabricated using a one-mask soft lithography process. PDMS was compressed into SU-8 micromolds with features 100 μm in thickness (*top left*) and demolded (*top right*) after curing under external weights. Each stencil was approximately 1 x 1 cm^2 in size. (*Bottom left*) SEM micrographs of the stencils show cleanly resolved features and straight side walls (*bottom right*).

3.4.2 Cell Seeding and Collective Formation

Cell collectives were formed by seeding the stenciled micropost array substrates at high densities and incubating them until the formation of cell-cell junctions. Stenciled micropost arrays can be found in **Figure 3.11**. Residual PDMS from the scalpel method can be seen along the edges of an elliptical thru-hole in **Figure 3.11**-*left*, which can account for slight imperfections at the edges of cell collectives. A thru-hole seeded with BAECs can be seen in **Figure 3.11**-*right*. Even when seeding at a density equivalent to confluency, it was difficult to localize the cells within the stencil openings due to trapped air bubbles at the thru-hole locations. Seeding cells at higher densities, such as 3-4 times confluency, helped to increase cell localization within the stencil openings and yielded dense cell collectives. Low density clusters of cells could not form

continuous cell collectives, rendering them irrelevant for experiments. Effects of seeding density of cell collective formation can be found in **Figure 3.12**.

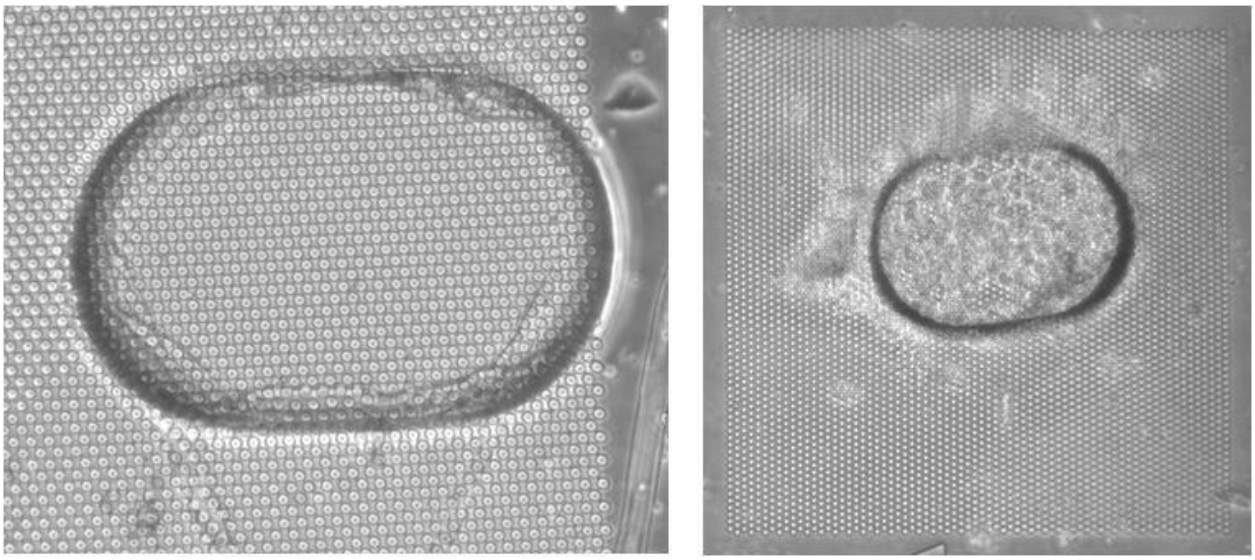

Figure 3.11. Stenciled micropost array substrates.
Thin-film stencils were used to selectively culture and locate cell collectives on micropost array surfaces (*left*). Thru-holes occasionally required manual opening with the scalpel method, which created residual PDMS at the edges. This resulted in slight impefections at the edges of cell collectives. (*Right*) A stenciled micropost array substrate after high density seeding with BAECs and a 3 day incubation period. Major axis length for both thru-holes is approximately 250 μm.

The thin-film stencil fabrication method was able to yield well-formed thru-holes that did not require manual opening. Even with these thru-holes, BAECs, while able to form dense cell collectives, were generally unable to maintain a perfect replica of the thru-hole shape after stencil removal, as shown in **Figure 3.12**-*right*. This is likely due to some cellular attachment at the edges to the stencils, which can result in mechanical breakage of cell-cell junctions during stencil removal.

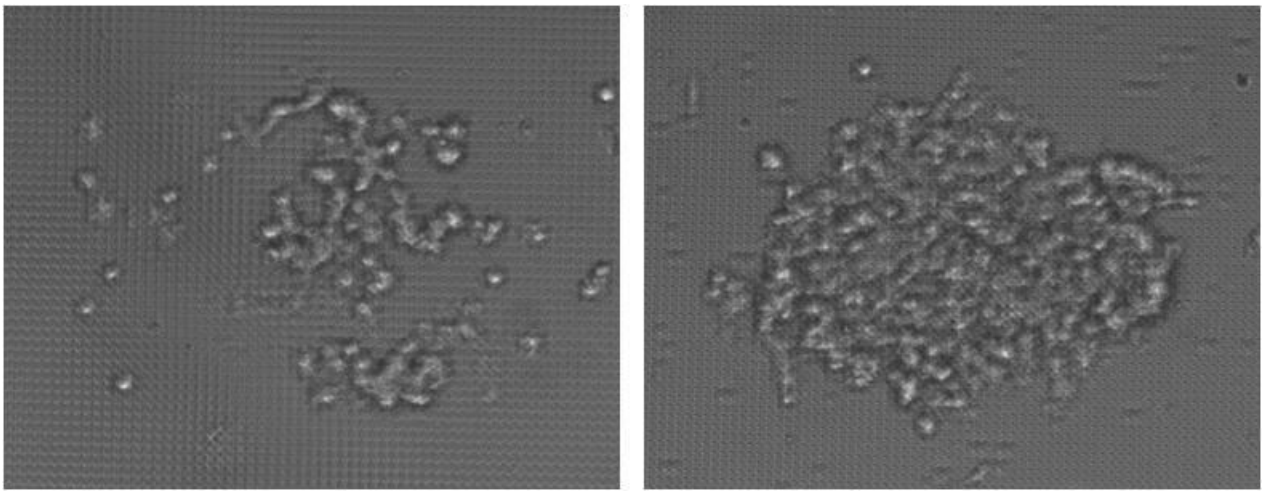

Figure 3.12. Seeding densities for collective cell experiments.
To create continuous collectives of cells, BAECs needed to be seeded at high densities to ensure thru-holes in the thin-film stencils were densely populated. (*Left*) Stencils seeded at confluency produced poorly formed, sparse collectives that could not be used for collective cell studies. In contrast, seeding at (*right*) three times confluency yielded continuous collectives of cells. The slight irregularities at the edges of the collective are likely caused by mechanical breakage of cells attached to the side walls of the stencil thru-holes. This collective is approximately 300 μm at its widest part.

To determine the types of junctions that were being formed by the cells after three days of incubating in the thru-holes of the thin-film stencils, BAECs collectives were fluorescently stained for cell-cell junctions and cell-substrate junctions. In **Figure 3.13**, a BAEC collective was visualized under bright-field and fluorescent illumination at 20x magnification. As shown in **Figure 3.13.A**, while the cell collective was not well visualized under bright-field illumination, the micropost substrate (μ*VRs* with radii of 1.5 μm) below was visible. The microposts in this image had an uneven appearance – this is due to stiction, which causes groups of microposts to collapse onto one another. **Figure 3.13.B** shows the cell collective through the nuclei of the BAECs using DAPI (blue) staining. The outline of the BAECs can be seen in **Figure 3.13.C** through the staining of the cell-cell junctions (adherens junctions), where VE-cadherin (*Santa Cruz Biotech, CA, USA*) was stained with FITC (green). This staining indicated that cell-cell junctions had formed and that the BAEC collectives were physically connected and not loosely clustered cells through hydrophobic/hydrophilic interactions. In **Figure 3.13.D**, cell-substrate junctions (focal adhesions), which also formed during the incubation period, were stained using Vinculin (*Sigma-Aldrich, Corp., MO, USA*) with TRITC (red). The cell collectives formed using the stenciling technique were 3-D collectives, not monolayers, as indicated by confocal microscopy and account for the lack of a circular or elliptical appearance of the cell collective in **Figure 3.13**.

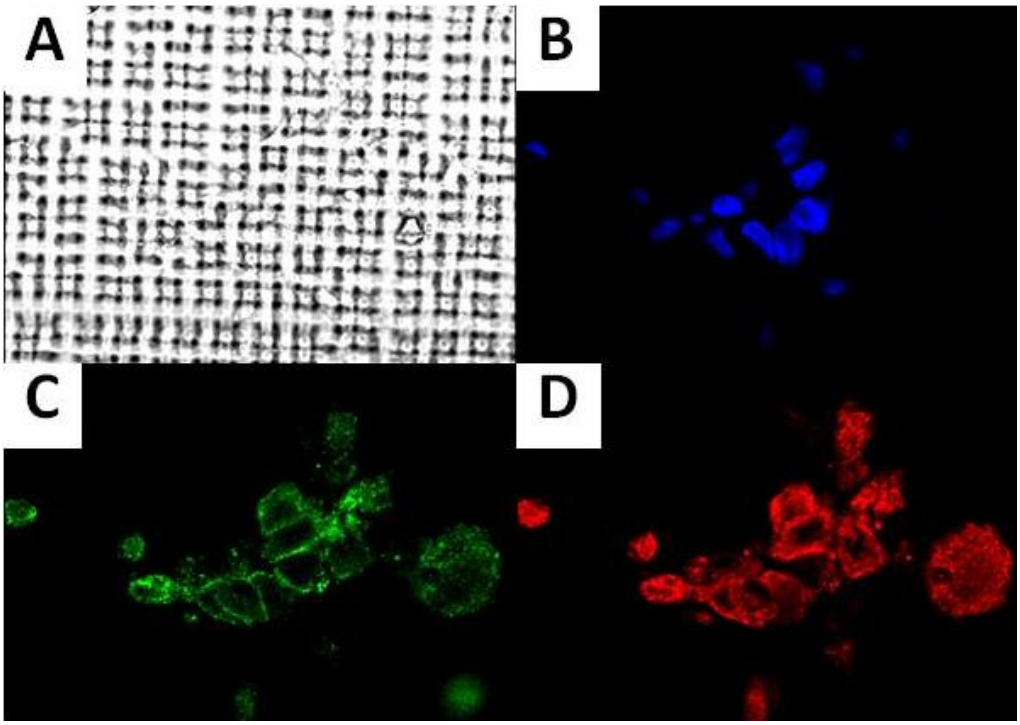

Figure 3.13. Formation of cell-cell and cell-substrate junctions for cell collectives.
To determine the types of junctions the BAECs were forming during the three day incubation period, the cell collectives were stained for both cell-cell and cell-substrate junctions. BAEC collectives on micropost substrates (*A*) were stained for (*B*) nuclei (DAPI, blue), (*C*) VE-cadherin for adherens junctions (FITC, green), and (*D*) Vinculin for focal adhesions (TRITC, red). (*A*) While the cell collective was not visualized under bright-field illumination, the underlying micropost substrate (*μVRs* with radii of 1.5 μm) was visible. The microposts had an uneven appearance due to collapse from stiction. (*B*) The cells in the collective are localized through the nuclei staining, showing a non-circular/non-elliptical collective. From (*C*), the outline of the cells was visible through positive staining of VE-cadherin, indicating the BAECs had formed physical junctions with one another. The collectives also formed cell substrate junctions as illustrated in (*D*) through the positive staining for Vinculin. Confocal imaging of BAEC collectives indicated that they are 3-D clusters, not monolayers of cells. Magnification = 20x.

3.4.3 Collective Cell Results: *μVR*, *μVH*, and *μSG*

Experimental results for the *μVRs* indicated that changes in micropost radii could maintain or inhibit collective cell behavior. Time-lapse images of collective cell behavior can be found in **Figure 3.14**-*left*/*middle*, with images taken every four hours. To quantify collective cell behavior, the expansion or contraction of the collective areas was tracked over 16-hour periods and normalized to the original corresponding collective area. This normalization accounted for slight differences in the original areas of different collectives. Normalized expansion and contraction area data over the 16-hour studies can be found in **Figure 3.15**, where values greater than 1 indicate expansive behavior, and values less than or equal to 1 denote contractile behavior.

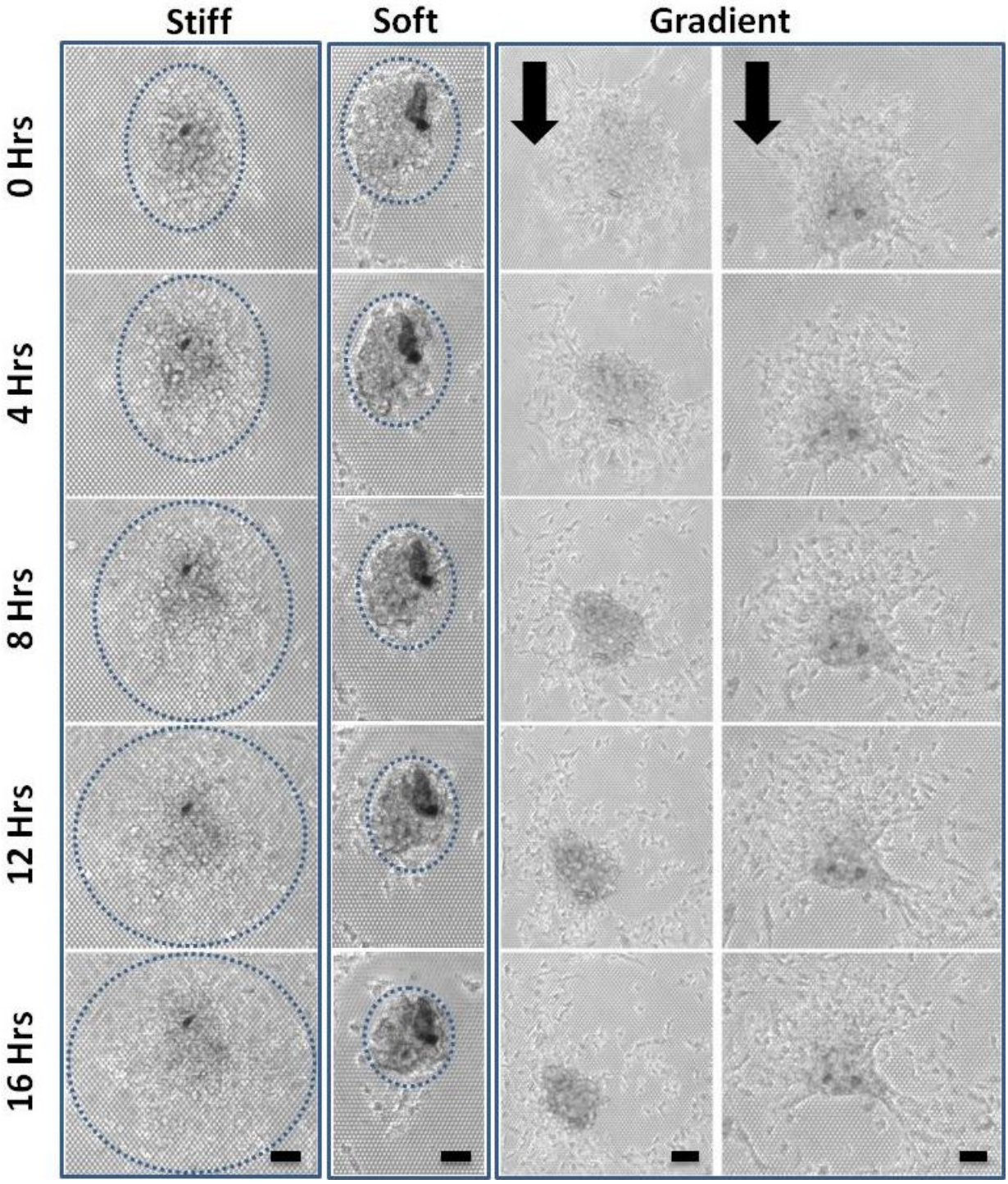

Figure 3.14. Experimental time-lapse collective cell results for *μVRs* and *μSGs*.
Time-lapse images for cell collectives on stiff, soft, and gradient micropost arrays. On the stiff *μVRs*, collective cell behavior was inhibited, with collectives dispersing into single cells. In contrast, on the soft *μVRs*, collective cell behavior was maintained. The dotted circles approximate the expansion or contraction of the cell collectives. While some cells are lost at the periphery, cell collectives remain as collectives. On the *μSGs*, behavior was found to be more complex, with cell collectives exhibiting expansion and contraction at different edges. Black arrows indicate the direction of decreasing interpost spacing. For stiff *μVRs* and *μSGs*, bars = 100 μm. For soft *μVRs*, bar = 50 μm.

For the *μVRs* with radii in the range of 1.75-2.25 μm, results indicated that collective cell behavior could not be maintained and the collectives expanded over time (**Figure 3.15).** These micropost arrays were classified as "stiff", and caused cell collectives to break apart and migrate radially away as single cells from the group. On the stiff arrays, it was found that collectives would have larger average expanded areas over time with increasing micropost radii. On the *μVRs* with radii of 1.75 μm, 2.0 μm, and 2.25 μm, the final average normalized expanded areas (greater than 1) were 3.0 ± 0.1, 3.3 ± 0.2, and 4.5 ± 0.5, respectively. While the differences in expansion between the *μVRs* with radii of 2.25 μm and 2.0 μm was not considerable (p = 0.09), the difference between the *μVRs* with radii of 2.25 μm and 1.75 μm was found to be statistically significant ($p < 0.05$).

In contrast to the stiff *μVRs*, on the *μVRs* with radii of 1.5 μm, cell collectives were able to maintain their collective behavior (less than or equal to 1) and even contract, with a final normalized expanded area of 0.7 ± 0.1. These micropost arrays were considered "soft". During experiments, cells at the periphery did break away intermittently; however not at the consistency and speed with which cells moved away from the collectives on the stiff *μVRs*. The difference in behavior between the soft and stiff surfaces was found to be statistically significant, with $p <$ 0.05. As the behavior of cell collectives changes between micropost arrays with radii of 1.5 μm and 1.75 μm, this transitional stiffness zone where collective cell behavior can no longer be maintained is characterized as 33 ± 9 nN/μm.

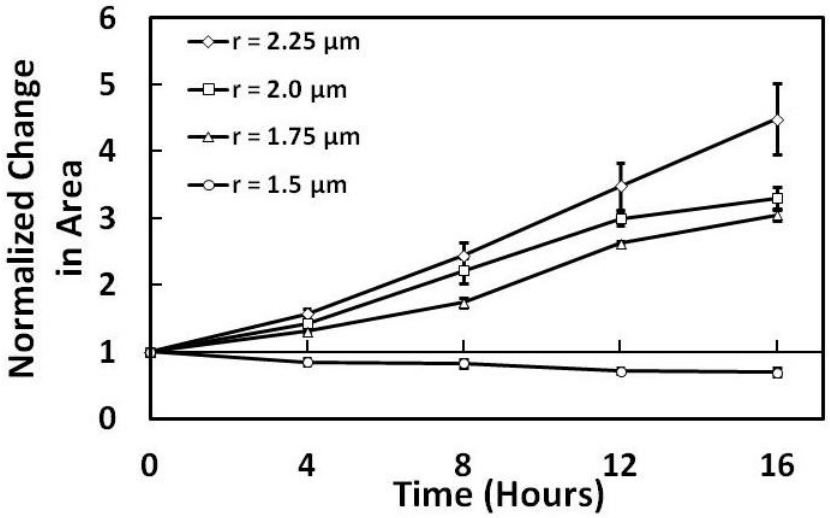

Micropost Radius (μm)	Number of Cell Collectives
2.25	7
2.0	3
1.75	3
1.5	5

Figure 3.15. Normalized expansion and contraction data for the *μVRs.*
(*Left*) To quantify collective cell behavior, the expansion or contraction of cell collectives on the *μVRs* were tracked over 16-hour periods. To account for different sizes of collectives, these were normalized to their initial corresponding areas. As this is a normalization, values greater than 1 described expansion and values less than or equal to 1 indicated contraction, which are the inhibition or maintenance of collective cell behavior, respectively. For the microposts with radii between 1.75-2.25 μm, collective behavior could not be maintained and single cell migration was induced. In contrast, on the microposts with radii of 1.5 μm, cells maintained their group behavior and exhibited contraction. Error bars denote s.e.m. (*Right*) The number of cell collectives tested for each radius is tabulated.

To further investigate possible differences between collective cell behaviors on the stiff and soft *μVRs*, collectives of a transfected BAEC cell line were used. The BAECS were transfected such that Actin, which was used to visualize the cell cytoskeleton, was fluorescently labeled with mCherry. In **Figure 3.16**, cell collectives were visualized with Actin by mCherry (Cy3, green) and with nuclei by DAPI (blue) staining. Microposts in **Figure 3.16.B,D** were stained with fluorescently-labeled BSA (Cy5, red).

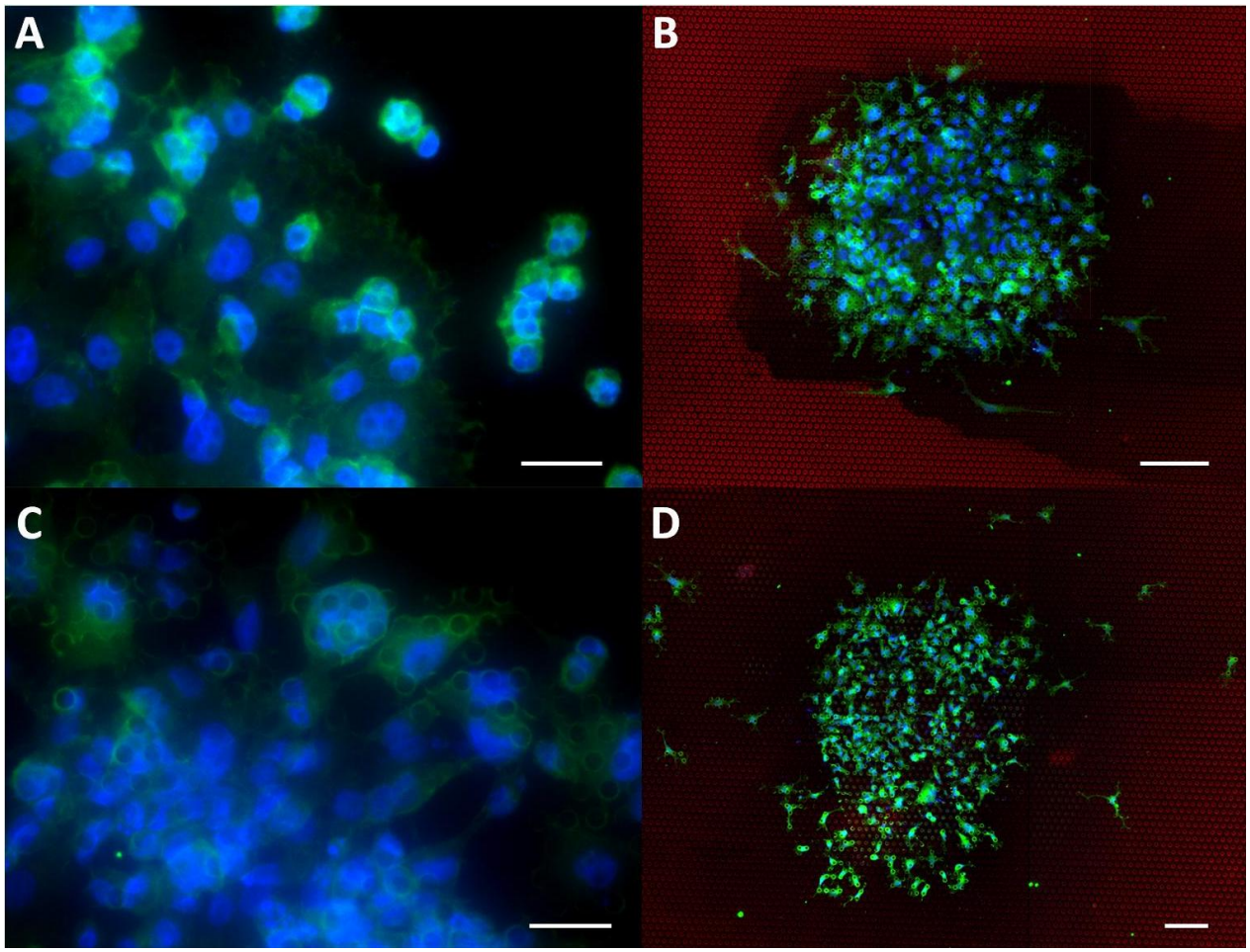

Figure 3.16. Fluorescence images for collective cells.
Cell collectives with BAECs transfected with mCherry-Actin on *μVRs* with radii of (*A,B*) 1.5 *μ*m and (*C,D*) 2.5*μ*m. For all images, the cytoskeleton of the BAECs in collectives was visualized through mCherry (Cy3, green) and the cells were localized through their nuclei (DAPI, blue). Directly after stencil removal, collectives on the *μVRs* with radii of (*A*) 1.5 *μ*m and (*C*) 2.25 *μ*m were stained for nuclei and Actin. The edges of the collective on the *μVRs* with radii of 1.5 *μ*m appear to be more continuous than the one on the surface with 2.25 *μ*m microposts, suggesting that cells on these surfaces are able to form cell-cell junctions more easily. Magnification = 40x. Bars = 20 *μ*m. After 8 hours of incubation, the maintenance (contraction) and inhibition (expansion) of collective behavior can be seen on *μVRs* with (*B*) 1.5 *μ*m and (*D*) 2.25 *μ*m radii microposts (Cy5, red), respectively. (*B*) The cell collective on the *μVRs* with radii of 1.5 *μ*m was mostly intact after the 8 hour incubation period, losing only a few cells at the periphery. (*D*) In contrast, after 8 hours, the cell collective on the *μVRs* with radii of 2.25 *μ*m had dispersed, with significant single cell migration. Magnification = 10x. Bars = 50 *μ*m

After incubating for three days in the thin-film stencils, collectives on *μVRs* were stained immediately after stencil removal (**Figure 3.16.A,C**) and after eight hours of incubation (**Figure 3.16.B,D**). In **Figure 3.16.A**, a collective on a *μVRs* with radii of 1.5 μm exhibited a fairly continuous edge, with overlap of cytoskeletons of neighboring cells seen through the mCherry-Actin. Unattached cells appeared round and not spread out. The microposts could be visualized through the nuclear stains, likely from the deformation of the nuclei. In contrast, on the *μVRs* with radii 2.25 μm (**Figure 3.16.C**), the edge of the collective is not continuous with cells appearing loosely attached to one another in spite of the higher cell density. Individual cells appear more spread out in comparison to those on the *μVRs* with radii of 1.5 μm. Microposts can also be seen in the nuclear stains of the cells. These edge differences suggest that cells on the substrates with softer microposts have stronger tendencies to form cell-cell junctions more easily than those on the surfaces with stiffer microposts. The overall differences between the two surfaces can be seen after eight hours of incubation. In **Figure 3.16.B**, a collective on the *μVRs* with radii of 1.5 μm has been maintained or exhibited slight contraction with a few cells leaving at the periphery. In contrast (**Figure 3.16.D**), the collective on the *μVRs* with radii of 2.25 μm has expanded with many single cells migrating away from the group.

Although these results suggest that changes in collective cell behavior can be attributed to changes in micropost radii (stiffnesses), interpost spacing also varies for the different arrays and may influence this behavior as well. Since these *μVRs* have a *%ECM* of 0.2 to maintain constant microtopographic area for microposts of different radii, the interpost spacing for radii 1.5-2.25 μm increases from 1.47 μm to 2.21 μm. To investigate possible changes in behavior due to spacing, collective cell behavior was observed on the *μSGs*, which have microposts with identical geometry to the *μVRs* with radii of 1.5 μm as well as gradients in interpost spacing. For cell collectives on *μSGs*, experimental results indicated multiple behaviors that were markedly different from behavior on any of the *μVRs*. Time-lapse images of cell collectives on these surfaces, taken every four hours, can be found in **Figure 3.14**-*right*. From the time-lapse images, it was observed that at different parts of the collective, contraction of the collective can occur while the overall cell collective is expanding. To quantify the overall behavior of the collectives, the average normalized expansion of the collectives was tracked for 16-hour studies (**Figure 3.17**).

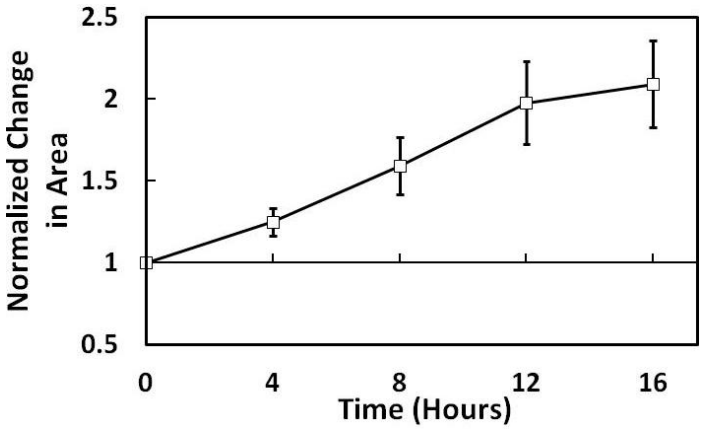

Figure 3.17. Experimental collective cell data for micropost array gradients.
Although all of the cell collectives on the *μSGs* had portions that exhibited contraction, the expansion areas were recorded for 16-hour studies to characterize their overall behavior. Cell collectives were not able to fully maintain their group behavior on these gradients, indicated by values greater than 1, despite having the same substrate stiffness stimuli as the *μVRs* with radii of 1.5 μm. Error bars denote s.e.m.

Four cell collectives were observed and found to have a normalized change in area of 2.1 ± 0.3 after 16-hour periods, which is statistically different from that of the *μVRs* with radii of 1.5 μm, where cell collectives were able to contract and maintain their group behavior. Cell collectives exhibited an overall expansion on these surfaces even though portions of the collectives did exhibit some contractile behavior. This contractile behavior was characterized by measuring the displacement of the centroids of the cell collectives over 16-hour studies. The average centroid displacement of the four collectives was found to be approximately 84.5 ± 35.8 μm. Although the contractile behavior of specific portions of the collectives occurred in both the directions of decreasing and increasing interpost spacing, general effects of the spacing gradient may not be observable as only four collectives were tested. Overall, the expansive behavior indicated that, even with the same substrate stiffness cues, the larger interpost spacing can cause the expansion of the cell collectives.

These results could be attributed to physical difficulties cells may have with forming and maintaining cell-cell junctions with one another. Similar to how single BAECs might have been unable to physically reach subsequent microposts that are spaced farther and farther away on the *μDSGs*, BAECs at the edges of collectives on the *μSGs* may not be close enough to one another to form sufficient numbers of or strong enough cell-cell junctions to balance the cell-substrate adhesion forces required to maintain collective cell behavior. At the center of collectives, where cell density is very high and spacing between cells should not be an issue, different phenomena might explain this behavior. It might be possible that BAECs need to form a sufficient amount of cell-substrate junctions in order to form cell-cell junctions well. On the *μSGs*, cells have less topographical area to anchor to due to the *%ECM* of 0.15. While the hypothetical force balance described in literature suggests that cell-cell junctions and cell-substrate junctions work

antagonistically to inhibit and maintain collective cell behavior, there might be a minimum balance between the two required for tissue functionality.

Since interpost spacing can possibly affect collective cell behavior, cell collectives were observed on *μVHs* for 16-hour periods. These *μVHs* have the same micropost diameter at 1.5 μm and same interpost spacing while the microposts have different heights of 5 μm and 6 μm. These have the same microtopographic layout as the *μVRs* with radii of 1.5 μm, which has a height of 7 μm. Time-lapse images, taken every four hours, of expansion on these substrates can be found in **Figure 3.18**. From these images, it is clear that on these microposts arrays, collective cell behavior cannot be maintained, similarly to the stiff *μVRs* with larger radii. Their expansion data, compared to the *μVR* with radii of 1.5 μm, can be found in **Figure 3.19**. Specifically, for heights of 5 μm and 6 μm, the final normalized expanded areas were 4.6 ± 0.6 and 3.8 ± 0.5, respectively. It is observed that the expansion of cell collectives on these surfaces tends to increase with decreasing height, but these results were not statistically different ($p = 0.3$). However, the difference between these results and the *μVR* with radii of 1.5 μm was statistically significant ($p < 0.05$). These results further validate the experimental observation that there is a zone where collective behavior can no longer be maintained on micropost arrays with radii of 1.5 μm between the heights of 6 μm and 7 μm and this transitional stiffness can be characterized as 30 ± 6 nN/μm.

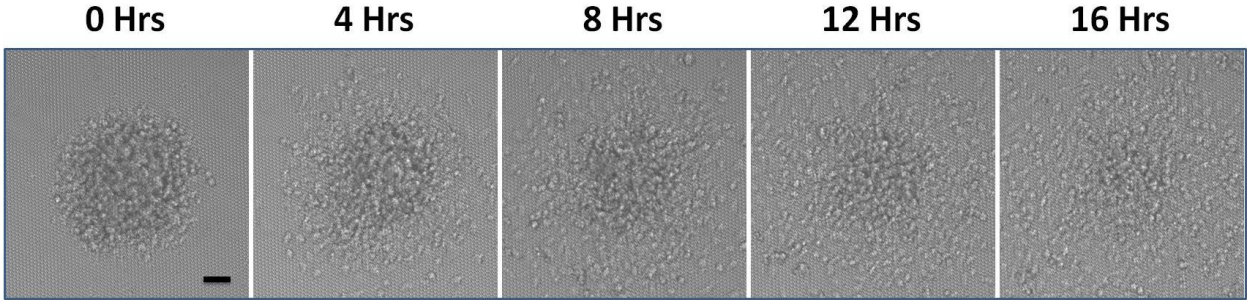

Figure 3.18. Experimental time-lapse collective cell results for *μVHs*.
Time-lapse images for cell collectives on *μVHs* for 16-hour studies. Similar to the *μVRs*, with radii between 1.75-2.25 μm, collective cell behavior was inhibited and the expansion of the collectives was observed for both *μVHs*. Bar = 50 μm.

These results show that the expansive behavior was found for both the *μVRs* and the *μVHs*. Micropost stiffness can likely play a role in mechanically regulating collective cell behavior. Additionally, the *μVRs* with radii 1.75 μm and 2.0 μm have similar but slightly stiffer microposts than the *μVHs* with heights of 6 μm and 5 μm, respectively, as shown in **Figure 3.5**. Based on the expansion results for both the *μVRs* and *μVHs*, the collectives on the *μVRs* might be expected to expand slightly faster than they would on the *μVHs*. However, it is interesting to note that, while not statistically significant, cells spread faster on the *μVHs* relative to the *μVRs*. Based on the single cell migration data for the *μDSGs*, where cells migrated faster in the direction of decreasing interpost spacing (approximate range of 2 μm to 6 μm) relative to the opposite

direction, this result might again demonstrate the influence of interpost spacing on cellular migration.

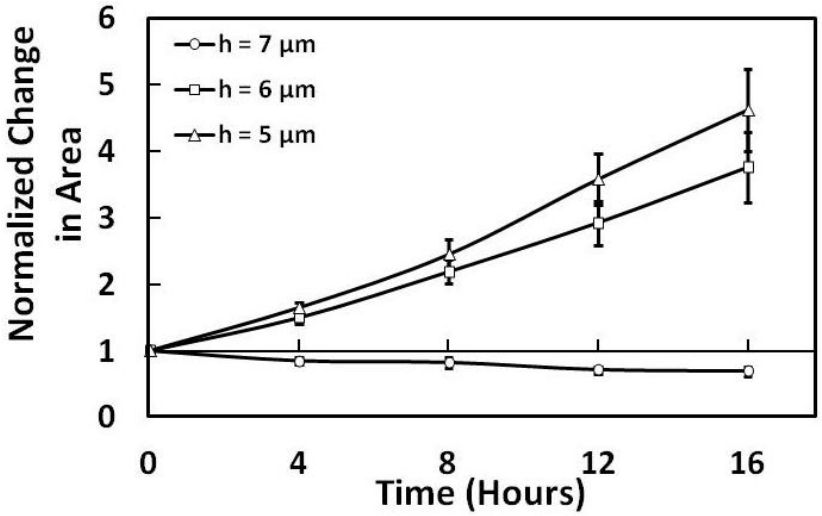

Micropost Height (µm)	Number of Cell Collectives
7	5
6	4
5	4

Figure 3.19. Normalized expansion and contraction data for the *µVHs*.
The expansion and contraction of cell collectives on the *µVHs* were tracked for 16-hour periods, and normalized to their corresponding initial areas. Values greater than 1 and less than or equal to 1 indicate expansion (inhibition) and contraction (maintenance) of collective cell behavior, respectively. In comparison to the *µVRs* with radii of 1.5 µm, collectives on the *µVHs* could not maintain their group behavior and were dispersed into single cells. Error bars denote s.e.m. (*Right*) The number of cell collectives tested for each height is tabulated.

Chapter 4: Micropost Arrays for Cell Reprogramming

4.1 Introduction

Stem Cell Biology

The field of stem cell biology holds promise for addressing many poorly met medical challenges, including regenerative medicine, organ engineering, cell replacement therapies, and autoimmune disorders. [119–125] Stem cells are unique due to their theoretical capacity to become any type of cell in the human body depending on their level of differentiation [120], [126] – the less differentiated a stem cell is, the greater the number of cells it has the potential to become. This potential to become many types of cells is referred to as potency. While totipotent stem cells are able to become any type of cells including extraembryonic tissues, [127], [128] pluripotent stem cells are considered sufficient for most practical medical applications of stem cells as they can differentiate into any of the three germ layers. [7], [129–131] Embryonic stem cells (ESCs) are considered the gold standard for pluripotency. [128] It has been demonstrated that ESCs can differentiate into all fetal and adult cell lineages, can be implanted into embryos and play a role in tissue generation, and are capable of self-renewal. [132], [133] While they appear to be a solution to the aforementioned medical problems, they are not without their limitations. There is significant ethical controversy over the harvesting of human embryonic stem cells (hESCs) due to the way they are isolated and cultured, which requires the destruction of a human embryo. [134], [135] Also, because of the way their pluripotency is maintained, currently available stem cell lines suffer from xenographic contamination from mouse embryonic fibroblasts (MEF) feeder cell layers, or expensive chemical medias conditioned by MEFs, as pluripotency of hESCs cannot be maintained by cytokines such as leukemia inhibitory factor (LIF). [132], [136], [137] Additionally, even if the two aforementioned issues were addressed, there remains a problem of graft-versus-host disease that is common to stem cell treatments. [138–141] Human embryonic cells in culture will have immune imprinting in their derived cells, which can result in the need for host immune system suppression for actual applications. [119]

Stem Cell Reprogramming

To address the issues associated with ESCs, researchers have investigated methods of producing stem cells through alternate means. The idea of reprogramming somatic cells into stem cells has become an active area of research in the last 10 years. Reprogramming is the methodology of changing the potency of a cell body by manipulating the nuclear behavior. Methods that have been used to do this include nuclear transfer, [142], [143] cell fusion, [144] cell explantation, [145] and the technologies to create induced pluripotent stem cells (iPSCs). [146–148] While pluripotency can be induced using all of these methodologies, iPSCs have the greatest potential to overcome the limitations of ESCs. As nuclear transfer requires the use of

embryos, cell fusion results in cells that are tetraploid, and cell explantation maybe confined to germ cells, these methods have severe technical and practical limitations. [131], [149]

iPSCs have the potential to address the ethical and immunological rejection issues that are associated with ESCs. iPSCs are generated from embryonic or adult somatic cells by forcing exogenous production of transcription factors that are unique to stem cells. [147] As differentiated cells can be reprogrammed into iPSCs, this technology has wide reaching implications as they can possibly be patient-sourced. If iPSCs are patient-sourced, not only will stem cell treatments not require the use of embryos, the cells will be personalized and preclude any host rejection issues. [149]

iPSCs can be derived from both embryonic and adult somatic cells, and are reprogrammed into pluripotent states through the transduction of key stem cell factors. Delivery methods for the desired transcription factors for reprogramming can include using integrating viruses (e.g. retro-/lentiviruses [147], [148], [150], [151] and virus cassettes [152–154]), non-integrating viruses such as adenoviruses, [155], [156] plasmid transfections, [157–159] transposons, [160–162] direct protein delivery, [163–165] or mRNA delivery. [166] Several transcription factors play important roles in the propagation of undifferentiated stem cells and have been identified for reprogramming. Combinations of transcription factors, such as Oct-3/4, Sox2, c-Myc, Klf4, Lin28, and Nanog, [147], [149] are required for iPSC reprogramming. [149] Additionally, other classes of factors can improve the efficiency of the reprogramming process or replace transcription factors. These include epigenetic modifiers, signaling molecules, mRNA binding proteins, tumor suppressors, cell-cell adhesions, vitamin C, and environmental factors such as hypoxia. [167–174]

While iPSCs have significant potential for overcoming the limitations of ESCs, they have several drawbacks. Several delivery methods of the transcription factors are mutagenic (viral integration) and some of the transcription factors themselves are oncogenic such as c-Myc, which can result in undesirable side effects in the human body. [175], [176] Reprogramming efficiency is also notoriously low, often much less than 1%, which makes the process both expensive and slow. [149] Developing and researching methods that can eliminate oncogenic factors, increase the efficiency of the reprogramming process, or enable direct differentiation or transdifferentiation [177–181] of reprogrammed cells, therefore, are imperative for making medical applications of iPSCs a reality.

Microenvironmental Cues and their Effects on Stem Cells and iPSCs

As previously mentioned, while transcription factors are integral to the reprogramming process of iPSCs, secondary chemical factors in the cellular microenvironment have been shown to increase reprogramming efficiency or replace some of the transcription factors. [167–174], [182] Additionally, ESC protocols that utilize chemical growth factors for directed

differentiation into specific cell lineages, including hepatic, hematopoietic, endothelial, and neural, have been effective in differentiating iPSCs. [183–186]

Biophysical cues, which have demonstrated influence over the differentiation of stem cells, have not been explored for iPSCs. Microenvironmental stimuli, including substrate stiffness and extracellular matrix geometry, can control the differentiation of stem cells into specific desired lineages. [46], [187–192] In their seminal paper on effects of substrate stiffness on stem cell differentiation, Engler et. al. demonstrated that polyacrylamide surfaces of different stiffnesses could direct mesenchymal stem cells (MSCs) toward neuron, myoblasts, or osteoblasts lineages in identical chemical microenvironments. [46] Microtopography has also been used to direct the differentiation of stem cells. [56], [70] Uniform micropost arrays were employed to change the apparent stiffness of a substrate, and found to favor adipogenic or osteogenic fates of MSCs on soft and stiff microposts, respectively. [56] As microtopography can influence both somatic adult cell behavior and stem cell differentiation, micropost array technology may affect both the reprogramming and differentiation processes of iPSCs.

4.2 Design of Micropost Arrays for iPSCs

As a relatively new field of research, variables of the reprogramming and differentiation processes for iPSCs and the effects of microenvironmental cues are not well understood or characterized. Uniform micropost arrays, with varying radii and heights, and flat PDMS surfaces were used to explore the influence of microtopography on these iPSC processes. Furthermore, effects of initial seeding density and lentivirus infection levels were investigated.

4.2.1 Uniform Micropost Arrays: (*μVRs*)

Two sets of *μVRs*, similar to the micropost arrays utilized for the collective cell studies, were designed for the iPSC experiments (**Figure 4.2**). The *μVRs* were made at two different heights, 2 μm (μVR_2) and 7 μm (μVR_7). The micropost surfaces consisted of uniform micropost arrays with radii ranging from 1.5 μm to 3.0 μm, which enabled multiple stiffnesses at each height to be tested in parallel on the same device. As shown in the bottom figures of **Figure 4.2**, the theoretical stiffnesses for these radii are equivalent to 23.6-292.1 nN/μm and 483.6-2862.8 nN/μm for the μVR_7 and μVR_2, respectively. To avoid any issues with stiction of neighboring microposts, the *μVRs* had a reduced *%ECM* of 0.1. Microposts were spaced uniformly, dictated by the *%ECM*, in both the x- and y-directions and were arranged in a hexagonal pattern. The areas of these arrays ranged from 2500 x 2000 μm^2 to 7000 x 7000 μm^2. These arrays were larger than those made for the collective cell studies as it was difficult to seed specific densities of cells onto small areas in a repeatable fashion.

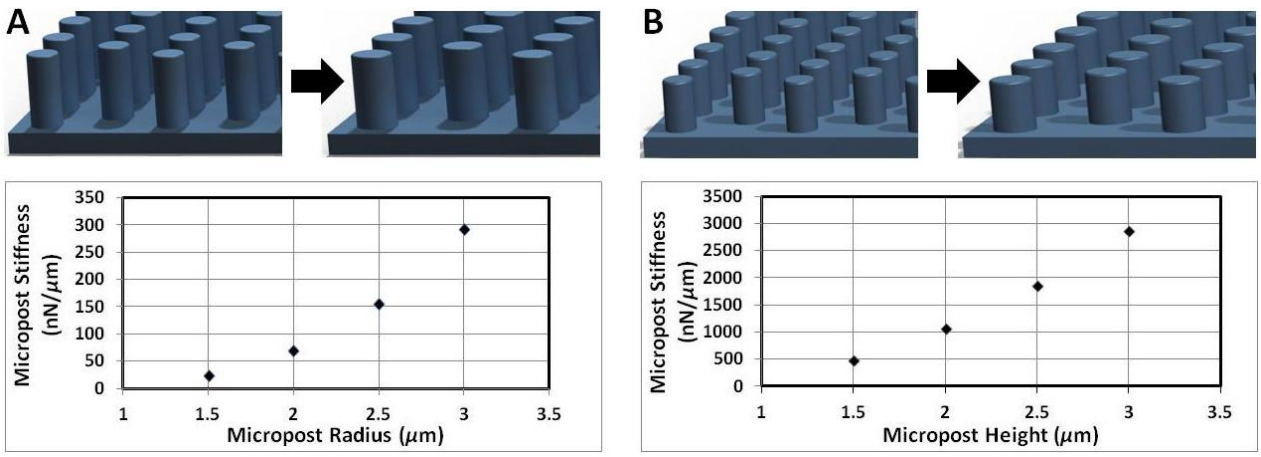

Figure 4.1. Concept schematic for the *μVRs*.
μVRs, similar to those used for collective cell studies, were fabricated for iPSC experiments. *μVRs* were made at two heights: (*A*) 2 μm (μVR_2) and (*B*) 7 μm (μVR_7). For each height, substrates were made with uniform micropost arrays with radii between 1.5-3 μm, enabling several different stiffnesses to be tested in parallel on the same device. Theoretical micropost stiffnesses were calculated for these radii for μVR_7 and μVR_2 in the bottom graphs of (*A*) and (*B*), respectively.

4.2.1 Design of Experiments

As the effects of microtopography on the reprogramming and differentiation processes have not been explored, flat PDMS surfaces were used as control substrates for the *μVR* experiments (**Figure 4.2**). From the previous single and collective cell studies, maintaining specific seeding densities on PDMS surfaces was challenging. PDMS is very hydrophobic and seeded suspensions could easily bead off the surfaces through movement of the substrates during experiment preparation. To address this issue, the cell suspensions were confined on all surfaces with PDMS frames. These frames had thru-holes, with areas of 1 x 1 cm^2 and approximately 4 mm in depth, and were utilized as large stencils (**Figure 4.2.B**). Furthermore, as chemical microenvironmental cues can influence many aspects of cellular behavior, the *μVRs* were not microcontact-printed with attachment proteins to preclude their effects.

In addition to exploring cellular responses to microtopography, the effects of initial seeding densities and viral infection levels of reprogrammed cells were investigated by varying their concentrations. Both of these factors can increase the probability of a reprogramming event by increasing the total number of available cells or the percentage of infected cells. Effects of viral infection levels on cells were compared on substrates of different microtopography. The possible effects of initial seeding density, virus infection levels, and microtopography on the reprogramming and differentiation events of cells (**Figure 4.2.C**) were observed over time.

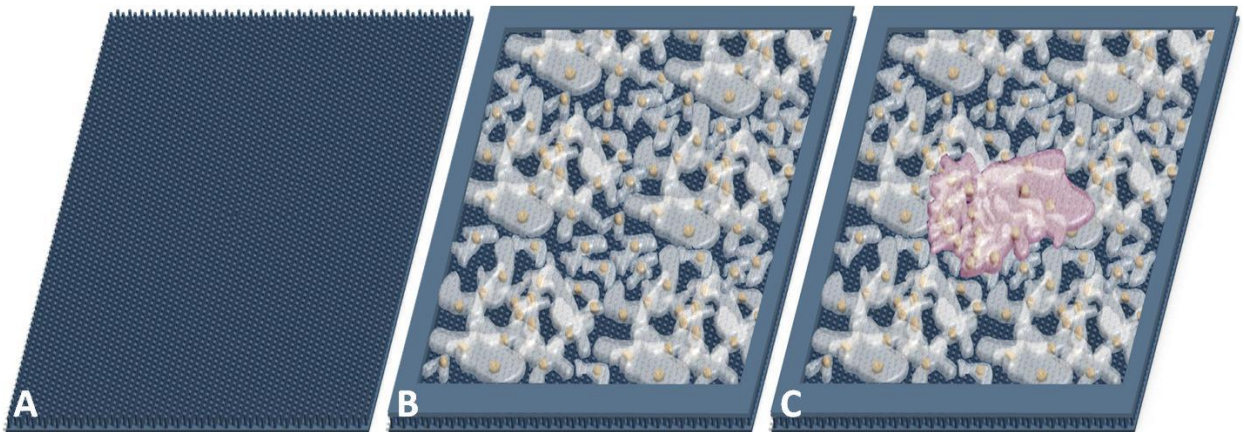

Figure 4.2. Experiments for investigating effects of microtopography on iPSCs.
Reprogrammed cells were seeded on (*A*) *μVRs* and flat PDMS surfaces. To ensure that specific seeding densities were maintained for different substrates, PDMS frames (*B*) were used to confine cell suspensions to 1 x 1 cm^2 areas on all test surfaces. The frames were approximately 4 mm in depth. Effects of microtopography, initial seeding density, and virus infection levels on the (*C*) reprogramming and differentiation of iPSCs (light pink cells) were explored over time.

4.3 Materials and Methods

4.3.1 Micropost Arrays Substrates: Microfabrication and Preparation

Micropost Array Preparation for iPSCs

Micropost array substrates with 7 μm tall features were fabricated in a manner similar to that used in the BAEC single and collective cell studies. Additionally, another set of shorter micropost array substrates (2 μm tall features) was fabricated. Briefly, silicon wafers were cleaned in *msink8*, treated with HMDS in *primeoven*, spin-coated with OiR 897-10i (*Fujifilm, RI, USA*) i-line positive photoresist (*svgcoat2, coater program 5*), and soft baked (*svgcoat2, oven program 2*). Similar to the SPR-220 coated wafers, these wafers were exposed using *gcaws2* with the EXPO EXPO program. For exposure, offset values ranged from -4 to -6, and exposure times were between 0.60-0.62 seconds to pattern features. Following exposure, the wafers were post exposure baked (*svgdev1, oven program 1*) and developed (*svgdev1, developer program 1*). The wafers were then hard baked at 120°C for 20 minutes (*VWR oven*) before being placed in *primeoven* for dehydration and baking. To create a release layer, the wafers were silanized using the same procedure used for the SPR-220 coated wafers. PDMS, mixed at a 1:10 w/w ratio, was poured into these micromolds, and cured under vacuum at room temperature for at least two days before use.

The preparation of the micropost array substrates were identical to the methods used for the BAEC single and collective cell studies. However, to isolate the effects of biophysical cues

on the cells from any chemical effects, the substrates were not microcontact-printed with any proteins following the O_2 plasma-treatment. Additionally, to maintain the surface density of seeded cells between different surfaces, the cell suspensions must be confined to a specific area. To accomplish this, PDMS frames were used, which were flat PDMS sheets (~4 mm thick) with 1 x 1 cm^2 square holes manually cut into them. The PDMS frames were cleaned and sterilized using the same procedures used for the thin-film PDMS stencils in the collective cell studies. Following sterilization, the PDMS frames were dried and placed in contact with the O_2 plasma-treated substrates, surrounding the active area of surfaces and creating small wells to contain the cell suspensions.

4.3.2 Cell Preparation for Collective Cell Migration Studies

Primary Cell Isolation: Mouse Ear Fibroblasts (mERFs)

Mouse ear fibroblasts (mERFs) were isolated from C57BL/6 wild type mice provided by the Xiaohua Gong laboratory (Vision Sciences Division, School of Optometry, UCB). Euthanized mice, 4-8 weeks old, were sprayed until soaked with 70% ethanol to prevent contamination. Mouse ears were harvested by removing them close to the skull with sterilized scissors, and stored in sterile PBS prior to cell isolation. In a sterile environment, after removal of hair using tweezers, ear tissue (from 3-4 mice) was diced with scalpels until a putty-like consistency was achieved. The tissue was then digested in 10 ml of a sterile-filtered solution of 3 mg/ml collagenase IV (*Sigma-Aldrich, MO, USA*) in 0.25% Trypsin, 1x PBS (all *Gibco, Invitrogen, NY, USA*). This mixture was incubated and agitated at 37°C for 30-60 min, or until the mixture was cloudy. DMEM, supplemented with 10% FBS and 1% P/S, was added to neutralize the Trypsin activity. Following manual pipetting to further break apart the tissue, the mixture was centrifuged at 1000 RPM for 4 min. The supernatant was aspirated and the pellet was resuspended in 40 ml of DMEM. The suspension was centrifuged for a second time under the same conditions. After aspiration of the supernatant, the pellet was resuspended in 10 ml of DMEM and transferred to a 10 cm TC dish and placed in an incubator at 37°C with 5% CO_2 and 5% O_2. The dish was checked daily to observe appearance of fibroblasts and changes in media color. Changes in media color can indicate contamination. While fibroblasts should appear within 2-5 days, all viable cells should have exited the tissue after two weeks. The cells were then passaged, grown to 80-90% confluency, and frozen down for future use.

Lentivirus Generation and Infection

An overview of the iPSC reprogramming process can be found in **Figure 4.3**.

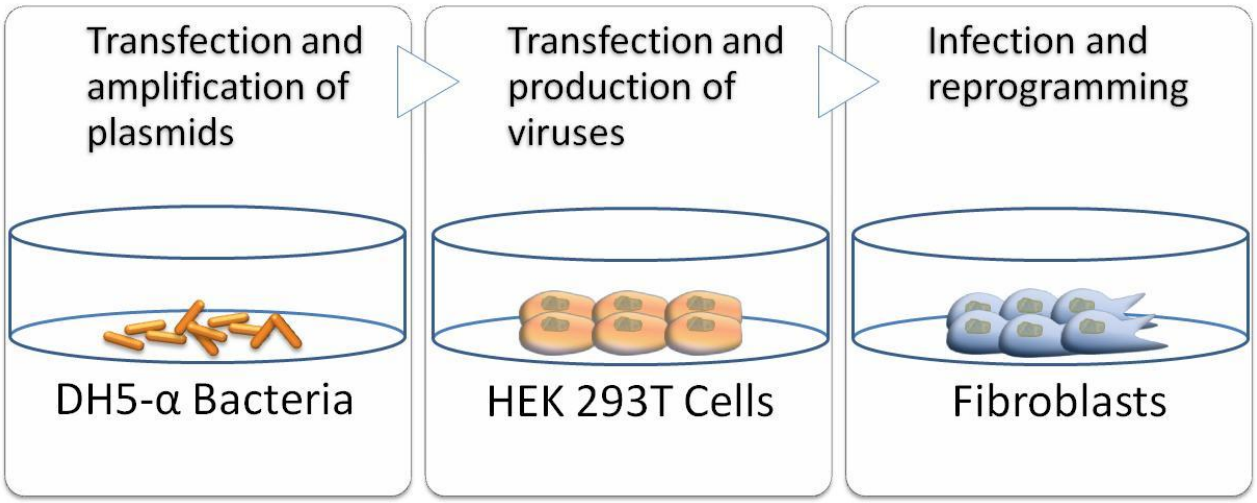

Figure 4.3. Overview of virus production and fibroblast reprogramming.
mERFs were reprogrammed into iPSCs by transfecting them with specific stem cell-associated transcription factors using lentiviruses. To generate lentiviruses for reprogramming cells into iPSCs, DH5-α bacteria were first transfected and used to amplify desired reprogramming and helper plasmids. The plasmids were then extracted from the bacteria by lysing them, and used to transfect HEK 293T cells. The HEK 293T cells subsequently produced viruses for infecting and reprogramming mERFs.

As the first step in this process (**Figure 4.3**-*left*), STEMCCA, the 4-in-1 polycistronic vector (*material transfer agreement with Gustavo Mostoslavsky*) for the original Yamanaka factors, Oct-3/4, Sox2, Klf4, and c-Myc (OSKM), [147] as well as helper plasmids for helper proteins (polyproteins, viral envelope proteins, transactivators, and viral genetic material integrators), Gag/Pol, vesicular stomatitis virus glycoprotein (VSVG), and Rev, (all a gift from the *David Schaffer laboratory*) were amplified by transfecting chemically competent *E. coli*, DH5-α (*Life Technologies, NY, USA*). Following plasmid amplification through DH5-α growth, the bacteria were lysed to harvest the plasmids. The plasmids were then quantified and diluted to get a final concentration of 1 μg/ml. These plasmids can be frozen down to store them for later use. This concentrated DNA was then mixed with sterile DI water, HeBS, $CaCl_2$, NaCl, and NaHPO4 (all from *Thermo Fisher Scientific, Inc., NH, USA*) to reach the desired concentration for experiments of 10 ng/ml, or about 1% of the solution. Relative proportions of the components of this mixture varied depending on the plasmid type.

To generate lentiviruses for reprogramming the mERFs into iPSCs, human embryonic kidney (HEK) 293T cells (gift from the *David Schaffer laboratory*) were used (**Figure 4.3**-*middle*). The HEK 293Ts were maintained in Iscove's Modified Dulbecco's Medium (IMDM), supplemented with 10% FBS and 1% P/S (all from *Gibco, Invitrogen, NY, USA*). Prior to transfection, the media was replaced for the HEK 293T cells plated on 10 cm TC dishes (50-70% confluent) 15 minutes before adding the plasmid mixture to ensure a proper fluidic pH in the system. Following the media change, 2 ml of the plasmid mixture was incubated with the cells

for 14-16 hours. The HEK 293Ts were then washed with sterile PBS and stored in IMDM for 40 hours before harvesting the produced virus. This virus could then be concentrated using Lenti-X Concentrator (*Clontech Laboratories, Inc., CA, USA*) and centrifuging. Once the virus has been concentrated, it can be frozen down for later use. To infect the mERFs for reprogramming, the virus was diluted to the desired concentration and placed on the mERFs for 5-24 hours (**Figure 4.3**-*right*). While virus concentration was never measured for these experiments, a multiplicity of infection (MOI) of 1 was targeted as the baseline level of infection, or "1x". This virus concentration for a 10 cm dish of mERFs was equivalent to the amount of virus produced from the aforementioned 40 hour incubation period of one 10 cm dish of HEK 293Ts. Once infected, these cells were trypsinized and suspended at the desired concentration of 1230 cells/μl in mouse embryonic stem cell (mESC) media. The mESC media is DMEM supplemented with 15% mESC FBS, 1% non-essential amino acids (NEAA), 1% P/S, (all from *Invitrogen, NY, USA*) 0.01% leukemia inhibitory factor (LIF) (*Millipore, MA, USA*), and 0.0008% β-mercaptoethanol (*Sigma-Aldrich, Corp., MO, USA*). To fill the wells created by the PDMS frames, 200 μl of suspension were used, resulting in a density of 246000 cells/cm^2. This density was considered to be approximately 10 times confluency, or "10x". For both level of lentivirus infection and initial seeding density, the variations were multiples of the above concentrations.

4.3.3 Methods for Observing Reprogramming Behavior

The infected mERFs required daily media change and were imaged periodically using phase contrast microscopy with the Eclipse TE300 inverted microscope or the AxioObserver A.10 (*Carl Zeiss Microscopy, LLC, NY, USA*) with AxioVision 4.8.2 software. For fluorescently stained samples, images were taken using the Swept Field Confocal with Prairie View Imaging software (*Prairie Technologies, Inc., WI, USA*), or the ImageXpress® Micro System (*Molecular Devices, LLC, CA, USA*) with a Photometrics CoolSNAP$_{HQ}$ digital charge-coupled device (CCD) camera and MetaXpress 3.1.0.89 software. ImageJ was used for image post-processing and analysis, including measuring areas and fluorescence intensities. All data is presented as means and s.e.m. These were calculated directly from the data and processed using the same statistical methods as used for the single cell studies.

4.4 Results and Discussion

4.4.1 Microfabrication Results

By using the design and microfabrication methods from both the single and collective cell studies, the *μVR$_7$s* were fabricated using SPR-220 and yielded similar results. As SPR-220 cannot be used to make microposts shorter than 5 μm, OiR 897-10i was used to make the *μVR$_2$s*. Fabrication results for microposts with 1.5 μm and 2.5 μm can be found in **Figure 4.4**. The micropost had sidewalls that were slightly angled and flat top surfaces.

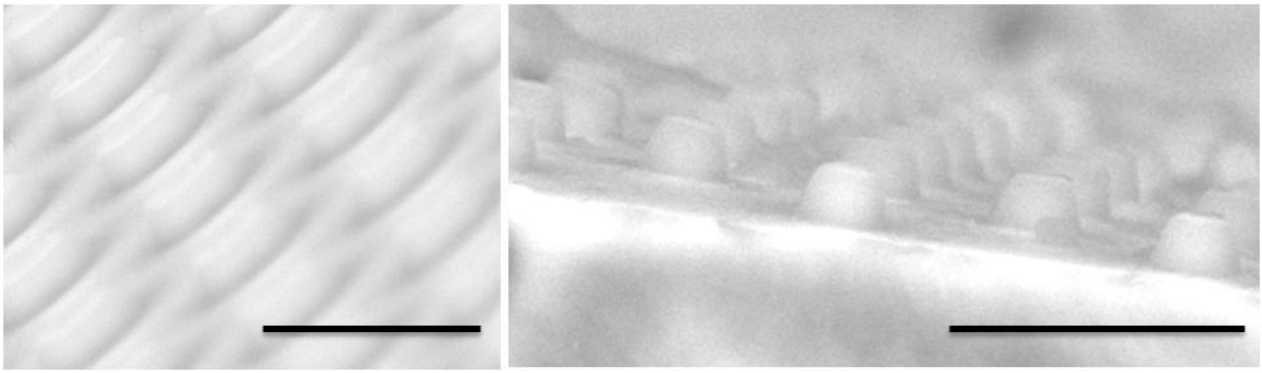

Figure 4.4. *μVR_2* fabrication results.
μVR_2s were fabricated with variable radii and heights to investigate possible effects of microtopographic height on the reprogramming process. Since micropost array substrates with features shorter than 5 μm cannot be made using SPR-220, 2 μm tall microposts were created using OiR 897-10i and standard programs on *svgcoat2*. SEM micrographs of micropost with radii of (*left*) 2.5 μm and (*right*) 1.5 μm. Bars = 10 μm

4.4.2 Effects of Seeding Density on iPSC Colony Formation

The reprogramming process of mERFs was refined and characterized in parallel with the reprogramming experiments. As a result, many factors, such as the initial seeding density of infected mERFs, were found to influence parts of the reprogramming process. For all experiments in this chapter, the reprogramming of mERFs into iPSCs was observed through the formation of iPSC colonies over time. If a mERF has been successfully reprogrammed, it will observe a different morphology that is similar to the rounded appearance of ESCs and self-replicate at a much higher rate than normal mERFs. The high replication rate of the iPSCs results in the formation of individual, dense clusters, which are referred to as colonies. As colonies may merge into one another at later time points, merged colonies will be counted as single colonies as physical and chemical connections may have occurred.

After lentivirus infection, the density at which cells were seeded onto substrates affected the number of colonies that formed. As shown in **Figure 4.5**, mERFs infected with a target MOI of 1 were seeded on TC dishes at densities that were multiples of confluency, 1x, 5x, and 10x. The seeding areas were approximately 1 x 1 cm^2 and confined using the PDMS frames. Time-lapse images of infected mERFs and induced iPSC colony growth can be found in **Figure 4.5.A** for days 2-8. In **Figure 4.5.A**, infected mERFs formed dense monolayers with no colony formation at day 2 for all seeding densities. By day 4, colonies formed on the surfaces with the 1x seeding density, as shown by the cell cluster with different morphology in **Figure 4.5.A**. In contrast, the 5x and 10x samples only had mERF monolayers. However, the 5x and 10x samples yielded many more colonies in comparison to the 1x samples by day 8.

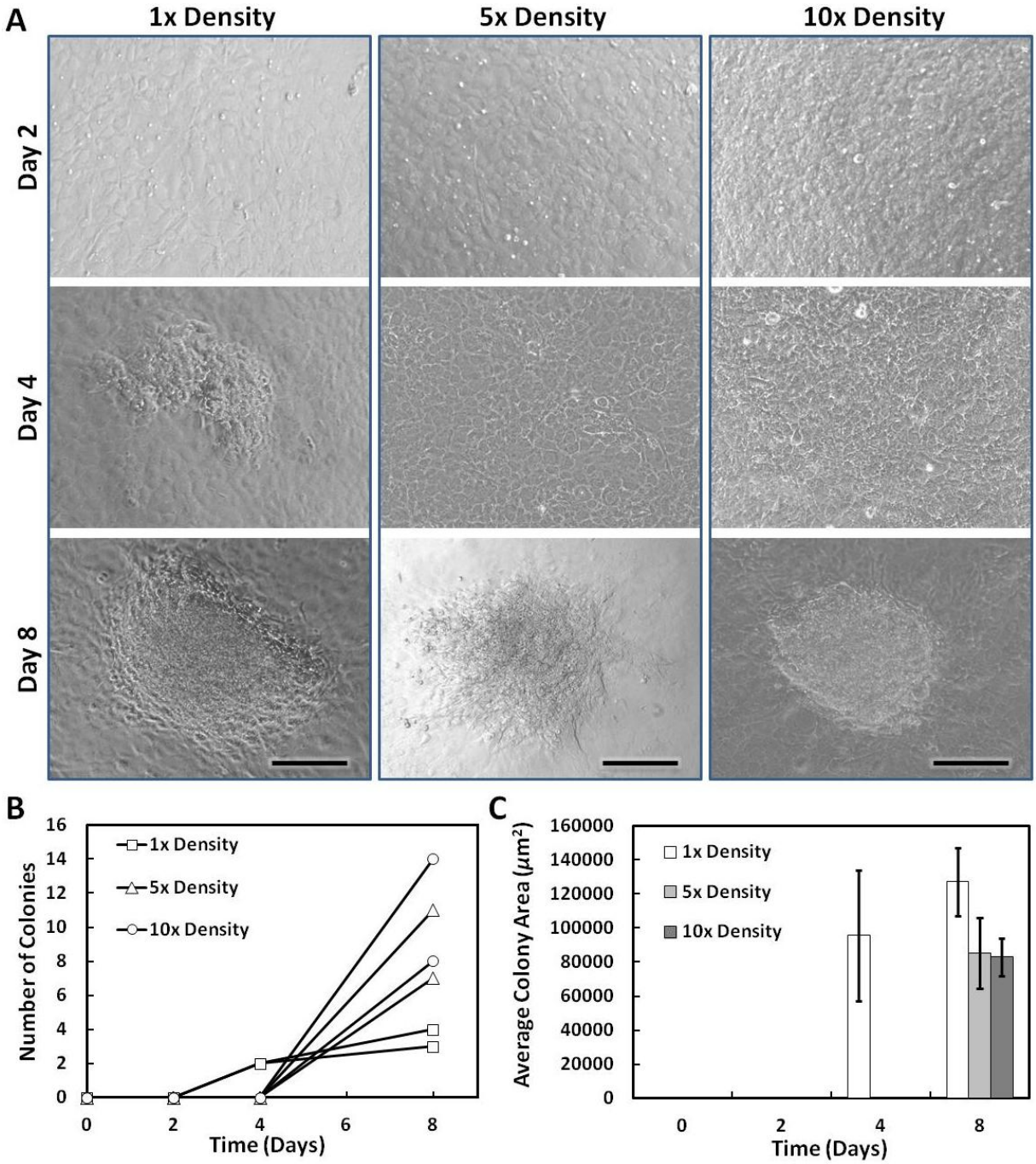

Figure 4.5. Time-lapse images of colony growth for various seeding densities.
After lentiviral infection with a target MOI of 1, mERFs were seeded on TC dishes at densities that were multiples of confluency: 1x, 5x, and 10x. (*A*) Time-lapse images of colony formation for days 2-8 for all seeding densities. Colonies formed earliest for the 1x samples at day 4. However, the 5x and 10x samples formed more colonies by day 8. Bars = 200 μm (*B*) For two samples of each seeding density, the number of colonies was tracked over an 8-day period. The average number of colonies increased with increasing seeding density. (*C*) The average size of the colonies was calculated for all colonies tracked in (*B*). On average, the colonies on the 1x samples were larger than those on the 5x and 10x samples. This difference was not found to be statistically significant.

In **Figure 4.5.B**, the formation of colonies was recorded over time for two samples of each seeding density. While the average number of colonies increased with increasing seeding density, it was not found to be directly proportional. The average number of colonies at day 8 for the 1x, 5x, and 10x samples were 3.5, 9, and 11 colonies/cm^2, respectively. The average area of the colonies was calculated for the different seeding densities, as shown in **Figure 4.5.C**. At day 8, the 1x, 5x, and 10x samples had approximate average colony sizes of 127000 ± 20000 μm^2, 85000 ±20700 μm^2, and 83000 ± 10900 μm^2, respectively. While the colonies for the 1x samples were larger than the ones on the 5x and 10x samples, the differences were not found to be statistically significant.

The proportionality between the numbers of iPSC colonies that form and the initial seeding density is an intuitive result, as increasing the number of cells in a population will increase the likelihood that a reprogrammed cell is present. Additionally, at high seeding densities, cells may be forced to have contact with many other cells and form cell-cell junctions. As E-cadherins have been found to be necessary for the reprogramming of cells and have even been able to replace Oct-4 in the reprogramming process, [168] high seeding densities may also promoted reprogramming through higher expression of E-cadherins.

4.4.2 Effects of Virus Concentration and Microtopography on iPSC Colony Formation

In addition to initial seeding density, experiments indicated that lentivirus infection levels (concentration) and substrate microtopography affected mERF reprogramming. mERFs were infected at three concentration levels, 0.5x, 1x, and 3x. While the virus concentration was never measured, the concentration levels were multiples of a targeted of MOI of 1. As higher initial seeding densities were found to yield more iPSC colonies, a seeding density of 10x confluency was used for all experiments to better visualize the results. Infected mERFs were placed on three surfaces: μVR_2, μVR_7, and flat PDMS. Two samples for each combination of virus concentration and substrate type were observed for their possible effects on the reprogramming process for 21 days.

To investigate the reprogramming of mERFs on these surfaces, immunofluorescence was used in **Figure 4.6**. **Figure 4.6.A-D** were taken at a magnification of 20x to show cellular detail of normal and infected mERFs, while montages of infected mERF images (7 x 7 matrix) taken at 20x magnification were created to visualize entire colonies in **Figure 4.6.E,F**. Normal, non-infected mERFs (**Figure 4.6.A,B**) were used as a control for the reprogramming process. Both normal mERFs and infected mERFs (**Figure 4.6.C-F**) were seeded on $\mu VR_7 s$ and were incubated for 21 days. After 21 days, the infected mERFs were able to yield colonies (**Figure 4.6.C-F**), some of which exhibited beating. In **Figure 4.6.A**, the individual nuclei (DAPI, blue) of the normal mERFs show visible deformation (non-ovular shapes) from the underlying microposts. This deformation was also present in the nuclei of the infected mERFs, but is not visible in **Figure 4.6.C** because of the high density of cells, illustrating an iPSC colony, in the image. By comparing the density of nuclei in **Figure 4.6.A** and **Figure 4.6.C**, the different growth rates of

normal mERFs and iPSCs formed from reprogrammed mERFs were visible as normal mERFs were not able to form colonies of cells.

To determine if the mERFs were actually reprogrammed into a pluripotent state, the normal mERFs and colonies formed by infected mERFs were stained for Oct-3/4 (*Santa Cruz Biotech, CA, USA*) (**Figure 4.6.B,D**). Oct-3/4 is involved in the renewal of undifferentiated stem cells and is used as a stem cell marker. As normal mERFs were not infected, the cultures did not express Oct-3/4, shown by the negative stain in **Figure 4.6.B**. In contrast, the colonies formed by the infected mERFs had positive staining for Oct-3/4, as shown through the bright TRITC (red) fluorescence in **Figure 4.6.D**.

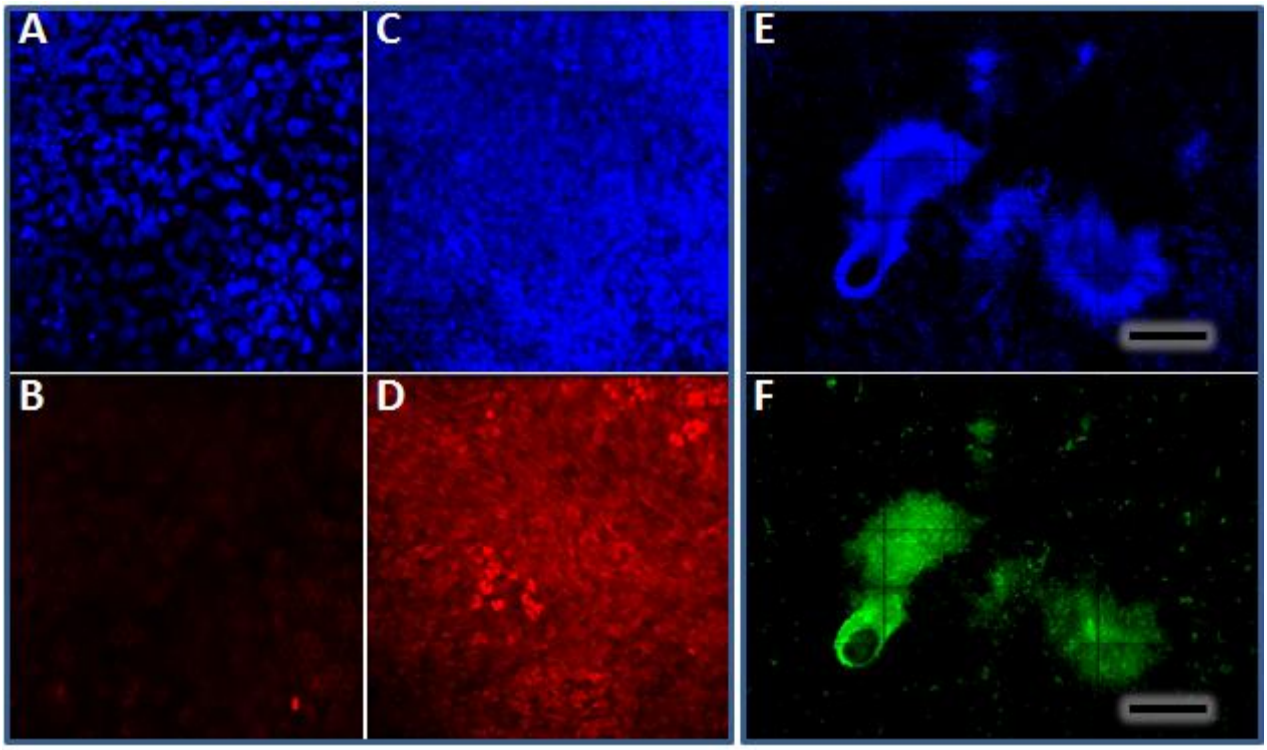

Figure 4.6. Fluorescence images of iPSC colonies.
Normal and infected mERFs were seeded on μVR_7s and stained for Oct-3/4 and Nanog to confirm that the colonies they formed consisted of iPSCs. (*A*) Normal mERFs were stained for nuclei (DAPI, blue) and show nuclear distortion (non-ovular shape) from the underlying microposts (radii = 2 μm). (*C*) In comparison to the relatively sparse nuclei of normal mERFs, the dense appearance of nuclei of infected mERFs shows that colonies of reprogrammed cells could be formed. To determine if these colonies were reprogrammed, both the normal mERFs and colonies formed from infected mERFs were stained for Oct-3/4. (*B*) As shown by the negative staining, normal mERFs were unable to form colonies and did not express Oct-3/4. (*D*) In contrast, colonies formed by reprogrammed mERFs stained positively through bright TRITC (red) expression. Magnification = 20x. As Oct-3/4 was used to reprogram the mERFs and positive staining may not indicate endogenous production, Nanog was also stained to confirm full reprogramming of the cells. For (*E*) and (*F*), montages of images (7 x 7 matrix) taken at 20x magnification were used to visualize entire colonies. (*E*) The location of cells in these colonies can be found using DAPI (blue) staining of their nuclei. (*F*) Colonies stained positive for Nanog (FITC, green) on μVR_7s, indicating reprogramming to pluripotent states. Bars = 1 mm

Although this staining indicated that Oct-3/4 was present in the infected mERFs and not in the normal mERFs, Oct-3/4 was one factors used to reprogram the mERFs through viral integration. Therefore, its presence in reprogrammed mERFs may not indicate endogenous production of the protein and does not show that cells have been fully reprogrammed. To address this issue, a transcription factor that was not used for reprogramming the mERFs, Nanog (*Abcam, MA, USA*), which directs propagation of undifferentiated cells, [132] was also used to identify iPSC colonies. In **Figure 4.6.E**, two large iPSC colonies were visualized by their nuclei (DAPI, blue) in the 7 x 7 montage of images. These two colonies stained positively for Nanog (FITC, green) in **Figure 4.6.F**, indicating that the infected mERFs had been reprogrammed into a pluripotent state.

As there were slight variations in seeding densities and virus concentration, beating colonies were observed in as early as 14-15 days after infection on all surfaces. Although there were multiple radii on the micropost surfaces, beating colonies were formed on all micropost arrays and did not appear to have a bias towards specific radii. The colonies were also often characterized by multiple sections that beat independently of one another, having as many as three asynchronous parts. Beating frequency was in the range of 0.2 Hz to 1 Hz for all substrates. Time-lapse images taken every 2.5 seconds of a beating portion of a colony can be found in **Figure 4.7**. As shown in the images, the upper edge of the round feature deforms as the colony beats, indicated by the black arrows.

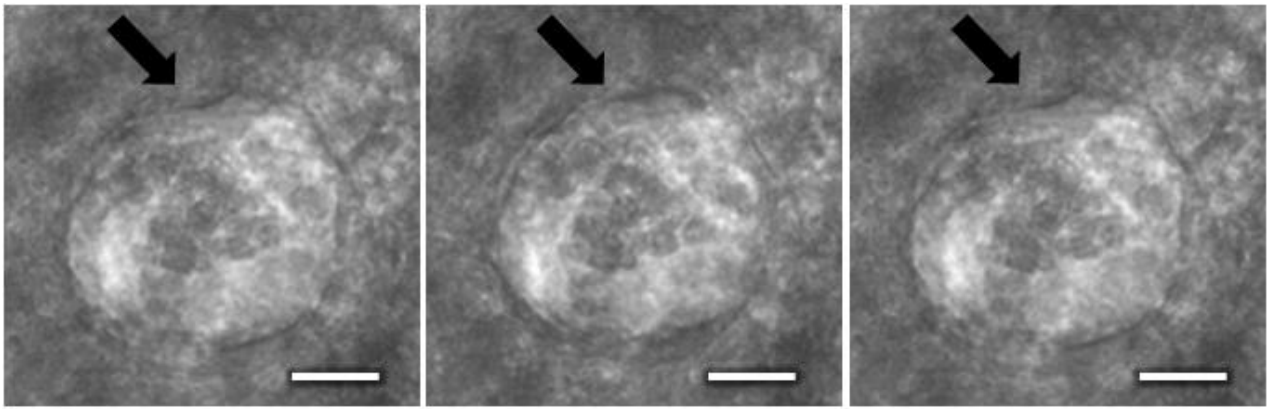

Figure 4.7. Time-lapse images of beating iPSC colony.
Time-lapse images for a beating portion of an iPSC colony, taken every 2.5 seconds. The circular feature shows deformation at the upper edge (black arrows) as the colony beats. Bar = 300 um

Although no beating was observed for normal mERFs cultured on any of the surfaces, both normal mERFs (**Figure 4.8.A,B**) and beating colonies (**Figure 4.8.C,D**) derived from reprogrammed mERFs were stained for Myosin heavy chain (MHC) (*Santa Cruz Biotech, CA, USA*) on μVR_7s after incubating for 21 days. All images in **Figure 4.8** were taken at 20x magnification. As MHC is found in skeletal and cardiac muscle cells and necessary for muscle contraction, it can be used to identify pre-existing cells capable of muscle contraction in normal mERF cultures. Therefore, if normal mERF cultures contain many cells with MHC, then the

beating found in the colonies might not be due to the reprogramming and differentiation of iPSCs. In **Figure 4.8.A**, individual nuclei of normal mERFs (DAPI, blue) were easily seen and show distortion (non-ovular shape) from the μVR_7s with radii of 2 μm. In contrast to the normal mERFs, infected mERFs were able to form colonies, which were visualized through dense populations of cells. The nuclei of cells in a colony formed from infected mERFs can be found in **Figure 4.8.C**. Normal mERFs did not stain positively for MHC (**Figure 4.8.B**), showing low expression of FITC (green) which is likely due to background in the channel. Colonies formed from infected mERFs, on the other hand, show positive expression, with bright FITC (green) staining in **Figure 4.8.D**. These staining results suggest that the normal mERF cultures did not have pre-existing cells that were the source of the beating in the colonies formed by the infected mERFs. The beating, therefore, likely resulted from differentiation of iPSCs.

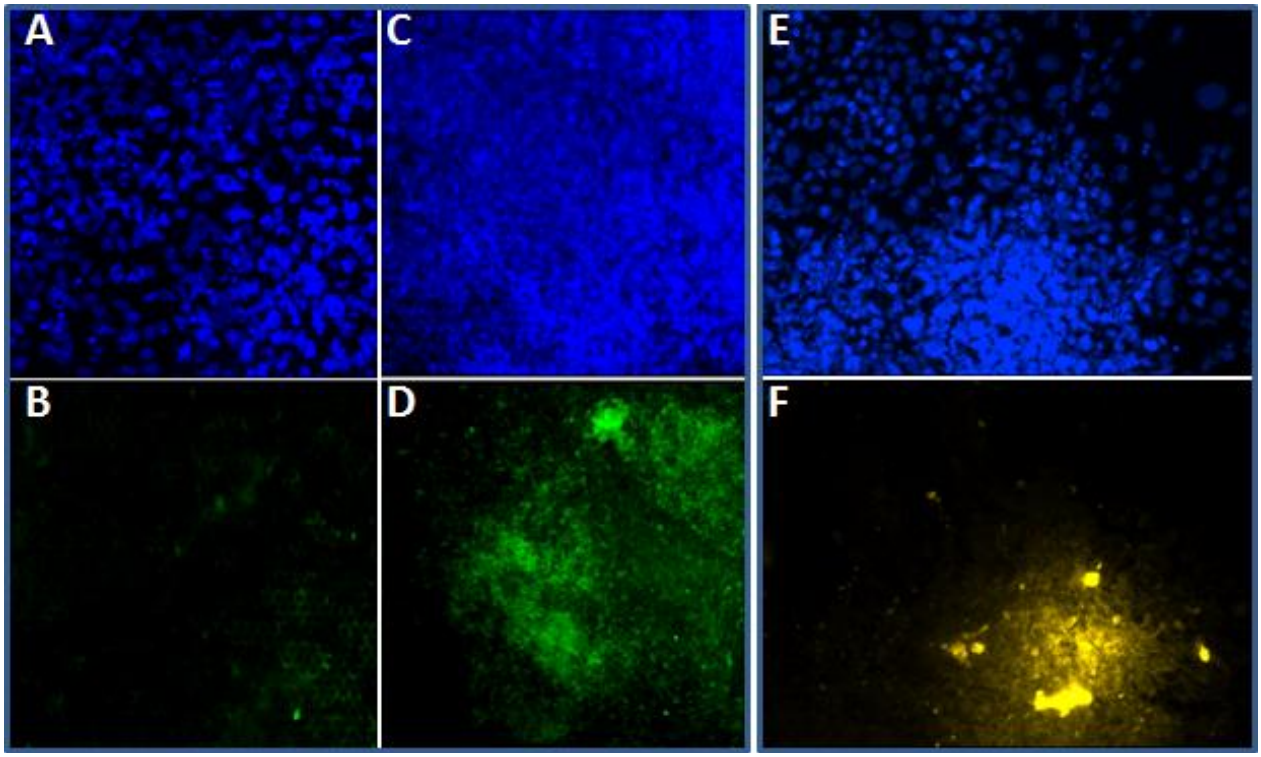

Figure 4.8. Fluorescence images for beating colonies.
Normal mERFs and iPSC colonies on μVR_7s were stained for MHC to determine if pre-existing cells capable of beating were present in the normal mERF cultures and were responsible for beating in the iPSC colonies. (*A*) Normal mERFs were localized using nuclei staining (DAPI, blue), which show distortion (non-ovular shape) due to the underlying μVR_7s with radii of 2 μm. (*C*) In contrast to the relatively low density of the normal mERFs, nuclear staining (DAPI, blue) of a colony formed from reprogrammed mERFs shows high densities of cells. (*B*) Normal mERFs did not express MHC, with low FITC (green) fluorescence likely due to background noise. (*D*) On the other hand, the beating colony formed by the reprogrammed mERFs had portions that stained positively for MHC (FITC, green), suggesting that the beating was a result of differentiation of iPSCs. To further investigate the types of cells that were responsible for the beating exhibited by the iPSC colonies, iPSC colonies were stained for cTnT. (*E*) The nuclei of a beating colony formed from reprogrammed mERFs show a high density of cells. (*F*) This colony had positive expression for cTnT (TRITC, yellow), suggesting that cardiomyocytes were responsible for the beating. Magnification = 20x.

As MHC is found in both skeletal and cardiac muscle cells, to investigate the type of cells responsible for the beating, colonies formed from reprogrammed mERFs were stained for Cardiac Troponin T (cTnT) (*Abcam, MA, USA*). cTnT is more specifically expressed in cardiomyocytes, and positive expression may indicate that they are responsible for the colony beating. In **Figure 4.8.E**, a beating colony formed from reprogrammed mERFs (dense clustering of cells) was visualized with DAPI (blue) staining of the nuclei. This colony stained positively for cTnT with bright TRITC (yellow) expression, as shown in **Figure 4.8.F**. These results suggest that cardiomyocytes are likely responsible for the beating exhibited by iPSC colonies.

The number of colonies formed by infected mERFs was found to increase almost directly with increasing virus concentration. This is expected as higher concentrations of virus particles increase the probability of cells becoming infected and having the ability to reprogram. **Figure 4.9**-*top* shows the number of colonies formed for each sample, each approximately 1 x 1 cm^2 in area. For a virus concentration of 0.5x, the average number of colonies that formed for flat PDMS, μVR_2, and μVR_7 were 2.5, 1.5, and 2.5 colonies, respectively. These numbers increase when the virus concentration was increased to 1x. Flat PDMS surfaces were, on average, able to form almost twice as many colonies as the micropost surfaces. On average, flat PDMS formed 8 colonies, $\mu VR_2 s$ formed 4.5 colonies, and $\mu VR_7 s$ formed 3 colonies. For a virus concentration of 3x, the $\mu VR_2 s$ formed the greatest number of colonies. The average number of colonies formed for flat PDMS, $\mu VR_2 s$, and $\mu VR_7 s$ were 14, 18.5, and 13.5 colonies, respectively. Considering that flat PDMS was able to produce the most number of colonies at the 1x virus concentration, and $\mu VR_2 s$ produced the fewest at the 0.5x concentration and the most at 3x concentration, these results suggest that specific surfaces might be more favorable at different virus concentrations for producing iPSC colonies. As this work includes data from limited prototype testing (two samples per combination), a larger number of tests of the same conditions should be conducted to have statistical figures to reach sound conclusions.

The number of beating colonies was also influenced by increasing virus concentration, though this increase was not directly proportional. The number of beating colonies formed for each sample can be found in **Figure 4.9**-*bottom*. At a virus concentration of 0.5x, flat PDMS, μVR_2, and μVR_7 all formed either 1 or 0 beating colonies. While the number of beating colonies increased on flat PDMS for a virus concentration of 1x, this number actually decreased for the micropost surfaces. On the other hand, the number of beating colonies increased for all surfaces with the 3x virus concentration. The average numbers of beating colonies for the flat PDMS, μVR_2, and μVR_7 were found to be 1.5, 4.5, and 1.5 colonies, respectively. Although the numbers of formed iPSC colonies and beating colonies varied for each sample for each combination of virus concentration and substrate type, it was found that the surfaces that produced the largest number of iPSC colonies also produced the largest percentage of beating colonies. These results suggest that substrate type may play a role in the relative numbers of iPSCs that differentiate into cardiomyocytes for different virus concentrations. Certainly, further investigations with larger numbers of experiments might be able to provide more conclusive trends.

These experimental results confirm that both increasing the initial seeding density and the lentivirus infection concentration of mERFs can increase the number of iPSC colonies that form during the reprogramming process. The influences of substrate microtopography over the number of iPSC colonies that form have been observed but more experiments have to be conducted for conclusive assessments as physical changes in cells due to mechanotransductive responses to microtopography might contribute to the reprogramming processes.

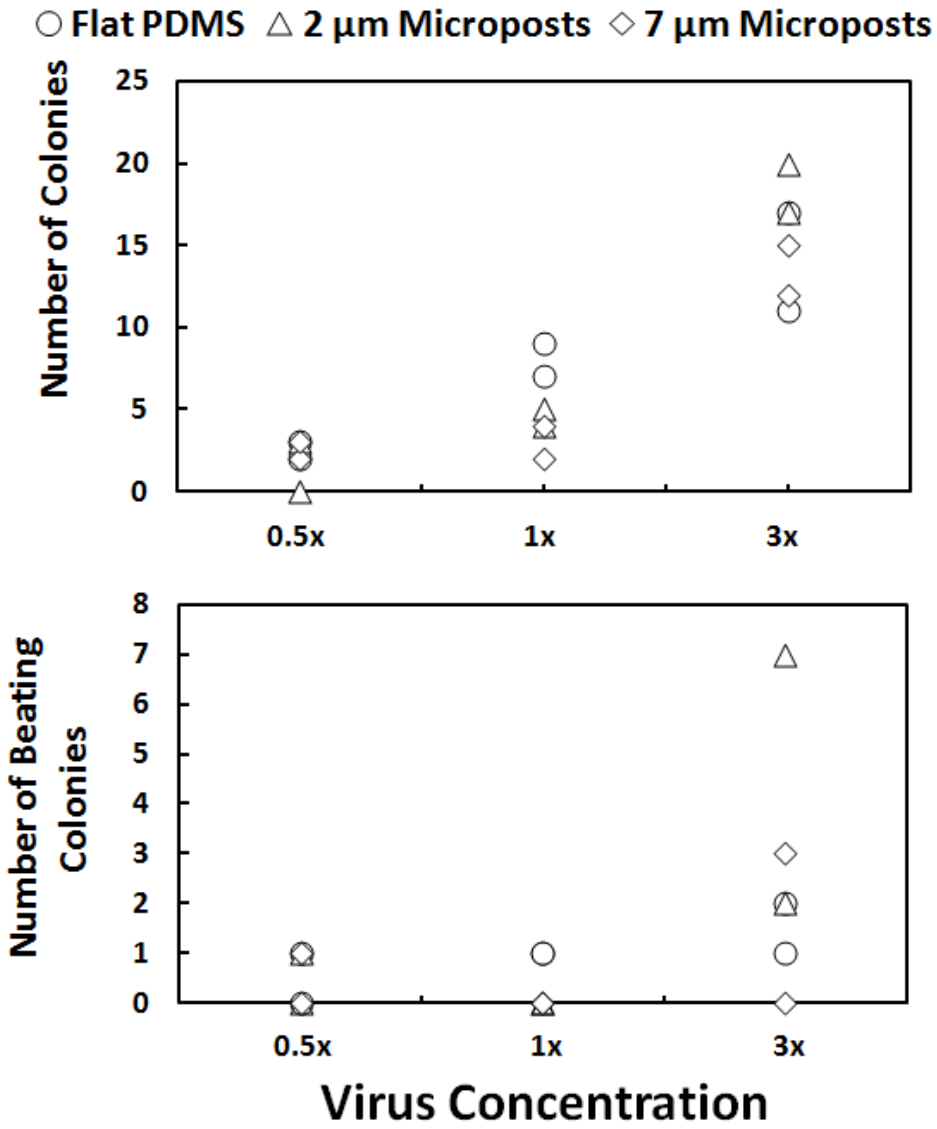

Figure 4.9. Colony formation and beating results.
Colony formation and percentage of beating colonies after 21 days in culture were found to be dependent on virus concentration and substrate type (two samples per combination). (*Top*) The formation of iPSC colonies increased with increasing virus concentration with relative numbers of colonies dependent on substrate type. (*Bottom*) The number of colonies exhibiting beating increased from 0.5x to 3x. Microtopography appeared to affect the relative numbers of beating colonies for each specific virus concentration. These results are for two samples for each combination of substrate type and virus concentration.

Several sets of experiments were subsequently conducted to investigate the appearance of colony beating in these studies, where reprogrammed mERFs on different substrates were observed for the onset of beating. Although the substrates were consistent in these experiments, factors such as sources of cells, cell passage number, and virus incubation periods were varied. Beating was observed in colonies as early as 10 days on the μVR_7s. This result suggests that microtopography might be able to influence the direct differentiation of iPSCs. Previously, only the introduction of chemical factors has been able to achieve directed differentiation of cardiomyocytes within such a short time frame. [178] It should be noted that the inception of beating in the current experiments was difficult to control and could start as late as 20 days after infection, or not at all. Beating was also present on all surfaces, and the onset of beating differed between substrates by, at most, a couple days. As the substrates and initial seeding densities were most consistent between experiments, it is likely that the virus concentration or quality and the source of cells could be the biggest determinants of the onset of beating.

4.4.4 Effects of Microtopography on mERFs

As the previous results indicated that substrate microtopography may affect the formation of iPSC colonies and percentages of beating colonies at specific virus concentrations, effects of microtopography on normal, non-infected mERFs was investigated. These experiments were intended to determine possible physical changes within the cells that may occur on different types of microtopography to give insight on what may be responsible for changes in the reprogramming and differentiation processes of iPSCs. Short-term physical changes that occur in normal mERFs are relevant to these processes as full reprogramming of mERFs into iPSCs can take several days to occur. Experimentally, mERFs were seeded at 0.25x confluency on four types of substrates: TC dishes, flat PDMS, μVR_2s, and μVR_7s. For the micropost arrays, uniform microposts with radii ranging from 1.5 μm to 3μm were tested. mERFs were seeded and incubated on the surfaces for 24 hours and stained for Actin, Lamin A/C, HDAC4 (all from *Santa Cruz Biotech, CA, USA*), and Nesprin (*Abcam, MA, USA*). As one of the most important components of the cytoskeleton, Actin was used to observe the general morphology of the mERFs on different microtopography. To explore how microtopography can influence the structure of the cell nuclei, Lamin A/C and Nesprin expression was studied. Nesprin is responsible for transmitting mechanical information from the cellular microenvironment to the cell nucleus by connecting the cell cytoskeleton to the lamina of the nuclear membrane. The lamina is composed of proteins such as Lamin A/C, and is responsible for maintaining the structural shape of the nucleus through a meshwork of proteins that support the nuclear membrane. In addition to structural differences in the cell and cell nuclei, possible changes in DNA transcription were investigated through HDAC4. HDAC4 can regulate the access of transcription factors to DNA, and its localization in the cell can indicate possible changes in its activity.

After 24 hours, mERFs were stained for nuclei (DAPI, blue), Nesprin (FITC, green), and Actin (TRITC, red) on the TC dishes (**Figure 4.10.A**) and flat PDMS surfaces (**Figure 4.10.B**). The mERFs had ovular nuclei (DAPI, blue) and were well spread out as shown by the Actin (TRITC, red) staining on both surfaces in **Figure 4.10.A,B**. mERFs were also stained for Nesprin (FITC, green), and found to have high expression in their cytoplasms on the TC dishes and flat PDMS surfaces. Overall, mERFs on these two surfaces had similar morphology and expression of the three stains.

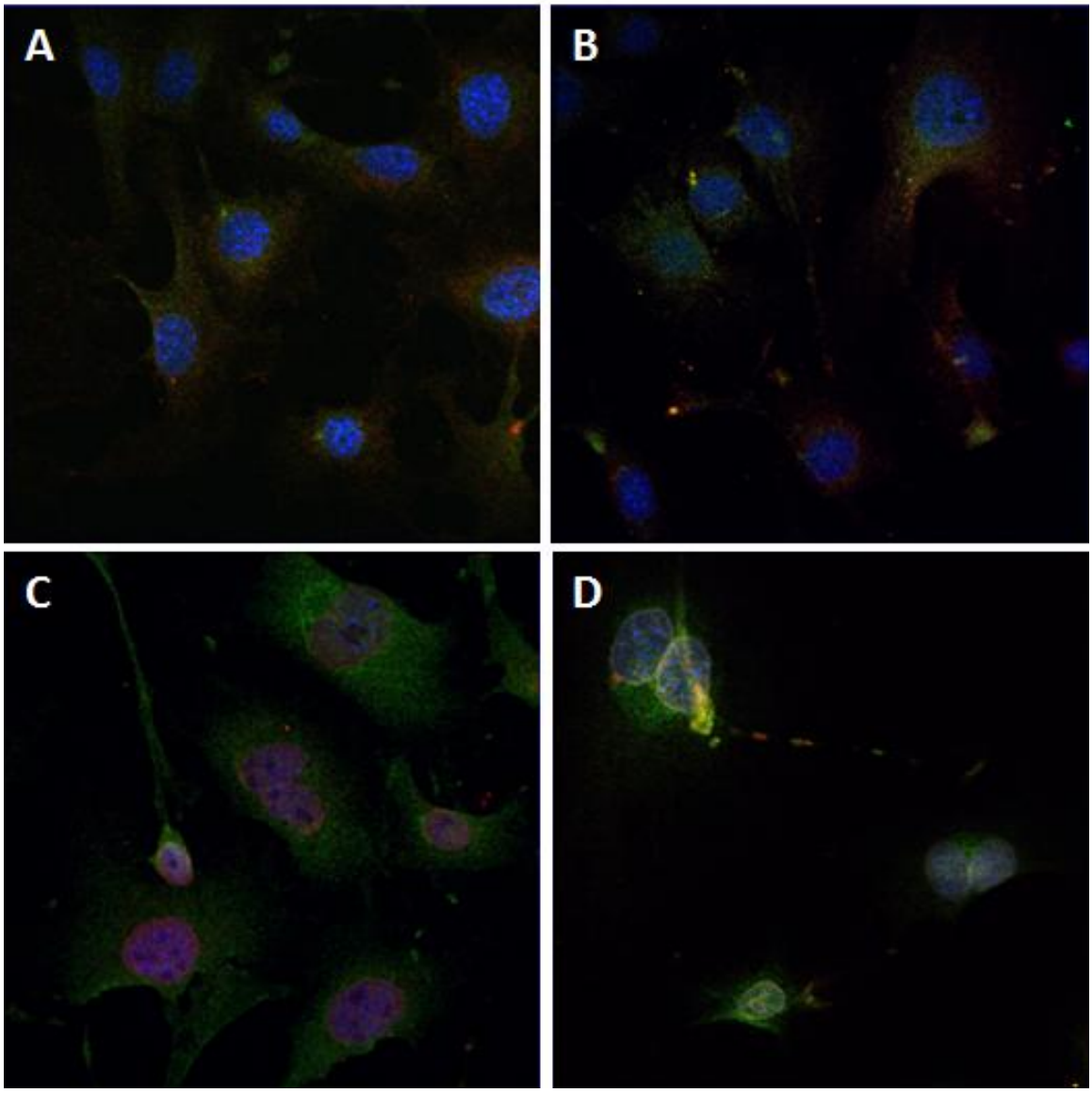

Figure 4.10. Fluorescence images for mERFs on flat PDMS and TC dishes.
mERFs were incubated for 24 hours on (*A,C*) TC dishes and (*B,D*) flat PDMS. (*Top*, *A* and *B*) In addition to nuclei (DAPI, blue), mERFs were stained for Nesprin (FITC, green) and Actin (TRITC, red). Nesprin was found in the cytoplasms for mERFs on TC dishes and flat PDMS. Actin stains illustrate the spread out morphology on both surfaces. (*Bottom, C* and *D*) mERFs were stained for nuclei (DAPI, blue), HDAC4 (FITC, green) and Lamin A/C (TRITC, red). Lamin A/C was found in both the cytoplasms and nuclei of mERFs on the TC dishes and flat PDMS. HDAC4 had high expression in the cell cytoplasms on

the TC dishes, and was mainly confined to the cell nuclei on the flat PDMS substrates. Magnification = 40x.

Additionally, mERFs were stained for nuclei (DAPI, blue), HDAC4 (FITC, green), and Lamin A/C (TRITC, red) on TC dishes (**Figure 4.10.C**) and flat PDMS surfaces (**Figure 4.10.D**). Similar to **Figure 4.10.A,B**, nuclei (DAPI, blue) were ovular on both surfaces, and cells had a spread out morphology. As shown in **Figure 4.10.C**, mERFs on TC dishes exhibited high cytoplasmic content of HDAC4 (FITC, green), while the protein appeared to be mainly confined to the nuclei on the flat PDMS surfaces (**Figure 4.10.D**). On both surfaces, the Lamin A/C stain (TRITC, red) had visually distinct nuclei and some expression in the mERF cytoplasms.

Figure 4.11 and **Figure 4.12** show the staining results for mERFs incubated on μVR_2s for 24 hours. In **Figure 4.11.A-D**, mERFs on μVR_2s with radii ranging from 1.5-3.0 μm were stained for nuclei (DAPI, blue), Nesprin (FITC, green), and Actin (TRITC, red). From the Actin (TRITC, red) staining, the morphologies of the mERFs appeared to be slightly affected by the microtopography, particularly for the microposts with radii of 2 μm and 3 μm, as shown in **Figure 4.11.B** and **Figure 4.11.D**, respectively. In **Figure 4.11.B**, the mERFs appear to be smaller and less spread out, while in **Figure 4.11.D**, the cells appear to be somewhat aligned to the underlying microposts. Overall, mERFs on these surfaces appeared to have smaller spreading areas and thinner protrusions than those on the TC dishes and flat PDMS surfaces. mERFs seeded on the μVR_2s with radii of 1.5 μm (**Figure 4.11.A**) and 2.5 μm (**Figure 4.11.C**), in contrast, had similar morphologies to cells on the flat surfaces. These cells were well spread out, but had thinner protrusions in comparison to the flat surfaces. mERFs on the μVR_2s had slightly irregularly shaped nuclei resulting from interaction with the underlying microposts for all radii. Similar to the flat surfaces, mERFs on the micropost arrays had high expression of Nesprin (FITC, green) in the cytoplasms and appeared to have significant overlap with Actin for all radii.

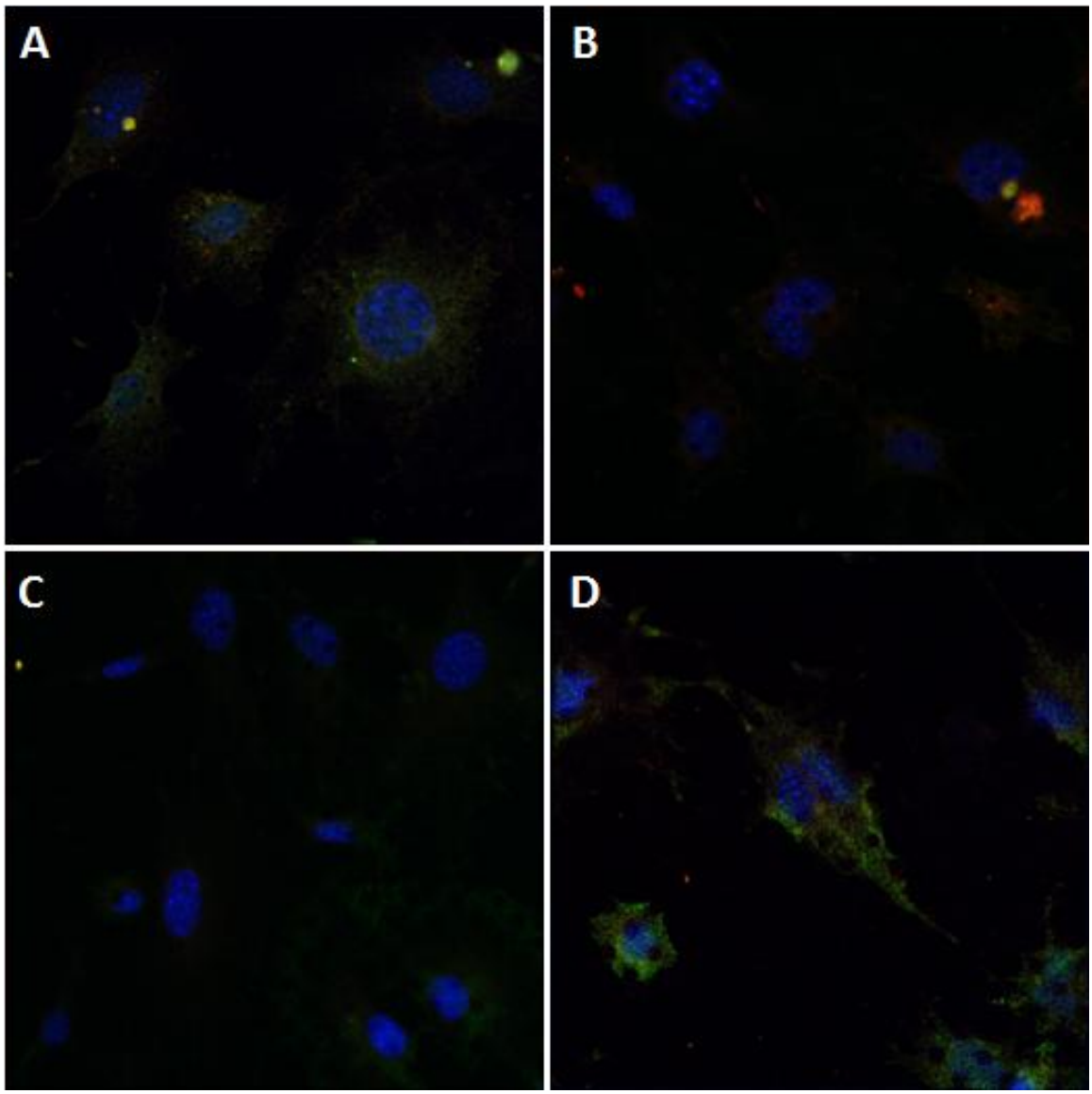

Figure 4.11. Fluorescence images for mERFs on μVR_2s: Nesprin and Actin.
mERFs were incubated for 24 hours on μVR_2s with radii of (*A*) 1.5 μm, (*B*) 2.0 μm, (*C*) 2.5 μm, and (*D*) 3.0 μm. The cells were stained for nuclei (DAPI, blue), Nesprin (FITC, green), and Actin (TRITC, red). The nuclei on these surfaces were generally ovular, with some distortion due to the underlying microposts. From the Actin staining, mERFs were spread out on (*A*) and (*C*), similar to the morphologies observed on TC dishes and flat PDMS. In contrast, mERFs on (*B*) and (*D*) exhibited smaller spreading areas and thinner protrusions. Nesprin was found to be highly cytoplasmic, with large amounts of overlap with Actin for all radii. Magnification = 40x.

In **Figure 4.12**, mERFs on μVR_2s with radii ranging from 1.5-3.0 μm were stained for nuclei (DAPI, blue), HDAC4 (FITC, green), and Lamin A/C (TRITC, red). Similar to the mERFs in **Figure 4.11** and on the flat surfaces, the nuclei (DAPI, blue) were generally ovular. Slight distortion in the nuclei was visible in some mERFs, such as those on the left in **Figure 4.12.A**. This distortion was due to the microtopography, as the nuclei show conformation to the

edges of microposts. For all radii, HDAC4 (FITC, green) was present in the cytoplasms of mERFs with some visible confinement to the nuclei, with the visually highest cytoplasmic expression for the μVR_2s with radii of 1.5 μm (**Figure 4.12.A**) and 2.5 μm (**Figure 4.12.C**). The μVR_2s with radii of 2 μm were the exception (**Figure 4.12.B**), where outlines of the nuclei could not be seen in the HDAC4 stain. The nuclei and cytoplasms were both highly visualized with Lamin A/C (TRITC, red) for all radii.

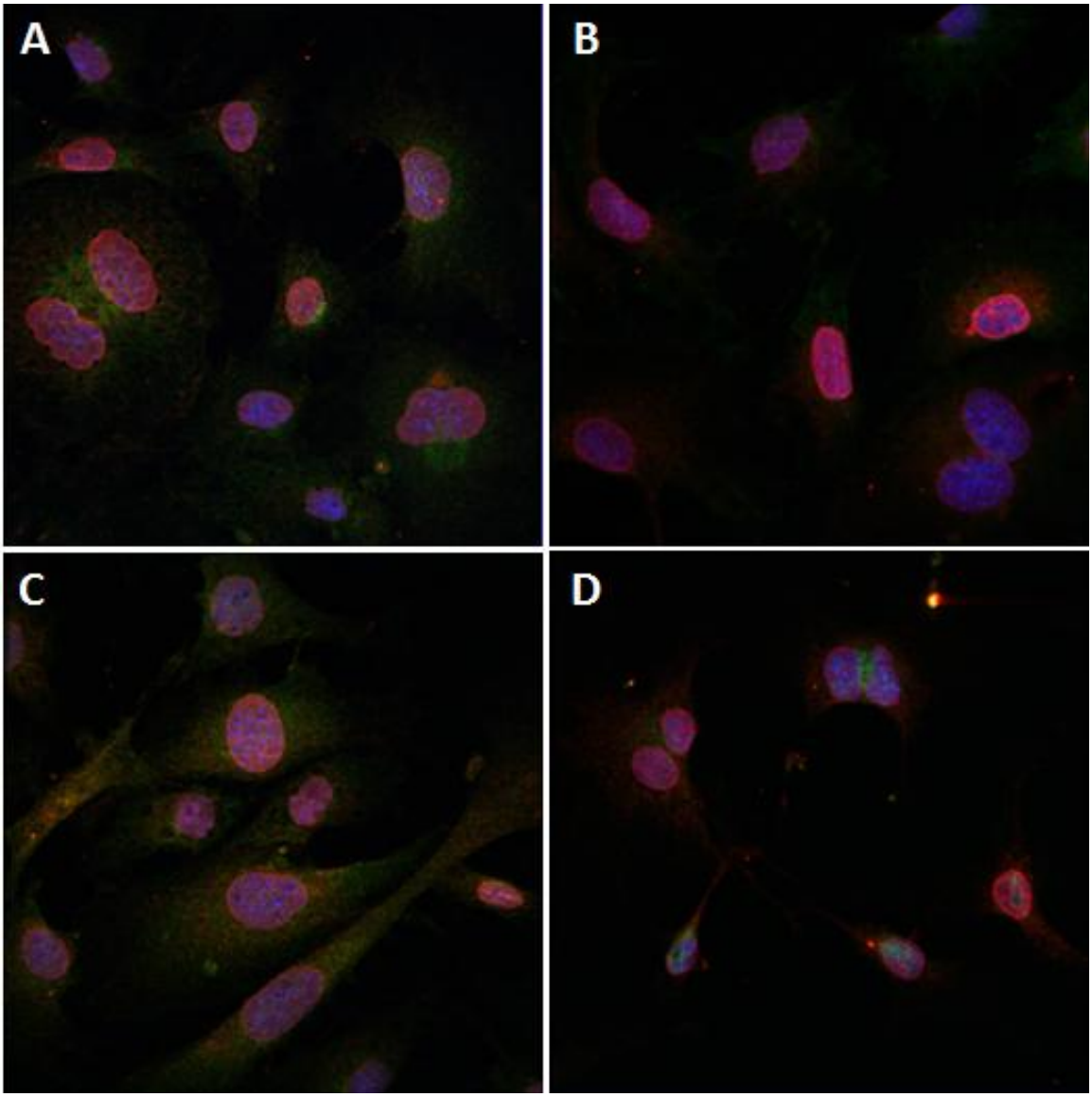

Figure 4.12. Fluorescence images for mERFs on μVR_2: HDAC4 and Lamin A/C.
mERFs were incubated for 24 hours on μVR_2s with radii of (*A*) 1.5 μm, (*B*) 2.0 μm, (*C*) 2.5 μm, and (*D*) 3.0 μm. The cells were stained for nuclei (DAPI, blue), HDAC4 (FITC, green), and Lamin A/C (TRITC, red). The nuclei were generally ovular for all surfaces, similar to the ones in mERFs seeded on TC dishes and flat PDMS. However, some nuclear distortion is visible in mERFs on the left in (*A*), where the nuclei conform to the underlying microposts. HDAC4 was expressed in mERF cytoplasms for all surfaces and visualized in the nuclei for all radii except for the μVR_2s with radii of 2 μm (*B*). Lamin A/C was found in both cytoplasms and nuclei of mERFs on all μVR_2s. Magnification = 40x.

In contrast to both TC dishes, flat PDMS surfaces, and the μVR_2s, mERFs on μVR_7s with radii ranging from 1.5-3.0 μm appeared to be highly affected by the surface microtopography (**Figure 4.13** and **Figure 4.14**) after 24-hour incubation periods.

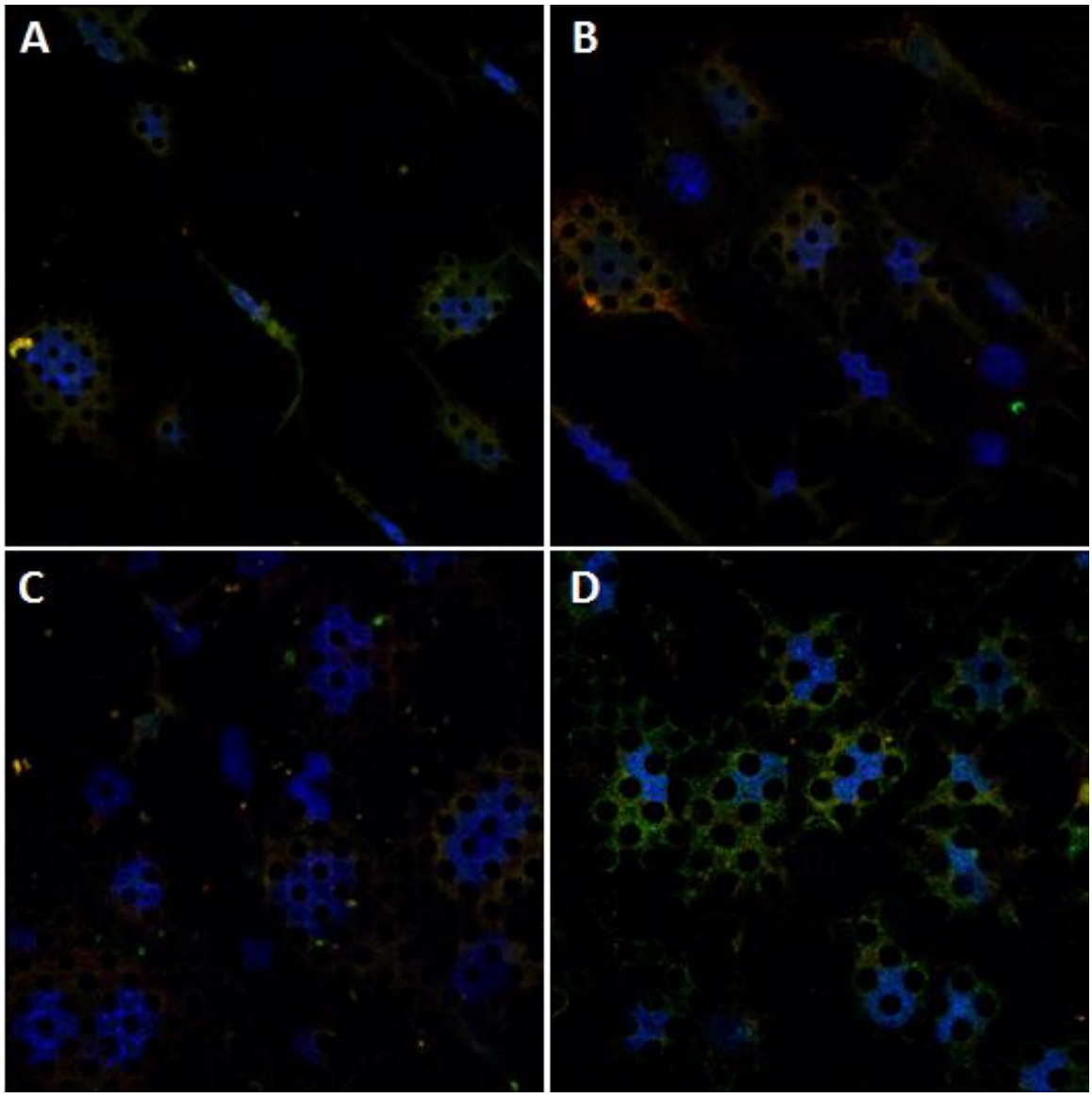

Figure 4.13. Fluorescence images for mERFs on μVR_7: Nesprin and Actin.
mERFs were incubated for 24 hours on μVR_7s with radii of (*A*) 1.5 μm, (*B*) 2.0 μm, (*C*) 2.5 μm, and (*D*) 3.0 μm. The cells were stained for nuclei (DAPI, blue), Nesprin (FITC, green), and Actin (TRITC, red). The nuclei of the mERFs on all surfaces showed significant distortion, with shapes that conformed dramatically to the underlying microtopography. The edges of the microposts can be seen in the nuclear staining. From the Actin staining, mERFs demonstrated morpholgies very different from the TC dishes, flat PDMS, and μVR_2s. In addition to smaller overall spreading areas, mERFs on the μVR_7s exhibited alignment with the microposts, which was very evident in (*A*) and (*B*). mERFs on the larger microposts (*C*) and (*D*) had morphologies more similar to the flat surfaces and the μVR_2s, but had smaller spreading areas as well. For all radii, Nesprin had high cytoplasmic expression, with substantial overlap with Actin. Magnification = 40x.

In **Figure 4.13**, mERFs were stained for nuclei (DAPI, blue), Nesprin (FITC, green), and Actin (TRITC, red). From the Actin staining (TRITC, red), mERFs exhibited very different morphologies for those seeded on the flat surfaces and μVR_2s, with visually smaller spreading areas, alignment with the underlying microposts, and dramatically distorted nuclei. The underlying microtopography was visible for all images in **Figure 4.13**. The majority of nuclei (DAPI, blue) on all μVR_7s were not ovular and molded to the shape of surrounding microposts. The alignment of the cells with the microtopographic features was especially evident for the μVR_7s with radii of 1.5-2.5 μm (**Figure 4.13.A,B** and **Figure 4.14.A-C**). The cells on these surfaces exhibited small spreading areas, aligned along the lines of spacing between microposts, and had long, thin protrusions. mERFs on the microposts with radii of 3 μm, in contrast, had larger spreading areas (**Figure 4.13.D** and **Figure 4.14.D**) more similar to the flat surfaces and μVR_2s. Similar to the other surfaces, mERFs on the μVR_7s had high cytoplasmic expression of Nesprin (FITC, green) for all radii and had significant overlap with Actin, as shown in **Figure 4.13**.

In **Figure 4.14**, mERFs seeded on μVR_7s with radii ranging from 1.5-3.0 μm were stained for nuclei (DAPI, blue), HDAC4 (FITC, green), and Lamin A/C (TRITC, red). Similar to nuclear stains shown in **Figure 4.13**, the nuclei (DAPI, blue) for all surfaces exhibited significant deformation, as outlines of the microposts can be readily visualized in the nuclear areas. For all radii, HDAC4 (FITC, green) was found to be highly cytoplasmic for the mERFs, with visual confinement to the nucleus only present in the μVR_7s with radii of 1.5 μm (**Figure 4.14.A**). For the Lamin A/C (TRITC, red) stain, the mERFs showed visible confinement of the protein to the nuclei with some expression in the cytoplasm on all surfaces.

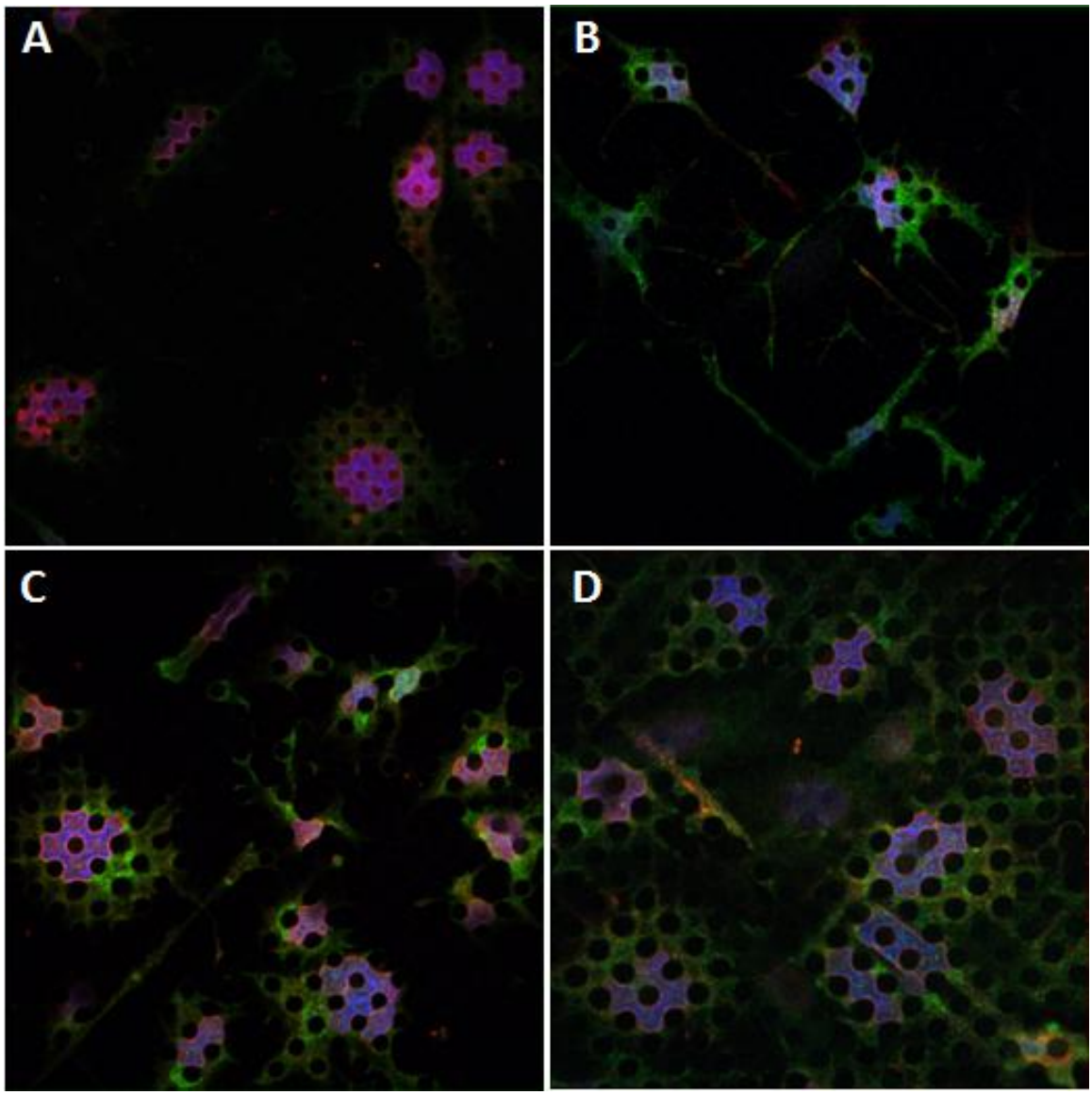

Figure 4.14. Fluorescence images for mERFs on μVR_7s: HDAC4 and Lamin A/C.
mERFs were incubated for 24 hours on μVR_7s with radii of (*A*) 1.5 μm, (*B*) 2.0 μm, (*C*) 2.5 μm, and (*D*) 3.0 μm. The cells were stained for nuclei (DAPI, blue), HDAC4 (FITC, green), and Lamin A/C (TRITC, red). Similar to the nuclear stains in **Figure 4.13**, mERF nuclei were highly distorted with conformation to the underlying microtopography. mERFs had high expression of HDAC4 in their cytoplasms for all radii, with nuclei visualization for only the μVR_7s with radii of 1.5 μm (*A*). Lamin A/C was expressed in both the nuclei and cytoplasms of mERFs for all surfaces. Magnification = 40x.

HDAC4 is part of a class of proteins that are capable of regulating the expression of genes by enabling or limiting transcription factor access to DNA. [193–195] Its activity is modulated through a dynamic nucleo-cytoplasmic shuttling process in the cell. If HDAC4 is present in the nucleus, it is able to regulate the transcription of DNA. However, if it is shuttled out into the cytoplasm, its regulatory behavior is suppressed. As HDAC4 had different localizations in mERFs on the different surfaces, microtopography may play a role in regulating

HDAC4 activity. To better visualize the localization of HDAC4 on the TC dishes, flat PDMS, μVR_2s, and μVR_7s, the single HDAC4 stains are shown in **Figure 4.15**.

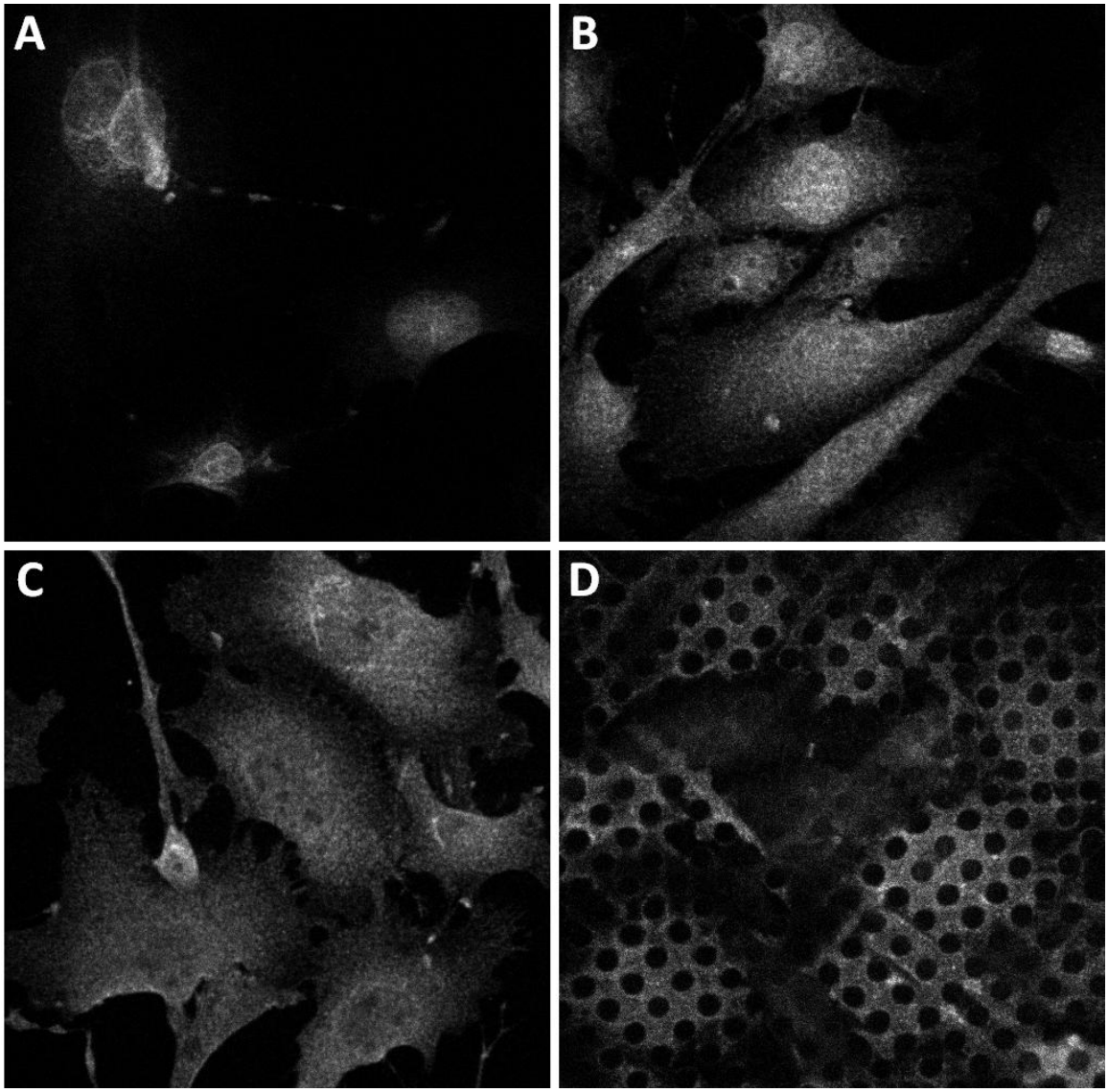

Figure 4.15. Fluorescence images for mERFs on TC dishes, flat PDMS, and *μVRs*: HDAC4
HDAC4 localized in different intracellular locations of mERFs on surfaces with different microtopographies. (*A*) HDAC4 was mostly localized in the nuclei on flat PDMS surfaces, as denoted by the bright nuclear outlines and low expression of HDAC4 in the mERF cytoplasms. (*B*) On the μVR_2s, HDAC4 was found in both the nuclei and cytoplasms, as the general morphology of the mERFs were visualized in this staining. This particular μVR_2 has microposts with radii of 2.5 μm. For the TC dishes (*C*) and μVR_7s (*D*), HDAC4 was highly expressed in the cytoplasms with faint or non-existent localization in the nuclei. Nuclear outlines are particularly difficult to see for the μVR_7s as the staining is interrupted by the underlying microposts. The featured μVR_7s has radii of 3 μm. Magnification = 40x.

As shown in **Figure 4.15.A**, the expression of HDAC4 on the flat PDMS substrates was mostly confined to the nuclei, with faint localization in the mERF cytoplasms. This is likely

indicative that these surfaces do not disrupt the activity of the protein significantly. The cytoplasmic content was increased relative to the flat PDMS substrates for mERFs seeded on the μVR_2s, where HDAC4 was expressed strongly in both locations. **Figure 4.15.B** illustrates this localization in both the nuclei and cytoplasm for the μVR_2s with radii of 2.5 μm. The μVR_2s appear to initiate shuttling of HDAC4 to the cytoplasm, possibly indicating a reduction in its activity in the cell nuclei. For the TC dishes (**Figure 4.15.C**) and the μVR_7 (**Figure 4.15.D**), HDAC4 was highly cytoplasmic with slight localization in the nuclei which is indicated by the faint or non-existent outlines of the nuclei in this stain. **Figure 4.15.D** shows high cytoplasmic expression for μVR_7s with radii of 3 μm, and any nuclear localization is difficult to see as the underlying microposts interrupt the fluorescence staining. This large shuttling of HDAC4 out of the mERF nuclei suggests that these surfaces significantly suppressed HDAC4 activity in the nuclei.

To provide a numerical comparison of protein expression between surfaces, average fluorescence values were measured for each substrate. Fluorescence values for HDAC4 and Lamin A/C (**Figure 4.16**-*top*), and Nesprin and Actin (**Figure 4.16**-*bottom*) were measured. By using confocal images, fluorescence data was collected from image planes with the best staining focus for each substrate using ImageJ. Fluorescence values were collected from the brightest areas of mERFs for each stain. To ensure intensity accuracy, fluorescence values were measured for only the mERFs that were in focus for the specific image plane.

As shown in **Figure 4.16**-*top*, the TC dishes had statistically higher expression of both HDAC4 and Lamin A/C than any of the other surfaces, suggesting that surface chemistry or stiffness might play a role in the expression of both proteins. For HDAC4, expression on the flat PDMS surfaces was similar to the μVR_2s with radii of 2-2.5 μm and the μVR_7s with a radius of 1.5 μm, and higher than all other surfaces. Both the μVR_2s and μVR_7s had similar high and low expressions of HDAC4, with no clear trend for any of the radii. In contrast, the TC dishes, flat PDMS surfaces, and μVR_2s had higher relative intensities of Lamin A/C in comparison to HDAC4. This trend was reversed for the μVR_7s, where the relative intensity of Lamin A/C was lower than HDAC4 on these surfaces. In fact, the expression of Lamin A/C on the μVR_2s was statistically higher than the μVR_7s for corresponding radii.

As Lamin A/C is integral for mechanically stabilizing the nucleus through a protein meshwork underlying the inner nuclear membrane, [196–198] it should have strong expression at the periphery of the mERF nuclei. Lamin A/C was found at the outer edges of the nuclei on all surfaces. As shown in **Figure 4.16**-*top*, on the μVR_7s, the intensity of Lamin A/C was reduced relative to the TC dishes, flat PDMS substrates, and μVR_2s. This makes sense as the nuclei of the mERFs on the μVR_7s were highly distorted (**Figure 4.13** and **Figure 4.14**) in comparison to the ovular nuclei found on the other surfaces (**Figure 4.10**-**Figure 4.12**). Lower expression of Lamin A/C in the μVR_7s may indicate protein disruption at the nuclear envelope and lower nuclear rigidity, which would enable the nuclei of mERFs on these surfaces to conform to the edges of the underlying microposts.

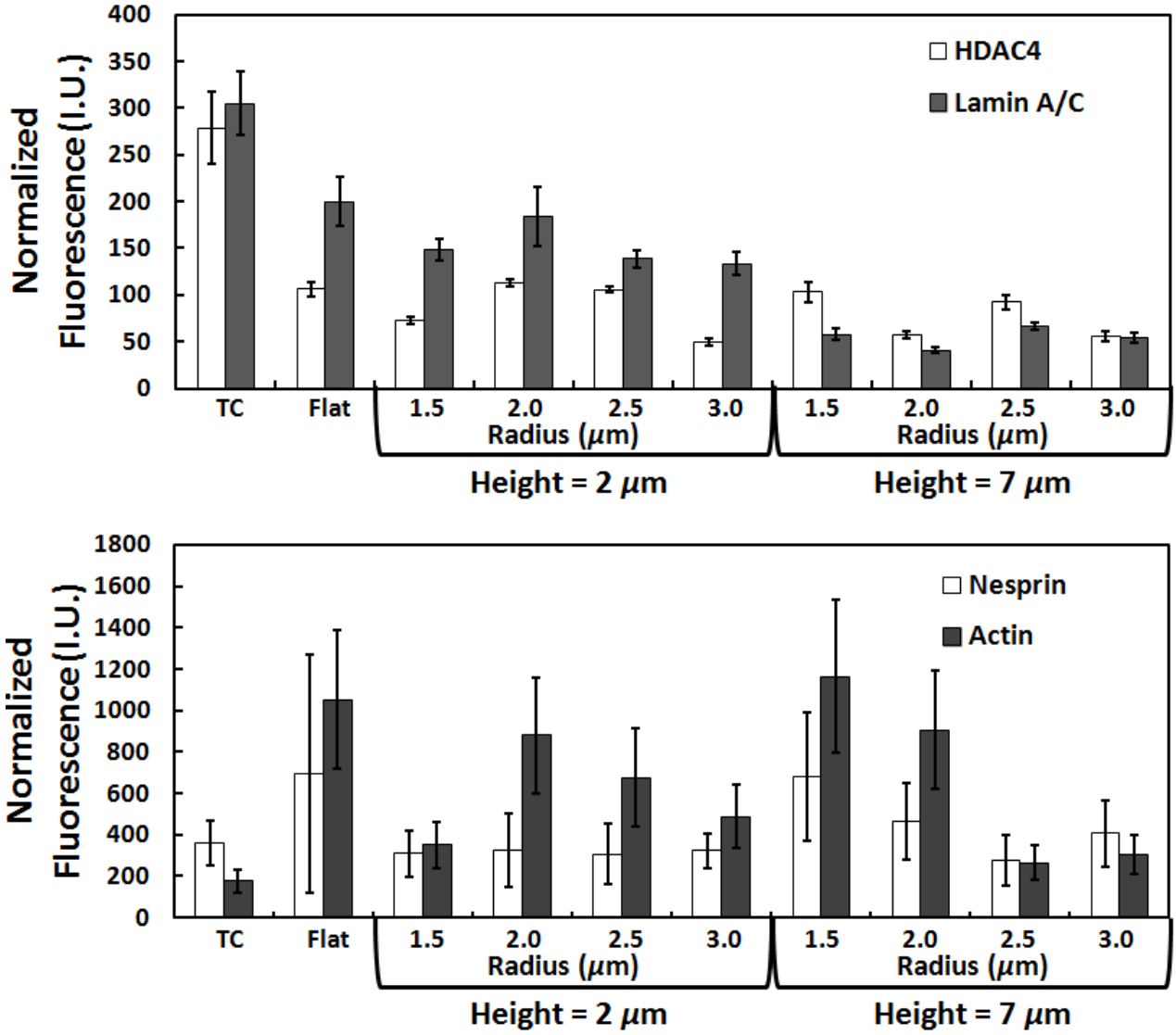

Figure 4.16. Normalized fluorescence results.
To numerically compare the expression of (*top*) HDAC4 and Lamin A/C and (*bottom*) Nesprin and Actin for different surfaces, the normalized average fluorescence intensities were measured for TC dishes, flat PDMS substrates, and the *μVRs*. (*Top*) For HDAC4 and Lamin A/C, TC dishes had the highest expression, with values that were statistically greater than all other surfaces. HDAC4 did not show any trends for the flat PDMS surfaces or the *μVRs*. In contrast, the expression of Lamin A/C was relatively higher than HDAC4 for the flat PDMS substrates and μVR_2s. This trend reversed for the μVR_7s, where the expression for Lamin A/C was not only relatively lower than HDAC4, but also statistically lower than the μVR_2s of corresponding radii. (*Bottom*) The overall intensity values were higher for this set of fluorescence values due to the use of different microscopes for imaging. For Nesprin, expression was similar among all of the surfaces. Actin had higher intensities relative to Nesprin for most of the surfaces, and had similar high and low expressions for both *μVRs*. Error bars = s.e.m.

The average fluorescence values were also calculated for Nesprin and Actin (**Figure 4.16**-*bottom*). These values were much higher than those calculated for Lamin A/C and HDAC4 due to the different microscopes used for imaging. For Nesprin, TC dishes had similar intensities to all other surfaces, differing only from the μVR_7 with radii of 1.5 μm. The expression of Nesprin on flat PDMS surfaces was found to be statistically the same as all of the other surfaces. Although the $\mu VR_7 s$ generally had higher average intensities than the $\mu VR_2 s$, only the μVRs with radii of 1.5 μm had statistically different expressions for Nesprin. In general, Actin expression was higher relative to Nesprin expression. TC dishes had the lowest Actin intensity, with expression that was statistically lower than all other surfaces. Actin expression was high on the flat PDMS surfaces, with expression similar to the μVR_2 with radii of 2.5 μm and μVR_7 with radii of 2 μm. Both μVRs had high and low expression of Actin, with statistical differences for the 1.5 μm and 2.5 μm radii. Overall, no clear trends were found for Nesprin or Actin on the different substrates.

Nesprin, which is responsible for linking the cytoskeleton to SUN proteins that are attached to the lamina of the nucleus, [199–201] should be localized near the outer edge of the nuclei. For all substrates, the nuclei of the mERFs were not visualized in this stain and Nesprin was highly cytoplasmic, with significant overlap with Actin. This suggests that the antibody used for these stains was not specific for this cell type.

The aforementioned structural and DNA transcription changes that result from differences in substrate microtopography give insight into the mechanotransductive pathways that may influence the reprogramming and differentiation of iPSCs. Understanding how biophysical cues can possibly affect these processes will be integral for the implementation of iPSCs in tissue engineering and regeneration, as microenvironmental cues must work synergistically for a common goal.

Chapter 5: Conclusion and Future Work

Micropost arrays provide a robust methodology for controlling the biophysical stimuli within the cellular microenvironment. Through simple and repeatable soft-lithography microfabrication processes, the characteristics of the cellular substrate can be engineered through geometric and spatial modulation of microscale features. In this body of work, micropost arrays were designed to induce (*i*) unidirectional single cell migration, (*ii*) maintenance and inhibition of collective cell behavior, and (*iii*) possible changes in the reprogramming and differentiation of induced pluripotent stem cells.

5.1 Micropost Array Gradients for Single Cell Migration

5.1.1 Microtopographic Durotaxis and Durotaxis *versus* Spatiotaxis Gradients

Micropost array gradients, consisting of circular micropost, were utilized to induce unidirectional cellular migration. Two types of arrays were designed: (*i*) microtopographic durotaxis gradients (*μDGs*), and (*ii*) microtopographic durotaxis versus spatiotaxis gradients (*μDSGs*).

The *μDGs* were engineered to create durotactic cues through microtopography by generating microscale stiffness gradients. In these arrays, the radii of microposts were increased along an axis of the array at two gradient strengths, low and high, and spaced a constant distance. To mitigate effects of increasing topographical surface area (availability of potential attachment sites) and gradients in substrate immobilized proteins, the effective microtopographic surface area was uniform for regimes of different micropost radii, and therefore different stiffnesses. This was accomplished by maintaining a constant ratio of micropost top surface area to a corresponding unit cell. As the interpost spacing along the axis of increasing micropost stiffness was also held constant, the interpost spacing perpendicular to this axis was appropriately adjusted. On the *μDGs*, BAECs moved faster and displaced farther in the direction of increasing micropost stiffness relative to the opposite of that direction. Additionally, this behavior was enhanced with higher gradient strength, where stiffness ranges were increased from 5-50 nN/μm to 5-390 nN/μm.

The *μDSGs* were developed to explore possible effects of micropost spacing on cellular migration, termed spatiotaxis, while cells simultaneously interfaced with durotactic cues. Although similar in design to the *μDGs* with increasing micropost stiffness over the length of the array, the *μDSGs* also included increasing interpost spacing. For consistency, the ratio of micropost top surface area to a corresponding unit cell was the same as the *μDGs*, but the interpost spacing was increased uniformly in the directions parallel and perpendicular to the direction of increasing stiffness. On the *μDSGs*, BAECs exhibited higher speeds and

displacements in the direction of decreasing interpost spacing (decreasing micropost stiffness) than in the direction opposite of that. These results show that gradients in spatial cues, or availability of attachment points, can influence cellular motility, and dominate opposing durotactic cues. This is the first demonstration of spatiotaxis, and suggests that interpost spacing is an important design consideration for microtopographic devices interfacing with cells.

5.1.2 Future Directions for Microtopographic Gradients

As discussed in Chapter 2, the *μDGs* and *μDSGs* have several limitations. In addition to having considerable movement in the directions perpendicular to the gradient axes, the micropost-specific topographical surface area increases with stiffness. The implementation of elliptical micropost arrays would be able to address these limitations (**Figure 5.1**). As mentioned previously, elliptical micropost arrays were able to limit cell migration to bidirectional movement along the major axes direction. [59] If the major and minor axes of the micropost are adjusted over the length of an array, thereby increasing anisotropy of the features, dual axis durotactic cues could be created. Since the stiffness is greater along the major axis relative to the minor axis, this design should reduce migration along the minor axis. Additionally, if the major axis increases while the minor axis decreases along the array, the stiffness increases along the direction of the major axis, providing a durotaxis gradient to induce unidirectional movement. Since the axes of the elliptical microposts can be adjusted individually, the micropost-specific topographical surface area can be kept constant for regimes of different stiffness.

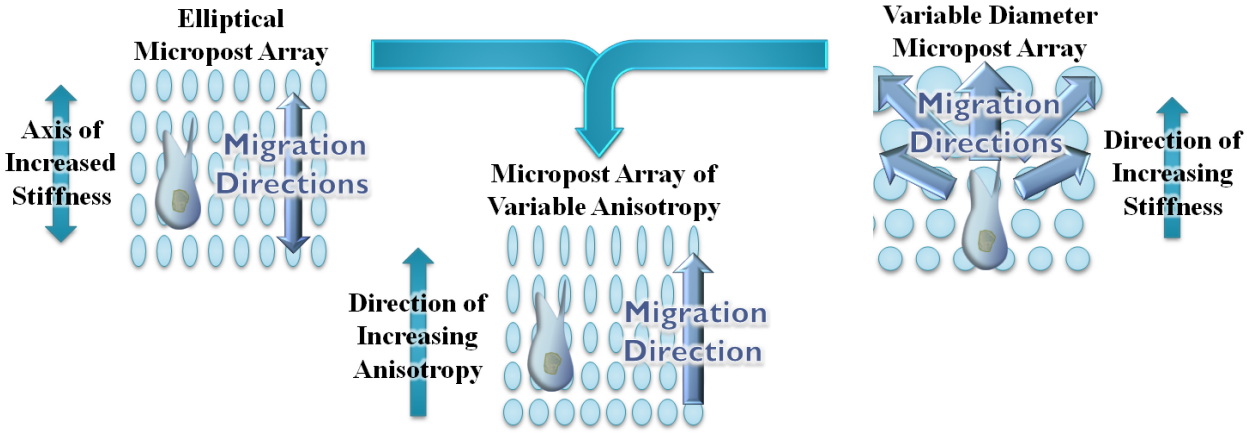

Figure 5.1. Concept for micropost arrays with increasing anisotropy.
To address the limitations of the *μDGs* and *μDSGs*, elliptical microposts with increasing anisotropy can be designed. Elliptical microposts have previously demonstrated the ability to limit migration bidirectionally along the direction of the major axes. By increasing the major axis length while decreasing the minor axis length over the course of the array, seeded cells will also receive dual axis durotactic cues for unidirectional migration. The elliptical nature of the microposts would reduce the movement of cells perpendicular to the axis of increasing micropost stiffness. As the major and minor axes can be adjusted independently, the micropost-specific top surface area can remain constant for regimes of different stiffnesses, mitigating any effects of increasing micropost-specific top surface area associated with circular microposts.

While the *μDSGs* were able to demonstrate dominance of spatial cues over stiffness cues, effects of spatial cues on cell motility have not been investigated independently of other migratory stimuli. The *μSGs* used in **Chapter 3** for investigating effects of spacing on collective cells, could be adapted for studying spatiotaxis. With uniform microposts and variable interpost spacing, *μSGs* with different ranges of interpost spacing could be tested.

Micropost array gradients have demonstrated their utility in inducing unidirectional cellular migration based on durotaxis and spatiotaxis biophysical cues on a platform that is simple to fabricate with high repeatability. In addition to their traditional use a traction force sensors, these substrates are well suited for interrogating the molecular dynamics of migration processes. Micropost array gradients would be able to yield dynamic traction force data during directed cellular migration, and could be used to investigate the effects of changes in stiffness and interpost spacing on the formation and dissolution of cell-substrate junctions, and intracellular processes such as cytoskeleton dynamics.

As the cellular migration results indicate, the geometry and interpost spacing can have different effects on cellular processes. The effects of spacing could possibly be minimized if the array were scaled down such that the critical dimensions are significantly smaller than those of cells. While nanoscale micropost arrays might offer a solution, there are several issues that should be taken into consideration. Currently, only the 2-D (x- and y-directions) planar effects of micropost arrays have been investigated – it is highly likely that out of plane (height, z-directions) dimensions might also affect cellular behavior. Although nanoscale features with the appropriate stiffness ranges can be fabricated and may be relevant in the x-y plane, their effects could be negated by the fact that cells might be able to touch the continuous substrate below because the features are not tall enough in the z-direction. Additionally, it is unclear how micropost-specific surface area affects cellular behavior, and the formation and density of cell-substrate junctions might require a minimum amount of continuous surface area. Fabrication of nanoscale features is also more time consuming and expensive than microscale features. [202] Despite their limitations, micropost array gradients are a versatile tool for controlling biophysical cues in the cellular microenvironment, and could have applications on both the research and industrial levels.

5.2 Micropost Arrays for Regulation of Collective Cell Behavior

5.2.1 Microtopographic Maintenance and Inhibition of Collective Cell Behavior

Uniform and gradient micropost arrays, using circular microposts, were used to mechanically influence collective cell behavior. Two groups of uniform micropost array substrates were tested: (*i*) microtopographic constant micropost height, variable micropost radius arrays (*μVRs*), and (*ii*) microtopographic constant micropost radius, variable micropost height

arrays (*μVHs*). Microtopographic spacing gradients, *μSGs*, with constant micropost geometry and variable interpost spacing were used to investigate whether or not spacing had effects on collective cell behavior.

For the *μVRs*, *μVHs*, and *μSGs*, cell collective were directly localized and grown on their micropost surfaces using a thin-film stenciling technique akin to metal lift-off microfabrication processes. BAECs were seeded at high density onto the micropost surfaces in thru-holes of thin-film stencils. After a few days of incubation in the thin-film openings, the BAECs were able to form cell collectives with cell-cell junctions. These collectives were released for observation by removing the stencils.

The *μVR* and *μVH* were designed to create surfaces of uniform apparent stiffnesses using various micropost geometries. For the *μVR*, uniform micropost arrays of a constant height were created for four different micropost radii within the range of stiffnesses of the *μDGs* and *μDSGs*. To maintain consistency, the ratio of micropost top surface area to a surrounding unit cells was held constant for all *μVRs* and equivalent to the ratio used for the *μDGs* and *μDSGs*. These devices enabled parallel testing of several different substrate stiffnesses at once in uniform environmental conditions. In contrast, the *μVHs* were uniform micropost arrays with a constant radius, the smallest of the ones used for the *μVRs*, at two different heights. These micropost arrays had the same microtopographic ratio as the *μVRs*. The microposts were spaced uniformly in both the x- and y-directions for both the *μVR* and *μVH*. On the *μVR*, BAEC collectives dispersed into single cells on the larger radii (stiffer) micropost arrays, and maintained their collective behavior on the smaller radii (softer) micropost arrays. Collectives dispersed at faster rates with increasing micropost radius.

From the single cell spatiotaxis studies, it was demonstrated that spatial cues can affect cellular behavior. Since the microtopographic ratio is constant for *μVR* with different radii, there are inherent differences in interpost spacing as well. The *μVHs* were created to mitigate effects of spacing while simultaneously changing the substrate stiffness cues. On the *μVHs*, BAEC collectives dispersed into single cells on the stiffer micropost arrays in a manner similar to cells on the stiffer *μVRs*. The *μVHs* were shorter (stiffer) versions of the *μVR* with radii of 1.5 μm, and this dispersive behavior indicated that the inhibition of collective cell behavior was repeatable, independent of micropost geometry. Cell collectives dispersed at faster rates with decreasing micropost height. The stiffnesses of the *μVHs* were comparable to some of the *μVRs*, though slightly softer. It is interesting to note that while *μVRs* have stiffer microposts than the *μVHs*, cell collectives dispersed at faster rates on the *μVHs* based on the fabricated prototype micropost arrays. This is likely due to the fact that microposts on the *μVHs* are closer to one another, making it easier for cells to migrate away, as suggested by the single cell migration data of the *μDSGs*.

The effects of interpost spacing on collective cell behavior were also explored using the *μSGs*. The *μSGs* had microposts identical to the *μVRs* that were able to maintain collective cell

behavior (smallest radii) and interpost spacing that decreased over the length of the array. Similar to the uniform and gradient micropost arrays, the ratio of the micropost top surface area to a corresponding unit cell was held constant for regimes of smaller interpost spacing. To maintain this ratio, the interpost spacing perpendicular to the direction of decreasing interpost spacing was increased. The range of interpost spacing for the *μSGs* was 2-3 times that of the *μVHs* and *μVRs* with radii of 1.5 μm. Cell collectives on the *μSGs* were found to have multiple behaviors, with simultaneous contraction and expansion at different parts of the collectives. Overall, collectives expanded in area and the movement of the collectives' centroids did not appear to be guided by the micropost gradient. These results reemphasize the importance of interpost spacing in micropost arrays as interpost spacing was able to disrupt the maintenance of collective cell behavior on surfaces with favorable stiffness cues.

5.2.2 Future Directions for Microtopography-based Collective Cell Studies

The uniform micropost arrays with varying geometry and thin-film stenciling method have shown that microtopography can be used to mechanically regulate collective cell behavior and induce collective-to-single cell transitions. This testing methodology has the potential to dissect the biophysical force balance that is hypothesized to exist between cell-cell and cell-substrate junctions. Since transitional behavior can be induced on these surfaces, associated traction force data and possibly intracellular information could be derived from collective cell experiments. By incorporating chemical cues or transfected cell lines into the system, this biophysical force balance could be interrogated by removing cellular capabilities of forming such junctions (**Figure 5.2**). Methods can include the disruption of either the cytoskeleton or cell-cell junctions. Chemicals, such cytochalasin D, could be used to disrupt Actin microfilaments to favor cell-cell junctions, [203] or culturing cell collectives in low calcium media to interfere with cadherins for inducing single cell behavior. [204], [205] Additionally, cells that have been transfected for suppression of other factors necessary for forming junctions, such as FAK, can also be explored. [206] As these substrates can be used in concert with chemical cues, it is possible to use this methodology to elucidate the cellular hierarchy of responses to different types of microenvironmental cues. Utilizing this technology with other microenvironmental stimuli could have many potential applications in drug screening, tissue engineering, and characterization and induction of transitional behavior of cells characteristic of biological phenomena, such as wound healing or cancer metastasis.

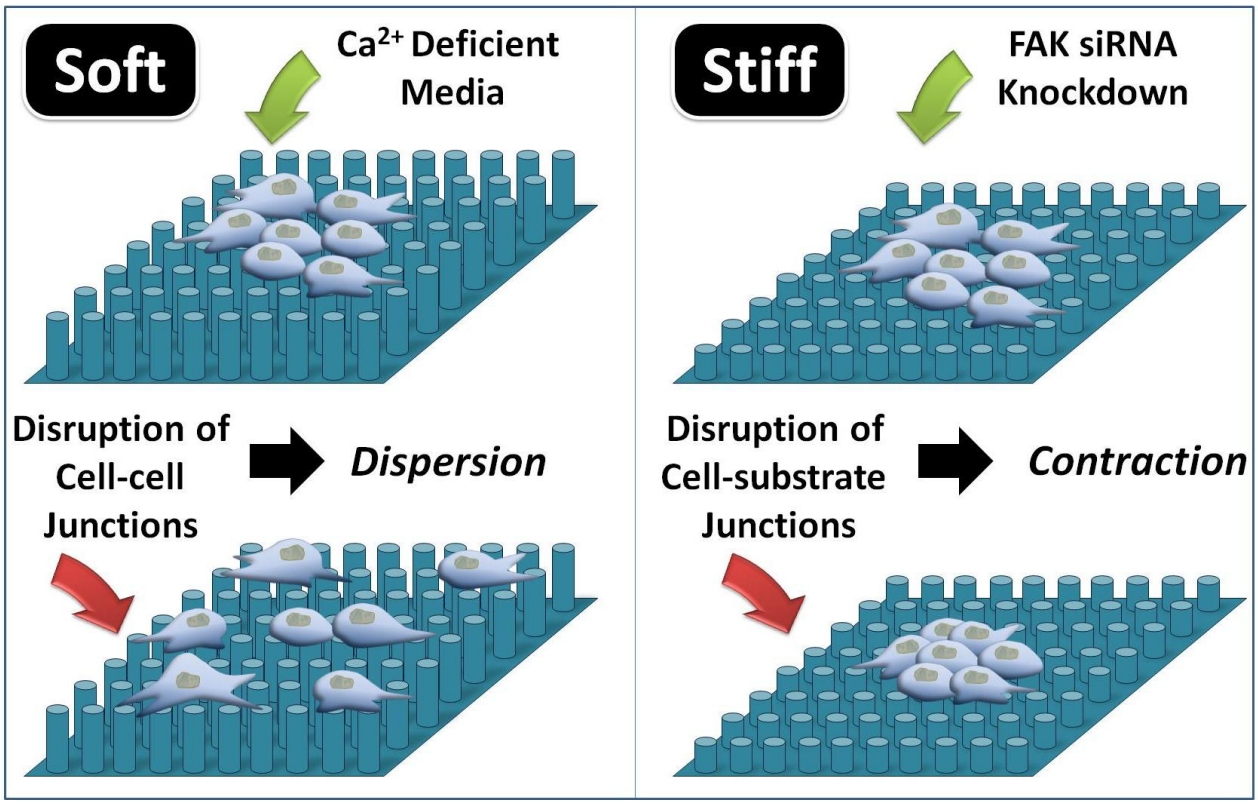

Figure 5.2. Investigating the biophysical force balance between cell-cell and cell-substrate junctions. The micropost array platform can be used to investigate the biophysical force balance between cell-cell and cell-substrate junctions. As demonstrated, varying the stiffness of micropost arrays can maintain or inhibit collective cell behavior by modifying the cell-substrate junctions. If this system is combined with chemical factors or transfection methods that modify the cell-cell junctions, it may be possible to override the biophysical cues of the cellular substrate. Both sets of cues could be tuned to determine transition points in the dominance of one cue over the other. Additionally, forces associated with transitional behavior could be measured through micropost deflection to further characterize this force balance.

While collective cell behavior was shown to be repeatable for microposts with similar stiffnesses but varying geometries, the microposts used for these experiments were confined to the geometries used in the single cell migration studies for consistency. As collective cell behavior differs significantly from single cell behavior, it is possible that new types of collective cell phenomenon might be observed for stiffnesses and interpost spacing regimes differing from those used for interrogating single cell behavior. For instance, while gradients in interpost spacing were able to induce single cell behavior, collective cell migration was not observed on the *μSGs*. Collective cell migration could be possible if the micropost array gradients included different ranges and increments of stiffnesses and interpost spacing in their design. Additionally, like the micropost array gradients, this test methodology would benefit from scaling down the micropost dimensions to produce a substrate that appears more continuous to cells.

5.3 Micropost Arrays for Cell Reprogramming

5.3.1 Effects of Virus Concentration and Microtopography on iPSC Colony Formation

As the reprogramming methodology was developed in parallel with the reprogramming experiments, many factors, such as initial seeding density, were found to influence the results of the reprogramming processes. Low passage mERFs were infected at a targeted MOI using lentiviruses for the original Yamanaka factors (OSKM), and seeded at three concentrations (multiples of confluency) on TC dishes. These cells were incubated over several days to observe the effects of initial seeding density on iPSC reprogramming processes. After four days in culture, colonies formed on the dishes with the lowest seeding density before the dishes with the higher seeding densities. However, after eight days in culture, the number of colonies formed on the dishes was proportional to the initial seeding densities. Colonies formed on the dishes with the lowest initial seeding density were the largest, on average, after eight days of culture. The differences in colony size among the three seeding densities were not found to be statistically significant.

The proportionality between initial seeding density and formation of colonies is expected as increasing the seeding density also increasing the likelihood that a reprogrammed cell is present in a sample. Additionally, higher seeding densities may result in greater numbers of cell-cell junctions due to increased cell-cell contact. As E-cadherins have been shown to be integral to the reprogramming process of cells, an increase in the number of junctions may also contribute to this result.

5.3.2 Effects of Seeding Density on iPSC Colony Formation

Uniform arrays of circular microposts were used to investigate possible effects of microtopography on the reprogramming and differentiation of infected mERFs. *μVRs*, similar to the ones used for the collective cell studies, were designed with several micropost radii in the stiffness ranges of the *μDGs* and *μDSGs* for single cell migration. This enabled parallel testing of multiple stiffnesses on the same devices. These micropost arrays were fabricated at two heights, denoted as μVR_2 and μVR_7. Flat PDMS surfaces were used as controls for these experiments.

mERFs were infected at three different lentivirus infection levels (concentrations) and seeded onto all substrate types at approximately the same density. The seeding suspensions were confined to specific areas on the flat PDMS surfaces, $\mu VR_2 s$, and $\mu VR_7 s$ in wells created by PDMS frames. This ensured consistent seeding for different surfaces. Colonies were able to form on all surfaces and iPSCs were confirmed by staining for Oct-3/4 and Nanog. The infected mERFs were also able to form colonies that exhibited beating, many of which had several sections with asynchronous beating. The colonies had beating frequencies that ranged from 0.2-1 Hz for all surfaces, and could form as early as 10-20 days after infection. This is a notable result considering that chemical factors have been required to achieve directed differentiation of iPSCs

into cardiomyocytes within such a short time frame. Positive staining for both Myosin heavy chain and cardiac Troponin T indicated that the beating in the colonies was likely due to cardiomyocyte differentiation.

Both lentivirus concentration and substrate microtopography appeared to influence the reprogramming and differentiation processes of mERFs. The total number of iPSC colonies that formed on all surfaces almost directly increased with virus concentration. This was expected as increasing virus concentration, similar to increasing initial seeding density, also increases the probability that reprogramming events in cells will occur. Microtopography did not have as strong an effect on colony formation as virus concentration; however, at specific virus concentrations, microtopography appeared to influence the relative numbers of iPSC colonies that formed on different surfaces. For the lowest virus concentration, μVR_2 formed the fewest colonies. However, flat PDMS and the μVR_2 formed the most colonies for the mid and highest virus concentrations, respectively.

In addition to the total number of iPSC colonies formed, the number of beating colonies was recorded. Beating colony formation was not directly proportional to virus concentration. Relative to the lowest virus concentration, the number of beating colonies decreased and increased for the mid and highest virus concentrations, respectively. The relative numbers of beating colonies was also affected by microtopography. At the lowest virus concentration, all surfaces yielded the same average number of beating colonies. At the mid and highest virus concentrations, the formation of beating colonies followed the trend for the formation of iPSC colonies. It was also found that the surfaces that produced the greatest number of beating colonies also had the highest percentage of beating colonies.

These results suggest virus concentration is an important factor for determining the average number of iPSC colonies and absolute numbers of beating colonies that form. Microtopography appears to have secondary effects on the reprogramming and differentiation processes of iPSCs by increasing or decreasing relative numbers of iPSC and beating colonies that form on surfaces at set virus concentrations. Specific virus concentrations, therefore, may be more effective at producing different lineages of cells on different substrate microtopographies.

Similar subsequent experiments have indicated that the onset of beating in iPSC colonies is difficult to control. In addition to initial seeding densities, virus concentrations, and microtopography, factors such as the sources of cells, cell passage number, incubation periods, and the quality of viruses may affect mERF reprogramming and differentiation.

5.3.3 Effects of Microtopography on mERFs

To investigate how microtopography physically changes cells, normal, non-infected mERFs were seeded on, μVR_2s, μVR_7s, flat PDMS surfaces, and TC dishes for 24-hour periods. The mERFs were subsequently stained for Lamin A/C, HDAC4, Nesprin, and Actin.

For the TC dishes and flat PDMS surfaces, the mERFs were widely spread out with ovular nuclei. Lamin A/C was expressed in the nuclei and cytoplasms of cells for both surfaces. Although HDAC4 was found in the cytoplasm of mERFs on the TC dishes, the protein was largely confined to the nuclei on the flat PDMS surfaces. On the μVR_2s, mERFs had slight physical changes due to the microposts, including smaller spreading areas and thinner protrusions. For the majority of the μVR_2s, both HDAC4 and Lamin A/C were present in the cytoplasms and nuclei of cells. In contrast to both flat surfaces and the μVR_2s, mERFs on the μVR_7s were highly affected by the surface microtopography. In addition to having small spreading areas and distorted nuclear shapes, mERFs exhibited some alignment with the underlying microposts. For these surfaces, HDAC4 was found mainly in the cytoplasm of cells with little expression in the nuclei. Lamin A/C was found in both the nuclei and cytoplasms. Nesprin expression had significant overlap with Actin and was primarily cytoplasmic for all surfaces.

Normalized fluorescence intensities were used to numerically compare protein expression. The expression of both Lamin A/C and HDAC4 were statistically higher on the TC dishes than all other surfaces. Flat PDMS surfaces also had high expression, and had similar intensities to the μVR_2s with smaller radii. TC dishes, flat PDMS surfaces, and μVR_2s had higher relative intensities of Lamin A/C in comparison to HDAC4, and this trend was reversed for the μVR_7s. μVR_2s had statistically higher expression of Lamin A/C than μVR_7s with corresponding radii. HDAC4 did not have a similar trend, with statistical differences for the two μVRs only occurring for the micropost arrays with smaller radii. For Nesprin, the μVR_7s had slightly higher expression than the μVR_2s, but this difference was only significant for the micropost arrays with the smallest radii. The flat surfaces had comparable expression. Actin expression had high variability for both micropost array surfaces, and high and low expression for the flat PDMS surfaces and TC dishes, respectively.

These physical differences suggest that microtopography can influence the regulation of genes through nuclear and cytoplasmic localization of HDAC4. The shuttling of HDAC4 to the cytoplasm likely indicates suppression of its activity. Therefore, on the TC dishes and μVR_7s, HDAC4 was highly suppressed. In contrast, on the flat PDMS and the μVR_2s, HDAC4 had high expression in the nuclei, suggesting strong transcription activity. Microtopography also appeared to affect the structural stability of the nuclei through the relative expressions of Lamin A/C. The TC dishes, flat PDMS surfaces, and μVR_2s had stronger expression of Lamin A/C at the cell nuclei than the μVR_7s. The nuclei on the μVR_7s surfaces were able to distort and conform to the edges of the microposts. The Nesprin staining was not localized at the nucleus as expected, suggesting that different antibodies will be required for staining this protein in mERFs.

5.3.2 Future Directions for Microtopography-based iPSC Studies

This preliminary work has demonstrated that microtopography has the potential for influencing the reprogramming and differentiation of iPSCs. Although the early onset of colony

beating without the use of chemical cues is a promising result, controlling this and rates of colony formation proved to be difficult. This is likely due to changes in other factors in these experiments. Effects of changes in the initial seeding densities and lentivirus infection levels indicate the importance of non-biophysical cues in these processes. Therefore, it is imperative that all other factors are tightly controlled to reveal the true influence of microtopography and other biophysical cues in future experiments. Virus concentration, which was never measured for any of these experiments, must be quantified to ensure consistency. Other means of generating iPSCs, such as doxycycline-inducible reprogramming, [207], [208] maybe provide an alternate system for investigation of effects of biophysical cues. Additionally, the cell lines and their passage number are important to consider. Experiments have shown that iPSCs could not produce the beating phenotype from higher passages of mERFs or other cells lines, such as fibroblasts derived from tail tissue.

From the microtopography studies, it is unclear what biophysical cues are resulting in changes to the reprogramming and differentiation processes. The current *μVRs* deliver many types of biophysical cues: substrate stiffness, spacing of attachment points, and different geometries, some of which enable contact with the continuous substrate below. To determine the effects each of these has on these processes, developing systems that isolate these cues is imperative. As used for tissues and stem cells, [46], [113] polyacrylamide gels can be employed to study changes in substrates stiffness on a continuous surface. Similar to the *μVRs* and *μVHs* used in the collective cell studies, microposts with varying geometry and same theoretical stiffnesses can be utilized to explore how micropost radii and heights affect cellular behavior. The influence of spacing of attachment points can also be investigated on *μSGs* or through changes in *%ECM*. Additionally, further investigation of the structural and transcription changes that occur due to microtopography should be conducted, such as through polymerase chain reaction (PCR), to understand the possible mechanisms behind changes in the reprogramming and differentiation processes of iPSCs.

The long term goal of implementing biophysical cues in the reprogramming and differentiation of iPSCs is to determine if they can be used in concert or in lieu of other microenvironmental cues to increase reprogramming efficiencies or direct differentiation. Biophysical cues can further be explored by reducing the number of transcription factors used in the reprogramming process, e.g. using OSK instead of OSKM, and observing their effects. As biophysical cues can affect the behavior of both somatic adult cells and stem cells, their influence over other aspects of iPSCs, such as epigenetic memory, [209] would be areas worthy of investigation.

References

[1] A. C. Guyton and J. E. Hall, *Textbook of Medical Physiology*, 10th ed. Saunders, 2000, p. 1064 .

[2] H. Gray, L. H. Bannister, M. M. Berry, and P. L. Williams, *Gray's Anatomy: The Anatomical Basis of Medicine & Surgery*, 38th ed. Churchill Livingstone, 1995, p. 2092.

[3] B. Assmus et al., "Transplantation of Progenitor Cells and Regeneration Enhancement in Acute Myocardial Infarction (TOPCARE-AMI)," *Circulation*, vol. 106, no. 24, pp. 3009-3017, Nov. 2002.

[4] A. E. Butler, J. Janson, S. Bonner-weir, R. Ritzel, R. A. Rizza, and P. C. Butler, "β-Cell Deficit and Increased β-Cell Apoptosis inHumans With Type 2 Diabetes," *Diabetes*, vol. 52, no. 1, pp. 102-110, 2003.

[5] M. Al-Hajj, M. S. Wicha, A. Benito-Hernandez, S. J. Morrison, and M. F. Clarke, "Prospective identification of tumorigenic breast cancer cells.," *Proceedings of the National Academy of Sciences of the United States of America*, vol. 100, no. 7, pp. 3983-8, Apr. 2003.

[6] P. Paterlini-Brechot and N. L. Benali, "Circulating tumor cells (CTC) detection: clinical impact and future directions.," *Cancer letters*, vol. 253, no. 2, pp. 180-204, Aug. 2007.

[7] J. Itskovitz-eldor et al., "Differentiation of Human Embryonic Stem Cells into Embryoid Bodies Comprising the Three Embryonic Germ Layers," *Molecular Medicine*, vol. 6, no. 2, pp. 88-95, 2000.

[8] E. M. Zeisberg et al., "Endothelial-to-mesenchymal transition contributes to cardiac fibrosis.," *Nature medicine*, vol. 13, no. 8, pp. 952-61, Aug. 2007.

[9] S. Hakomori, "Glycosphingolipids in cellular interaction, differentiation, and oncogenesis.," *Annual review of biochemistry*, vol. 50, pp. 733-64, Jan. 1981.

[10] G. C. Gurtner, S. Werner, Y. Barrandon, and M. T. Longaker, "Wound repair and regeneration.," *Nature*, vol. 453, no. 7193, pp. 314-21, May 2008.

[11] M. P. Lutolf and J. a Hubbell, "Synthetic biomaterials as instructive extracellular microenvironments for morphogenesis in tissue engineering.," *Nature biotechnology*, vol. 23, no. 1, pp. 47-55, Jan. 2005.

[12] J. El-Ali, P. K. Sorger, and K. F. Jensen, "Cells on chips.," *Nature*, vol. 442, no. 7101, pp. 403-11, Jul. 2006.

[13] M. Tamura, “Inhibition of Cell Migration, Spreading, and Focal Adhesions by Tumor Suppressor PTEN,” *Science*, vol. 280, no. 5369, pp. 1614-1617, Jun. 1998.

[14] R. H. Burdon, “Superoxide and hydrogen peroxide in relation to mammalian cell proliferation,” *Free Radical Biology and Medicine*, vol. 18, no. 4, pp. 775-794, Apr. 1995.

[15] J. Gerdes, H. Lemke, H. Baisch, H. Wacker, U. Schwab, and H. Stein, “Cell cycle analysis of a cell proliferation-associated human nuclear antigen defined by the monoclonal antibody Ki-67,” *J. Immunol.*, vol. 133, no. 4, pp. 1710-1715, Oct. 1984.

[16] B. S. H. Zigmond and J. G. Hirsch, “Leukocyte locomotion and chemotaxis: New methods for evaluation, and demonstration of a cell-derived chemotactic factor,” *Journal of Experimental Medicine*, vol. 137, pp. 387-410, 1973.

[17] S. Yao et al., “Long-term self-renewal and directed differentiation of human embryonic stem cells in chemically defined conditions.,” *Proceedings of the National Academy of Sciences of the United States of America*, vol. 103, no. 18, pp. 6907-12, May 2006.

[18] H. Wichterle, I. Lieberam, J. A. Porter, and T. M. Jessell, “Directed Differentiation of Embryonic Stem Cells into Motor Neurons,” *Cell*, vol. 110, no. 3, pp. 385-397, Aug. 2002.

[19] H. Billig, “Estrogens inhibit and androgens enhance ovarian granulosa cell apoptosis,” *Endocrinology*, vol. 133, no. 5, pp. 2204-2212, Nov. 1993.

[20] R. J. Cody et al., “Atrial natriuretic factor in normal subjects and heart failure patients. Plasma levels and renal, hormonal, and hemodynamic responses to peptide infusion.,” *The Journal of clinical investigation*, vol. 78, no. 5, pp. 1362-74, Nov. 1986.

[21] G. García-Cardeña, P. Oh, J. Liu, J. E. Schnitzer, and W. C. Sessa, “Targeting of nitric oxide synthase to endothelial cell caveolae via palmitoylation: implications for nitric oxide signaling.,” *Proceedings of the National Academy of Sciences of the United States of America*, vol. 93, no. 13, pp. 6448-53, Jun. 1996.

[22] K. R. Robinson, “The Responses of Cells to Electrical Fields: A Review,” *Journal of Cell Biology*, vol. 101, pp. 2023-2027, 1985.

[23] P. W. Luther and H. B. Peng, “Changes in cell shape and actin distribution induced by constant electric fields,” *Nature*, vol. 303, no. 5, pp. 61-64, 1983.

[24] T. M. Dexter, T. D. Allen, and L. G. Lajtha, “Conditions controlling the proliferation of haemopoietic stem cells in vitro.,” *Journal of cellular physiology*, vol. 91, no. 3, pp. 335-44, Jun. 1977.

[25] G. Mahmud et al., “Directing cell motions on micropatterned ratchets,” *Nature Physics*, vol. 5, no. 8, pp. 606-612, Jun. 2009.

[26] A. A. Brahmbhatt and R. L. Klemke, “ERK and RhoA differentially regulate pseudopodia growth and retraction during chemotaxis.,” *The Journal of biological chemistry*, vol. 278, no. 15, pp. 13016-25, Apr. 2003.

[27] A. M. Kloxin, A. M. Kasko, C. N. Salinas, and K. S. Anseth, “Photodegradable hydrogels for dynamic tuning of physical and chemical properties.,” *Science (New York, N.Y.)*, vol. 324, no. 5923, pp. 59-63, Apr. 2009.

[28] D. V. Zhelev, A. M. Alteraifi, and D. Chodniewicz, “Controlled pseudopod extension of human neutrophils stimulated with different chemoattractants.,” *Biophysical journal*, vol. 87, no. 1, pp. 688-95, Jul. 2004.

[29] B. Heit, S. Tavener, E. Raharjo, and P. Kubes, “An intracellular signaling hierarchy determines direction of migration in opposing chemotactic gradients.,” *The Journal of cell biology*, vol. 159, no. 1, pp. 91-102, Oct. 2002.

[30] N. Xia et al., “Directional control of cell motility through focal adhesion positioning and spatial control of Rac activation,” *The FASEB Journal*, pp. 1649-1659.

[31] N. Wang, J. D. Tytell, and D. E. Ingber, “Mechanotransduction at a distance: mechanically coupling the extracellular matrix with the nucleus,” vol. 10, no. JANuARy, pp. 75-82, 2009.

[32] N. Wang, J. Butler, and D. Ingber, “Mechanotransduction across the cell surface and through the cytoskeleton,” *Science*, vol. 260, no. 5111, pp. 1124-1127, May 1993.

[33] K.-den Chen et al., “Mechanotransduction in Response to Shear Stress: Roles of Receptor Tyrosine Kinases, Integrins, and Shc,” *Biochemistry*, vol. 274, no. 26, pp. 18393-18400, 1999.

[34] M. A. Wozniak and C. S. Chen, “Mechanotransduction in development: a growing role for contractility.,” *Nature reviews. Molecular cell biology*, vol. 10, no. 1, pp. 34-43, Jan. 2009.

[35] D. E. Jaalouk and J. Lammerding, “Mechanotransduction gone awry.,” *Nature reviews. Molecular cell biology*, vol. 10, no. 1, pp. 63-73, Jan. 2009.

[36] D. E. Discher, P. Janmey, and Y.-L. Wang, “Tissue cells feel and respond to the stiffness of their substrate.,” *Science (New York, N.Y.)*, vol. 310, no. 5751, pp. 1139-43, Nov. 2005.

[37] P. F. Davies, “Flow-mediated endothelial mechanotransduction.,” *Physiological reviews*, vol. 75, no. 3, pp. 519-60, Jul. 1995.

[38] A. Katsumi, a W. Orr, E. Tzima, and M. A. Schwartz, “Integrins in mechanotransduction.,” *The Journal of biological chemistry*, vol. 279, no. 13, pp. 12001-4, Mar. 2004.

[39] D. E. Ingber, “Tensegrity: the architectural basis of cellular mechanotransduction.,” *Annual review of physiology*, vol. 59, pp. 575-99, Jan. 1997.

[40] M. A. Schwartz and D. W. DeSimone, “Cell adhesion receptors in mechanotransduction.,” *Current opinion in cell biology*, vol. 20, no. 5, pp. 551-6, Oct. 2008.

[41] C. M. Lo, H. B. Wang, M. Dembo, and Y. L. Wang, “Cell movement is guided by the rigidity of the substrate.,” *Biophysical journal*, vol. 79, no. 1, pp. 144-52, Jul. 2000.

[42] A. L. Berrier and K. M. Yamada, “Cell-matrix adhesion.,” *Journal of cellular physiology*, vol. 213, no. 3, pp. 565-73, Dec. 2007.

[43] E. H. Burger and J. Klein-Nulend, “Mechanotransduction in bone--role of the lacuno-canalicular network.,” *FASEB journal : official publication of the Federation of American Societies for Experimental Biology*, vol. 13 Suppl, pp. S101-12, Jan. 1999.

[44] T. Yeung et al., “Effects of Substrate Stiffness on Cell Morphology , Cytoskeletal Structure , and Adhesion,” *Culture*, vol. 34, no. April 2004, pp. 24 -34, 2005.

[45] B. P. Toole, T. N. Wight, and M. I. Tammi, “Hyaluronan-cell interactions in cancer and vascular disease.,” *The Journal of biological chemistry*, vol. 277, no. 7, pp. 4593-6, Feb. 2002.

[46] A. J. Engler, S. Sen, H. L. Sweeney, and D. E. Discher, “Matrix Elasticity Directs Stem Cell Lineage Specification,” *Cell*, pp. 677-689, 2006.

[47] B. N. Zaari, P. Rajagopalan, S. K. Kim, A. J. Engler, and J. Y. Wong, “Photopolymerization in Microfluidic Gradient Generators : Microscale Control of Substrate Compliance to Manipulate Cell Response **,” no. 23, pp. 2133-2137, 2004.

[48] B. C. Isenberg, P. a Dimilla, M. Walker, S. Kim, and J. Y. Wong, “Vascular smooth muscle cell durotaxis depends on substrate stiffness gradient strength.,” *Biophysical journal*, vol. 97, no. 5, pp. 1313-22, Sep. 2009.

[49] J. A. Burdick, A. Khademhosseini, and R. Langer, “Fabrication of Gradient Hydrogels Using a Microfluidics/Photopolymerization Process,” *Langmuir*, vol. 20, no. 13, pp. 5153-5156, Jun. 2004.

[50] Y. Ni and M. Y. M. Chiang, “Cell morphology and migration linked to substrate rigidity,” *Society*, no. July, pp. 1285-1292, 2007.

[51] S. Kidoaki, “Mechanics in Cell Adhesion and Motility on the Elastic Substrates,” *Journal of Biomechanical Science and Engineering*, vol. 5, no. 3, pp. 218-228, 2010.

[52] J. B. Leach, X. Q. Brown, J. G. Jacot, P. A. Dimilla, and J. Y. Wong, "Neurite outgrowth and branching of PC12 cells on very soft substrates sharply decreases below a threshold of substrate rigidity," *Cell*, vol. 4, pp. 26-34, 2007.

[53] K.-ichiro Kamei et al., "Microfluidic image cytometry for quantitative single-cell profiling of human pluripotent stem cells in chemically defined conditions †," *Society*, no. Cdm, pp. 1113-1119, 2010.

[54] C.-min Lo, H.-bei Wang, M. Dembo, and Y.-li Wang, "Cell Movement Is Guided by the Rigidity of the Substrate," *Biophysical Journal*, vol. 79, no. July, pp. 144-152, 2000.

[55] W.-hui Guo, M. T. Frey, N. a Burnham, and Y.-li Wang, "Substrate rigidity regulates the formation and maintenance of tissues.," *Biophysical journal*, vol. 90, no. 6, pp. 2213-20, Mar. 2006.

[56] J. Fu et al., "Mechanical regulation of cell function with geometrically modulated elastomeric substrates.," *Nature methods*, vol. 7, no. 9, pp. 733-6, Sep. 2010.

[57] J. Y. Wong, A. Velasco, P. Rajagopalan, and Q. Pham, "Directed Movement of Vascular Smooth Muscle Cells on Gradient-compliant Hydrogels," *Exposure*, no. 9, pp. 1908-1913, 2003.

[58] E. Hadjipanayi, V. Mudera, and R. A. Brown, "Guiding cell migration in 3D: a collagen matrix with graded directional stiffness.," *Cell motility and the cytoskeleton*, vol. 66, no. 3, pp. 121-8, Mar. 2009.

[59] A. Saez, M. Ghibaudo, A. Buguin, and P. Silberzan, "Rigidity-driven growth and migration of epithelial cells on microstructured anisotropic substrates," vol. 104, no. 20, pp. 1-6, 2007.

[60] A. Khademhosseini, R. Langer, J. Borenstein, and J. P. Vacanti, "Microscale technologies for tissue engineering and biology.," *Proceedings of the National Academy of Sciences of the United States of America*, vol. 103, no. 8, pp. 2480-7, Feb. 2006.

[61] N. J. Sniadecki and C. S. Chen, "Microfabricated silicone elastomeric post arrays for measuring traction forces of adherent cells.," *Methods in cell biology*, vol. 83, pp. 313-28, Jan. 2007.

[62] J. A. N. M. Bruder, A. P. Lee, and D. Hoffman-kim, "Biomimetic materials replicating Schwann cell topography enhance neuronal adhesion and neurite alignment in vitro," *Polymer*, vol. 18, no. 8, pp. 967- 982, 2007.

[63] M. T. Lam, W. C. Clem, and S. Takayama, "Reversible on-demand cell alignment using reconfigurable microtopography.," *Biomaterials*, vol. 29, no. 11, pp. 1705-12, Apr. 2008.

[64] D.-H. Kim, K. Han, K. Gupta, K. W. Kwon, K.-Y. Suh, and A. Levchenko, "Mechanosensitivity of fibroblast cell shape and movement to anisotropic substratum topography gradients.," *Biomaterials*, vol. 30, no. 29, pp. 5433-44, Oct. 2009.

[65] a Curtis and C. Wilkinson, "Topographical control of cells.," *Biomaterials*, vol. 18, no. 24, pp. 1573-83, Dec. 1997.

[66] B. A. Dalton et al., "Modulation of epithelial tissue and cell migration by microgrooves.," *Journal of biomedical materials research*, vol. 56, no. 2, pp. 195-207, Aug. 2001.

[67] J. L. Tan, J. Tien, D. M. Pirone, D. S. Gray, K. Bhadriraju, and C. S. Chen, "Cells lying on a bed of microneedles: an approach to isolate mechanical force.," *Proceedings of the National Academy of Sciences of the United States of America*, vol. 100, no. 4, pp. 1484-9, Feb. 2003.

[68] A. Saez, M. Ghibaudo, A. Buguin, and P. Silberzan, "Rigidity-driven growth and migration of epithelial cells on microstructured anisotropic substrates," vol. 104, no. 20, pp. 1-6, 2007.

[69] R. Sudo, N. Takahashi, T. Mitaka, M. Ikeda, and K. Tanishita, "The Effect of Micropatterned Pores on the Formation and Movement of Small Hepatocyte Colonies," *Journal of Biomechanical Science and Engineering*, vol. 3, no. 2, pp. 249-262, 2008.

[70] E. Engel, E. Martínez, C. A. Mills, M. Funes, J. A. Planell, and J. Samitier, "Mesenchymal stem cell differentiation on microstructured poly (methyl methacrylate) substrates.," *Annals of anatomy = Anatomischer Anzeiger : official organ of the Anatomische Gesellschaft*, vol. 191, no. 1, pp. 136-44, Jan. 2009.

[71] P. Uttayarat, M. Chen, M. Li, F. D. Allen, R. J. Composto, and P. I. Lelkes, "Microtopography and flow modulate the direction of endothelial cell migration.," *American journal of physiology. Heart and circulatory physiology*, vol. 294, no. 2, pp. H1027-35, Feb. 2008.

[72] J. R. Hutchinson, "Shear Coefficients for Timoshenko Beam Theory," *Journal of Applied Mechanics*, vol. 68, no. 1, p. 87, 2001.

[73] A. Saez, E. Anon, M. Ghibaudo, O. Roure, and J.-m D. Meglio, "Traction forces exerted by epithelial cell sheets," vol. 194119, 2010.

[74] P. Friedl, Y. Hegerfeldt, and M. Tusch, "Collective cell migration in morphogenesis and cancer.," *The International journal of developmental biology*, vol. 48, no. 5–6, pp. 441-9, Jan. 2004.

[75] S. Aznavoorian, "Signal Transduction for Chemotaxis and Haptotaxis by Matrix Molecules in Tumor Cells," *Cell*, vol. 110, no. April, pp. 1427-1438, 1990.

[76] M. Zhao et al., “Electrical signals control wound healing through phosphatidylinositol-3-OH kinase-gamma and PTEN.,” *Nature*, vol. 442, no. 7101, pp. 457-60, Jul. 2006.

[77] E. Wang, M. Zhao, J. V. Forrester, and C. D. McCaig, “Bi-directional migration of lens epithelial cells in a physiological electrical field,” *Experimental Eye Research*, vol. 76, no. 1, pp. 29-37, Jan. 2003.

[78] M. R. Cho, H. S. Thatte, R. C. Lee, and D. E. Golan, “Integrin-Dependent Human Macrophage Migration Induced by Oscillatory Electrical Stimulation,” *Annals of Biomedical Engineering*, vol. 28, no. 3, pp. 234-243, Mar. 2000.

[79] A. Bahat, I. Tur-Kaspa, A. Gakamsky, L. C. Giojalas, H. Breitbart, and M. Eisenbach, “Thermotaxis of mammalian sperm cells: A potential navigation mechanism in the female genital tract,” *Nature Medicine*, vol. 9, , pp. 149 - 150, 2003.

[80] K. K. I. T. Parker et al., “Directional control of lamellipodia extension by constraining cell shape and orienting cell tractional forces,” *The FASEB Journal*, pp. 1195-1204.

[81] X. Jiang, D. A. Bruzewicz, A. P. Wong, M. Piel, and G. M. Whitesides, “Directing cell migration with asymmetric micropatterns.,” *Proceedings of the National Academy of Sciences of the United States of America*, vol. 102, no. 4, pp. 975-8, Jan. 2005.

[82] X. Trepat et al., “Physical forces during collective cell migration,” *Nature Physics*, vol. 5, no. 6, pp. 426-430, May 2009.

[83] M. Singh, C. Berkland, and M. S. Detamore, “Strategies and applications for incorporating physical and chemical signal gradients in tissue engineering.,” *Tissue engineering. Part B, Reviews*, vol. 14, no. 4, pp. 341-66, Dec. 2008.

[84] S. Li et al., “The role of the dynamics of focal adhesion kinase in the mechanotaxis of endothelial cells.,” *Proceedings of the National Academy of Sciences of the United States of America*, vol. 99, no. 6, pp. 3546-51, Mar. 2002.

[85] P. J. Mack, M. R. Kaazempur-Mofrad, H. Karcher, R. T. Lee, and R. D. Kamm, “Force-induced focal adhesion translocation: effects of force amplitude and frequency.,” *American journal of physiology. Cell physiology*, vol. 287, no. 4, pp. C954-62, Oct. 2004.

[86] J. Ando, H. Nomura, and A. Kamiya, “The effect of fluid shear stress on the migration and proliferation of cultured endothelial cells,” *Microvascular Research*, vol. 33, no. 1, pp. 62-70, Jan. 1987.

[87] S. Hsu, R. Thakar, D. Liepmann, and S. Li, “Effects of shear stress on endothelial cell haptotaxis on micropatterned surfaces.,” *Biochemical and biophysical research communications*, vol. 337, no. 1, pp. 401-9, Nov. 2005.

[88] D. S. Gray, J. Tien, and C. S. Chen, “Repositioning of cells by mechanotaxis on surfaces with micropatterned Young ’ s modulus,” 2002.

[89] S. Kidoaki and T. Matsuda, “Microelastic gradient gelatinous gels to induce cellular mechanotaxis.,” *Journal of biotechnology*, vol. 133, no. 2, pp. 225-30, Jan. 2008.

[90] M. Ghibaudo et al., “Traction forces and rigidity sensing regulate cell functions,” *Soft Matter*, vol. 4, no. 9, p. 1836, 2008.

[91] R. D. Sochol, A. T. Higa, R. R. R. Janairo, S. Li, and L. Lin, “Unidirectional mechanical cellular stimuli via micropost array gradients,” *Soft Matter*, vol. 7, no. 10, p. 4606, 2011.

[92] R. D. Sochol, a. T. Higa, R. R. R. Janairo, S. Li, and L. Lin, “Effects of micropost spacing and stiffness on cell motility,” *Micro & Nano Letters*, vol. 6, no. 5, p. 323, 2011.

[93] C. J. Weijer, “Collective cell migration in development.,” *Journal of cell science*, vol. 122, no. Pt 18, pp. 3215-23, Sep. 2009.

[94] R. Farooqui and G. Fenteany, “Multiple rows of cells behind an epithelial wound edge extend cryptic lamellipodia to collectively drive cell-sheet movement.,” *Journal of cell science*, vol. 118, no. Pt 1, pp. 51-63, Jan. 2005.

[95] M. Poujade, A. Hertzog, J. Jouanneau, P. Chavrier, B. Ladoux, and A. Buguin, “Collective migration of an epithelial monolayer,” *October*, 2007.

[96] A. Voulgari and A. Pintzas, “Epithelial-mesenchymal transition in cancer metastasis: mechanisms, markers and strategies to overcome drug resistance in the clinic.,” *Biochimica et biophysica acta*, vol. 1796, no. 2, pp. 75-90, Dec. 2009.

[97] T. E. Angelini, E. Hannezo, X. Trepat, J. J. Fredberg, and D. a. Weitz, “Cell Migration Driven by Cooperative Substrate Deformation Patterns,” *Physical Review Letters*, vol. 104, no. 16, pp. 1-4, Apr. 2010.

[98] B. Alberts, A. Johnson, J. Lewis, M. Raff, K. Roberts, and P. Walter, *Molecular Biology of the Cell*, 4th ed. Garland Science, 2002, p. 1392.

[99] O. Roure et al., “Force mapping in epithelial cell migration,” *PNAS*, pp. 10-15, 2005.

[100] C. M. Nelson et al., “Emergent patterns of growth controlled by multicellular form and mechanics.,” *Proceedings of the National Academy of Sciences of the United States of America*, vol. 102, no. 33, pp. 11594-9, Aug. 2005.

[101] D. Zeng et al., “Three-dimensional modeling of mechanical forces in the extracellular matrix during epithelial lumen formation.,” *Biophysical journal*, vol. 90, no. 12, pp. 4380-91, Jun. 2006.

[102] N. S. Gov, “Collective cell migration patterns: follow the leader.,” *Proceedings of the National Academy of Sciences of the United States of America*, vol. 104, no. 41, pp. 15970-1, Oct. 2007.

[103] G. Seghezzi et al., “Fibroblast growth factor-2 (FGF-2) induces vascular endothelial growth factor (VEGF) expression in the endothelial cells of forming capillaries: an autocrine mechanism contributing to angiogenesis.,” *Journal Of Cell Biology*, vol. 141, no. 7, pp. 1659-73, Jun. 1998.

[104] P. Delerive et al., “Peroxisome Proliferator-Activated Receptor Activators Inhibit Thrombin-Induced Endothelin-1 Production in Human Vascular Endothelial Cells by Inhibiting the,” *Circulation Research*, 1999.

[105] O. Ilina and P. Friedl, “Mechanisms of collective cell migration at a glance.,” *Journal of cell science*, vol. 122, no. Pt 18, pp. 3203-8, Sep. 2009.

[106] G. F. Weber, M. A. Bjerke, and D. W. DeSimone, “A mechanoresponsive cadherin-keratin complex directs polarized protrusive behavior and collective cell migration.,” *Developmental cell*, vol. 22, no. 1, pp. 104-15, Jan. 2012.

[107] P. Rørth, “Collective cell migration.,” *Annual review of cell and developmental biology*, vol. 25, pp. 407-29, Jan. 2009.

[108] M. Inaki, S. Vishnu, A. Cliffe, and P. Rørth, “Effective guidance of collective migration based on differences in cell states.,” *Proceedings of the National Academy of Sciences of the United States of America*, vol. 109, no. 6, pp. 2027-32, Feb. 2012.

[109] O. Markova and P.-F. Lenne, “Calcium signaling in developing embryos: Focus on the regulation of cell shape changes and collective movements.,” *Seminars in cell & developmental biology*, Mar. 2012.

[110] P. Dieterich et al., “Quantitative morphodynamics of endothelial cells within confluent cultures in response to fluid shear stress.,” *Biophysical journal*, vol. 79, no. 3, pp. 1285-97, Sep. 2000.

[111] M. R. Doran, R. J. Mills, A. J. Parker, K. A. Landman, and J. J. Cooper-White, “A cell migration device that maintains a defined surface with no cellular damage during wound edge generation.,” *Lab on a chip*, vol. 9, no. 16, pp. 2364-9, Aug. 2009.

[112] Y. Matsubayashi, M. Ebisuya, S. Honjoh, and E. Nishida, “ERK Activation Propagates in Epithelial Cell Sheets and Regulates Their Migration during Wound Healing,” *Current*, vol. 14, pp. 731-735, 2004.

[113] W.-hui Guo, M. T. Frey, N. A. Burnham, and Y.-li Wang, “Substrate Rigidity Regulates the Formation and Maintenance of Tissues,” *Biophysical Journal*, vol. 90, no. March, 2006.

[114] S. Li, N. F. Huang, and S. Hsu, “Mechanotransduction in Endothelial Cell Migration,” *Journal of Cellular Biochemistry*, vol. 1126, pp. 1110-1126, 2005.

[115] C. S. Chen, J. Tan, and J. Tien, “Mechanotransduction at cell-matrix and cell-cell contacts.,” *Annual review of biomedical engineering*, vol. 6, pp. 275-302, Jan. 2004.

[116] R. J. Pelham and Y. Wang, “Cell locomotion and focal adhesions are regulated by substrate flexibility,” *Proceedings of the National Academy of Sciences of the United States of America*, vol. 94, no. December, pp. 13661-13665, 1997.

[117] H. Haga, C. Irahara, R. Kobayashi, T. Nakagaki, and K. Kawabata, “Collective movement of epithelial cells on a collagen gel substrate.,” *Biophysical journal*, vol. 88, no. 3, pp. 2250-6, Mar. 2005.

[118] O. du Roure et al., “Force mapping in epithelial cell migration.,” *Proceedings of the National Academy of Sciences of the United States of America*, vol. 102, no. 7, pp. 2390-5, Feb. 2005.

[119] M. Drukker and N. Benvenisty, “The immunogenicity of human embryonic stem-derived cells.,” *Trends in biotechnology*, vol. 22, no. 3, pp. 136-41, Mar. 2004.

[120] R. M. Centre and I. Science, “Embryonic stem cells,” *Cell Proliferation*, vol. 37, pp. 23-34, 2004.

[121] I. Kehat et al., “Human embryonic stem cells can differentiate into myocytes with structural and functional properties of cardiomyocytes,” *The Journal of clinical investigation*, vol. 108, no. 3, pp. 363-364, 2001.

[122] J. W. McDonald et al., “Transplanted embryonic stem cells survive, differentiate and promote recovery in injured rat spinal cord.,” *Nature medicine*, vol. 5, no. 12, pp. 1410-2, Dec. 1999.

[123] S. Assady, G. Maor, M. Amit, J. Itskovitz-Eldor, K. L. Skorecki, and M. Tzukerman, “Insulin Production by Human Embryonic Stem Cells,” *Diabetes*, vol. 50, no. 8, pp. 1691-1697, Aug. 2001.

[124] G. R. Martin, “Isolation of a pluripotent cell line from early mouse embryos cultured in medium conditioned by teratocarcinoma stem cells Developmental Biology :,” *Proceedings of the National Academy of Sciences of the United States of America*, vol. 78, no. 12, pp. 7634-7638, 1981.

[125] J. Hanna et al., “Treatment of sickle cell anemia mouse model with iPS cells generated from autologous skin.,” *Science (New York, N.Y.)*, vol. 318, no. 5858, pp. 1920-3, Dec. 2007.

[126] D. L. Clarke, “Generalized Potential of Adult Neural Stem Cells,” *Science*, vol. 288, no. 5471, pp. 1660-1663, Jun. 2000.

[127] I. L. Weissman, “Stem cells: units of development, units of regeneration, and units in evolution.,” *Cell*, vol. 100, no. 1, pp. 157-68, Jan. 2000.

[128] F. H. Gage, “Mammalian Neural Stem Cells,” *Science*, vol. 287, no. 5457, pp. 1433-1438, Feb. 2000.

[129] L. A. Boyer et al., “Core transcriptional regulatory circuitry in human embryonic stem cells.,” *Cell*, vol. 122, no. 6, pp. 947-56, Sep. 2005.

[130] M. Kondo et al., “Biology of hematopoietic stem cells and progenitors: implications for clinical application.,” *Annual review of immunology*, vol. 21, pp. 759-806, Jan. 2003.

[131] R. Jaenisch and R. Young, “Stem cells, the molecular circuitry of pluripotency and nuclear reprogramming.,” *Cell*, vol. 132, no. 4, pp. 567-82, Feb. 2008.

[132] I. Chambers et al., “Functional Expression Cloning of Nanog, a Pluripotency Sustaining Factor in Embryonic Stem Cells,” *Cell*, vol. 113, no. 5, pp. 643-655, May 2003.

[133] N. Sato, L. Meijer, L. Skaltsounis, P. Greengard, and A. H. Brivanlou, “Maintenance of pluripotency in human and mouse embryonic stem cells through activation of Wnt signaling by a pharmacological GSK-3-specific inhibitor.,” *Nature medicine*, vol. 10, no. 1, pp. 55-63, Jan. 2004.

[134] I. L. Weissman, “Stem cells - Scientific, Medical, and Political issues,” *N Engl J Med*, vol. 346, no. 20, pp. 1576-1579, 2002.

[135] M. F. Pera, B. Reubinoff, and a Trounson, “Human embryonic stem cells.,” *Journal of cell science*, vol. 113 (Pt 1, pp. 5-10, Jan. 2000.

[136] R. L. Williams et al., “Myeloid leukaemia inhibitory factor maintains the developmental potential of embryonic stem cells,” *Nature*, vol. 336, pp. 684-687, 1988.

[137] C. Xu et al., “Feeder-free growth of undifferentiated human embryonic stem cells.,” *Nature biotechnology*, vol. 19, no. 10, pp. 971-4, Oct. 2001.

[138] J. Nussbaum et al., “Transplantation of undifferentiated murine embryonic stem cells in the heart: teratoma formation and immune response.,” *FASEB journal : official publication of the Federation of American Societies for Experimental Biology*, vol. 21, no. 7, pp. 1345-57, May 2007.

[139] S. Aggarwal and M. F. Pittenger, “Human mesenchymal stem cells modulate allogeneic immune cell responses.,” *Blood*, vol. 105, no. 4, pp. 1815-22, Feb. 2005.

[140] C. J. Taylor, E. M. Bolton, S. Pocock, L. D. Sharples, R. A. Pedersen, and J. A. Bradley, "Banking on human embryonic stem cells: estimating the number of donor cell lines needed for HLA matching.," *Lancet*, vol. 366, no. 9502, pp. 2019-25, Dec. 2005.

[141] J. Kurtzberg et al., "Placental Blood as a Source of Hematopoietic Stem Cells for Transplantation into Unrelated Recipients," *N Engl J Med* , vol. 335, pp. 157-166, 1996.

[142] T. Wakayama, V. Tabar, I. Rodriguez, A. C. Perry, L. Studer, and P. Mombaerts, "Differentiation of embryonic stem cell lines generated from adult somatic cells by nuclear transfer.," *Science (New York, N.Y.)*, vol. 292, no. 5517, pp. 740-3, Apr. 2001.

[143] J. A. Byrne et al., "Producing primate embryonic stem cells by somatic cell nuclear transfer.," *Nature*, vol. 450, no. 7169, pp. 497-502, Nov. 2007.

[144] C. a Cowan, J. Atienza, D. a Melton, and K. Eggan, "Nuclear reprogramming of somatic cells after fusion with human embryonic stem cells.," *Science*, vol. 309, no. 5739, pp. 1369-73, Aug. 2005.

[145] M. Kanatsu-Shinohara et al., "Generation of pluripotent stem cells from neonatal mouse testis.," *Cell*, vol. 119, no. 7, pp. 1001-12, Dec. 2004.

[146] K. Takahashi, K. Tanabe, M. Ohnuki, M. Narita, T. Ichisaka, and K. Tomoda, "Induction of Pluripotent Stem Cells from Adult Human Fibroblasts by Defined Factors," *Cell*, pp. 861-872, 2007.

[147] K. Takahashi and S. Yamanaka, "Induction of Pluripotent Stem Cells from Mouse Embryonic and Adult Fibroblast Cultures by Defined Factors," *Cell*, vol. 2, pp. 663-676, 2006.

[148] I.-H. Park et al., "Reprogramming of human somatic cells to pluripotency with defined factors.," *Nature*, vol. 451, no. 7175, pp. 141-6, Jan. 2008.

[149] E. Kiskinis and K. Eggan, "Progress toward the clinical application of patient-specific pluripotent stem cells," *J Clin Invest*, vol. 120, no. 1, pp. 51-59, 2010.

[150] I.-H. Park et al., "Disease-specific induced pluripotent stem cells.," *Cell*, vol. 134, no. 5, pp. 877-86, Sep. 2008.

[151] K. Okita, T. Ichisaka, and S. Yamanaka, "Generation of germline-competent induced pluripotent stem cells.," *Nature*, vol. 448, no. 7151, pp. 313-7, Jul. 2007.

[152] C. A. Sommer, M. Stadtfeld, G. J. Murphy, K. Hochedlinger, D. N. Kotton, and G. Mostoslavsky, "Induced pluripotent stem cell generation using a single lentiviral stem cell cassette.," *Stem cells (Dayton, Ohio)*, vol. 27, no. 3, pp. 543-9, Mar. 2009.

[153] B. W. Carey et al., “Reprogramming of murine and human somatic cells using a single polycistronic vector.,” *Proceedings of the National Academy of Sciences of the United States of America*, vol. 106, no. 1, pp. 157-62, Jan. 2009.

[154] C.-W. Chang et al., “Polycistronic lentiviral vector for ‘hit and run’ reprogramming of adult skin fibroblasts to induced pluripotent stem cells.,” *Stem cells (Dayton, Ohio)*, vol. 27, no. 5, pp. 1042-9, May 2009.

[155] M. Stadtfeld, M. Nagaya, J. Utikal, G. Weir, and K. Hochedlinger, “Induced pluripotent stem cells generated without viral integration.,” *Science (New York, N.Y.)*, vol. 322, no. 5903, pp. 945-9, Nov. 2008.

[156] W. Zhou and C. R. Freed, “Adenoviral gene delivery can reprogram human fibroblasts to induced pluripotent stem cells.,” *Stem cells (Dayton, Ohio)*, vol. 27, no. 11, pp. 2667-74, Nov. 2009.

[157] K. Okita, M. Nakagawa, H. Hyenjong, T. Ichisaka, and S. Yamanaka, “Generation of mouse induced pluripotent stem cells without viral vectors.,” *Science (New York, N.Y.)*, vol. 322, no. 5903, pp. 949-53, Nov. 2008.

[158] K. Okita, H. Hong, K. Takahashi, and S. Yamanaka, “Generation of mouse-induced pluripotent stem cells with plasmid vectors.,” *Nature protocols*, vol. 5, no. 3, pp. 418-28, Jan. 2010.

[159] J. Yu et al., “Human induced pluripotent stem cells free of vector and transgene sequences.,” *Science (New York, N.Y.)*, vol. 324, no. 5928, pp. 797-801, May 2009.

[160] K. Woltjen et al., “piggyBac transposition reprograms fibroblasts to induced pluripotent stem cells.,” *Nature*, vol. 458, no. 7239, pp. 766-70, Apr. 2009.

[161] K. Yusa, R. Rad, J. Takeda, and A. Bradley, “Generation of transgene-free induced pluripotent mouse stem cells by the piggyBac transposon.,” *Nature methods*, vol. 6, no. 5, pp. 363-9, May 2009.

[162] K. Kaji, K. Norrby, A. Paca, M. Mileikovsky, P. Mohseni, and K. Woltjen, “Virus-free induction of pluripotency and subsequent excision of reprogramming factors.,” *Nature*, vol. 458, no. 7239, pp. 771-5, Apr. 2009.

[163] D. Kim et al., “Generation of Human Induced Pluripotent Stem Cells by Direct Delivery of Reprogramming Proteins,” *Cell Stem Cell*, vol. 4, no. 6, pp. 472-476, 2010.

[164] H. Zhou et al., “Generation of induced pluripotent stem cells using recombinant proteins.,” *Cell stem cell*, vol. 4, no. 5, pp. 381-4, May 2009.

[165] H.-J. Cho et al., “Induction of pluripotent stem cells from adult somatic cells by protein-based reprogramming without genetic manipulation.,” *Blood*, vol. 116, no. 3, pp. 386-95, Jul. 2010.

[166] L. Warren et al., “Highly efficient reprogramming to pluripotency and directed differentiation of human cells with synthetic modified mRNA.,” *Cell stem cell*, vol. 7, no. 5, pp. 618-30, Nov. 2010.

[167] J. K. Ichida et al., “A small-molecule inhibitor of tgf-Beta signaling replaces sox2 in reprogramming by inducing nanog.,” *Cell stem cell*, vol. 5, no. 5, pp. 491-503, Nov. 2009.

[168] T. Redmer, S. Diecke, T. Grigoryan, A. Quiroga-negreira, W. Birchmeier, and D. Besser, “E-cadherin is crucial for embryonic stem cell pluripotency and can replace OCT4 during somatic cell reprogramming,” *EMBO reports*, vol. 12, no. 7, pp. 720-726, 2011.

[169] P. Mali et al., “Butyrate greatly enhances derivation of human induced pluripotent stem cells by promoting epigenetic remodeling and the expression of pluripotency-associated genes.,” *Stem cells (Dayton, Ohio)*, vol. 28, no. 4, pp. 713-20, Apr. 2010.

[170] M. A. Esteban et al., “Vitamin C enhances the generation of mouse and human induced pluripotent stem cells.,” *Cell stem cell*, vol. 6, no. 1, pp. 71-9, Jan. 2010.

[171] B. Feng, J.-H. Ng, J.-C. D. Heng, and H.-H. Ng, “Molecules that promote or enhance reprogramming of somatic cells to induced pluripotent stem cells.,” *Cell stem cell*, vol. 4, no. 4, pp. 301-12, Apr. 2009.

[172] W. Li and S. Ding, “Small molecules that modulate embryonic stem cell fate and somatic cell reprogramming.,” *Trends in pharmacological sciences*, vol. 31, no. 1, pp. 36-45, Jan. 2010.

[173] V. Krizhanovsky and S. W. Lowe, “Stem cells: The promises and perils of p53.,” *Nature*, vol. 460, no. 7259, pp. 1085-6, Aug. 2009.

[174] Y. Yoshida, K. Takahashi, K. Okita, T. Ichisaka, and S. Yamanaka, “Hypoxia Enhances the Generation of Induced Pluripotent Stem Cells,” *Cell Stem Cell*, vol. 5, p. 237-41, 2009.

[175] S. Hacein-Bey-Abina et al., “Insertional oncogenesis in 4 patients after retrovirus-mediated gene therapy of SCID-X1.,” *The Journal of clinical investigation*, vol. 118, no. 9, pp. 3132-42, Sep. 2008.

[176] S. Hacein-Bey-Abina et al., “LMO2-associated clonal T cell proliferation in two patients after gene therapy for SCID-X1.,” *Science (New York, N.Y.)*, vol. 302, no. 5644, pp. 415-9, Oct. 2003.

[177] M. Ieda et al., “Direct Reprogramming of Fibroblasts into Functional Cardiomyocytes by Defined Factors,” *Cell*, pp. 375-386, 2010.

[178] J. A. Efe et al., “Conversion of mouse fibroblasts into cardiomyocytes using a direct reprogramming strategy,” *Nature Cell Biology*, no. January, 2011.

[179] T. Vierbuchen, A. Ostermeier, Z. P. Pang, Y. Kokubu, T. C. Südhof, and M. Wernig, “Direct conversion of fibroblasts to functional neurons by defined factors.,” *Nature*, vol. 463, no. 7284, pp. 1035-41, Feb. 2010.

[180] Q. Zhou, J. Brown, A. Kanarek, J. Rajagopal, and D. A. Melton, “In vivo reprogramming of adult pancreatic exocrine cells to beta-cells.,” *Nature*, vol. 455, no. 7213, pp. 627-32, Oct. 2008.

[181] E. Szabo et al., “Direct conversion of human fibroblasts to multilineage blood progenitors.,” *Nature*, vol. 468, no. 7323, pp. 521-6, Nov. 2010.

[182] P. Mali et al., “Improved efficiency and pace of generating induced pluripotent stem cells from human adult and fetal fibroblasts.,” *Stem cells (Dayton, Ohio)*, vol. 26, no. 8, pp. 1998-2005, Aug. 2008.

[183] S. M. Wu and K. Hochedlinger, “Harnessing the potential of induced pluripotent stem cells for regenerative medicine.,” *Nature cell biology*, vol. 13, no. 5, pp. 497-505, May 2011.

[184] G. J. Sullivan et al., “Generation of functional human hepatic endoderm from human induced pluripotent stem cells.,” *Hepatology (Baltimore, Md.)*, vol. 51, no. 1, pp. 329-35, Jan. 2010.

[185] K.-D. Choi et al., “Hematopoietic and endothelial differentiation of human induced pluripotent stem cells.,” *Stem cells (Dayton, Ohio)*, vol. 27, no. 3, pp. 559-67, Mar. 2009.

[186] S. Karumbayaram et al., “Directed differentiation of human-induced pluripotent stem cells generates active motor neurons.,” *Stem cells (Dayton, Ohio)*, vol. 27, no. 4, pp. 806-11, Apr. 2009.

[187] F. Guilak, D. M. Cohen, B. T. Estes, J. M. Gimble, W. Liedtke, and C. S. Chen, “Control of stem cell fate by physical interactions with the extracellular matrix.,” *Cell stem cell*, vol. 5, no. 1, pp. 17-26, Jul. 2009.

[188] M. P. Lutolf, P. M. Gilbert, and H. M. Blau, “Designing materials to direct stem-cell fate.,” *Nature*, vol. 462, no. 7272, pp. 433-41, Nov. 2009.

[189] G. C. Reilly and A. J. Engler, “Intrinsic extracellular matrix properties regulate stem cell differentiation.,” *Journal of biomechanics*, vol. 43, no. 1, pp. 55-62, Jan. 2010.

[190] S. R. Peyton and A. J. Putnam, “Extracellular Matrix Rigidity Governs Smooth Muscle Cell Motility in a Biphasic Fashion,” *Journal of Cellular Physiology*, vol. 209, no. July 2004, pp. 198-209, 2005.

[191] N. Huebsch et al., “Harnessing traction-mediated manipulation of the cell/matrix interface to control stem-cell fate.,” *Nature materials*, vol. 9, no. 6, pp. 518-26, Jun. 2010.

[192] S. Even-Ram, V. Artym, and K. M. Yamada, “Matrix control of stem cell fate.,” *Cell*, vol. 126, no. 4, pp. 645-7, Aug. 2006.

[193] Y. Li et al., “Biophysical regulation of histone acetylation in mesenchymal stem cells,” *Biophysical journal*, vol. 100, no. 8, pp. 1902-9, Apr. 2011.

[194] S. Chawla, P. Vanhoutte, F. J. L. Arnold, C. L.-H. Huang, and H. Bading, “Neuronal activity-dependent nucleocytoplasmic shuttling of HDAC4 and HDAC5,” *Journal of Neurochemistry*, vol. 85, no. 1, pp. 151-159, Mar. 2003.

[195] E. A. Miska, C. Karlsson, E. Langley, S. J. Nielsen, J. Pines, and T. Kouzarides, “HDAC4 deacetylase associates with and represses the MEF2 transcription factor.,” *The EMBO journal*, vol. 18, no. 18, pp. 5099-107, Sep. 1999.

[196] P. Friedl and K. Wolf, “Plasticity of cell migration: a multiscale tuning model.,” *The Journal of cell biology*, vol. 188, no. 1, pp. 11-9, Jan. 2010.

[197] A. C. Rowat, J. Lammerding, H. Herrmann, and U. Aebi, “Towards an integrated understanding of the structure and mechanics of the cell nucleus.,” *BioEssays : news and reviews in molecular, cellular and developmental biology*, vol. 30, no. 3, pp. 226-36, Mar. 2008.

[198] K. N. Dahl, E. A. Booth-Gauthier, and B. Ladoux, “In the middle of it all: mutual mechanical regulation between the nucleus and the cytoskeleton.,” *Journal of biomechanics*, vol. 43, no. 1, pp. 2-8, Jan. 2010.

[199] A. Buxboim, I. L. Ivanovska, and D. E. Discher, “Matrix elasticity, cytoskeletal forces and physics of the nucleus: how deeply do cells ‘feel’ outside and in?,” *Journal of cell science*, vol. 123, no. Pt 3, pp. 297-308, Feb. 2010.

[200] J. MISLOW, “Nesprin-1 [alpha] self-associates and binds directly to emerin and lamin A in vitro,” *FEBS Letters*, vol. 525, no. 1–3, pp. 135-140, Aug. 2002.

[201] V. C. Padmakumar et al., “The inner nuclear membrane protein Sun1 mediates the anchorage of Nesprin-2 to the nuclear envelope.,” *Journal of cell science*, vol. 118, no. Pt 15, pp. 3419-30, Aug. 2005.

[202] J. J. Norman and T. A. Desai, “Methods for fabrication of nanoscale topography for tissue engineering scaffolds.,” *Annals of biomedical engineering*, vol. 34, no. 1, pp. 89-101, Jan. 2006.

[203] J. F. Casella, M. D. Flanagan, and S. Lin, “Cytochalasin D inhibits actin polymerization and induces depolymerization of actin filaments formed during platelet shape change,” *Nature*, vol. 293, no. 5830, pp. 302-305, Sep. 1981.

[204] S. Hirano, A. Nose, K. Hatta, A. Kawakami, and M. Takeichi, “Calcium-dependent cell-cell adhesion molecules (cadherins): subclass specificities and possible involvement of actin bundles.,” *The Journal of Cell Biology*, vol. 105, no. 6 Pt 1, pp. 2501-10, Dec. 1987.

[205] B. Grunwald, “The structural and functional analysis of cadherin cell adhesion molecules,” *Current Opinion in Cell Biology*, vol. 5, pp. 797-805, 1993.

[206] D. Sieg, C. Hauck, and D. Schlaepfer, “Required role of focal adhesion kinase (FAK) for integrin-stimulated cell migration,” *J. Cell Sci.*, vol. 112, no. 16, pp. 2677-2691, Aug. 1999.

[207] M. Wernig et al., “A drug-inducible transgenic system for direct reprogramming of multiple somatic cell types.,” *Nature biotechnology*, vol. 26, no. 8, pp. 916-24, Aug. 2008.

[208] N. Maherali, T. Ahfeldt, A. Rigamonti, J. Utikal, C. Cowan, and K. Hochedlinger, “A high-efficiency system for the generation and study of human induced pluripotent stem cells.,” *Cell stem cell*, vol. 3, no. 3, pp. 340-5, Sep. 2008.

[209] K. Kim et al., “Epigenetic memory in induced pluripotent stem cells,” *Nature*, vol. 467, no. September, 2010.